Design, Modelling and Fabrication of a Robotic Retractor for Colorectal Surgery

SUBMITTED IN PARTIAL FULFILLMENT OF THE REQUIREMENTS
OF THE DEGREE OF DOCTOR OF PHILOSOPHY

December 2016

Tianyi Tao

School of Engineering and Materials Science
Queen Mary University of London
Mile End Road, London, E1 4NS

Declaration

I declare that the work performed is entirely by myself during the course of my PhD studies at the Queen Mary University of London and has not been submitted for a degree at this or any other University.

Tianyi Tao

Acknowledgement

There are various people that I would like to thank for their assistance and encouragement.

My sincere gratitude goes to Dr Hasan Shaheed and Dr Ranjan Vepa, who expertly guided me through my graduate education of four years of discovery. Their unwavering enthusiasm for physics kept me constantly engaged with my research, and their personal generosity helped make my time in Queen Mary enjoyable. I would like to thank our partner Dr Mo Thaha whose advice on my research was priceless.

I would like to express my special appreciation and thanks to my families. Words cannot express how grateful I am to my mother, my father and my husband for all the sacrifices that you’ve made on my behalf. I would like to thank them for encouraging my research and for allowing me to grow as a research scientist.

Abstract

This research presents the design, fabrication and controller development of a robotic retractor which driven by a robotic manipulator for laparoscopic colorectal surgery. The system consists of a dual-head fan retractor and a manipulator. The dual-head fan retractor comprises two fan devices, retractor wrist, tubular element and handle. The fan device is facilitated with a fan end-effector, an expansion mechanism and a clutch-spring mechanism. Two fan devices have been used in the system to provide an anthropoid hand-holding shape which is specifically advanced for surgical purpose because intestine tends to slip when subject to disturbance and the anthropoid hand-holding shape can effectively halt that. One of the two fan devices is rotatable which makes the anthropoid hand-holding shape achievable. The retractor wrist possesses a triggering device, based on clutch-spring mechanism, for rotating the rotatable fan device. The clutch-spring mechanism has an impact on rotating the palms of the fan devices. In front of the handle, it is the so called front body which includes two fan devices, retractor wrist and tubular element. The front body can be controlled and is motorised using two motors fixed to the tubular element. The dual-head fan retractor is modelled in SolidWorks, and stress analysis of the retractor has been carried out by SolidWorks Simulation. Then, the mathematical model of the fan blades is developed.

A 3-joint manipulator is modelled and controlled by a computed torque PD control approach as part of an investigative study to fit such a system to the retractor for robotic manipulation. Based on this investigation, the retractor is attached to a 2-joint robotic manipulator which has one rotational joint and a prismatic joint. This manipulator is mathematically modelled, and the dynamic equations are obtained. Control methods from Azenha and Khatib are simulated and compared. Azenha & Machado's method has fewer input parameters and less oscillation when utilising the same control gains. Time-optimal control is then successfully developed for the above 2-joint manipulator. This study clearly indicates that a retractor to be used for laparoscopic surgery can be effectively controlled using a multi-joints and multi degrees of freedom robotic manipulator.

Contents

List of Figures

List of Tables

List of Symbols

$\mathbf{F}$	Vector of force acting on the centre mass
$\boldsymbol{v}$	Vector of linear velocity
$\dot{\boldsymbol{v}}$	Vector of linear acceleration
$\boldsymbol{\omega}$	Vector of angular velocity
$\dot{\boldsymbol{\omega}}$	Vector of angular acceleration
$\boldsymbol{I}$	Inertia tensor
$\boldsymbol{R}$	Rotational matrix
$\boldsymbol{p}$	Constant in frame
$\boldsymbol{z}$	Unit vector of coordinate axes z
$\mathbf{\Gamma}$	Vector of generalized torque acting on the body
$\mathbf{\Theta}$	Vector of joint angle value
$\dot{\mathbf{\Theta}}$	Vector of joint angle velocity
$\ddot{\mathbf{\Theta}}$	Vector of joint angle acceleration
$\boldsymbol{m}$	Vector of mass
$\boldsymbol{X}$	Vector of position
$\boldsymbol{Y}$	Vector of position
$\mathbf{H}$	Inertia matrix
$\mathbf{C}$	A matrix denoting Coriolis and centrifugal forces
$\mathbf{G}$	A vector of gravitational forces
$\mathbf{\Phi}$	Nonlinear term
$\mathbf{\Psi}$	Nonlinear term
$\boldsymbol{\alpha}$	Undetermined matrix
$\boldsymbol{\beta}$	Undetermined matrix
$\mathbf{e}$	Vector of error
$\mathbf{e}_f$	Interaction force error
$\mathbf{M_m}$	Desired inertia
$\mathbf{B_m}$	Damping matrix
$\mathbf{K_m}$	Stiffness matrix

$\mathbf{M}$	Kinetic energy matrix
$\mathbf{B}$	Vector of end-effector centrifugal and Coriolis forces
$\mathbf{K}$	Vector gravity
$\mathbf{z}$	The n-dimensional state vector of the compensator
$\mathbf{A}$	Semi-negative definite matrix
$\mathbf{s}$	Switching function
$\boldsymbol{J}$	Jacobian
$\mathbf{\Omega}$	Vector defines the generalized position and force
i	Link number
$f(x)$	Function
I	Mass moment inertia
m	Mass
V	Volum
D	Diameter
g	Gravity coefficient
ρ	Density
F	Force
P	Pitch
t	Thickness
L	Lagrangian
E_k	Kinetic energy
E_p	Potential energy
X	Position
Y	Position
Z	Position
Γ	Joint torque
θ	Angle
θ_{id}	Desired angle
θ_w	Angle of the wall

$\dot{\theta}$	Angle velocity
$\ddot{\theta}$	Angle acceleration
φ	Angle
$\dot{\varphi}$	Angle velocity
$\ddot{\varphi}$	Angle acceleration
z	Position
$\dot{z}$	Position velocity
$\ddot{z}$	Position acceleration
l	Position
l_{id}	Desired prismatic joint position
$\dot{l}$	Position velocity
$\ddot{l}$	Position acceleration
ζ_i	Damping ratio
ω_i	Undamped angular frequency of the oscillator
l_{icg}	The position of the centre gravity according to *i* th joint
u_{icg}	The radius of gyration about the centre gravity of the *i* th link
M	Mass of the intestine
d	Link offset
k_v	Derivative control gain
k_p	Potential control gain
e	Error
u	Control parameter
H	Hamiltonian
c_{ni}	Constant

Chapter 1

Introduction

1.1 Intestine and colorectal cancer

The intestine is a segment of the alimentary canal starting from the pyloric sphincter to the anus. The small intestine can be divided into colon (caecum, ascending colon, transverse colon, descending colon) and rectum (Anthea et al., 1993). Intestine, as a section of the digestive system, has a remarkable function.

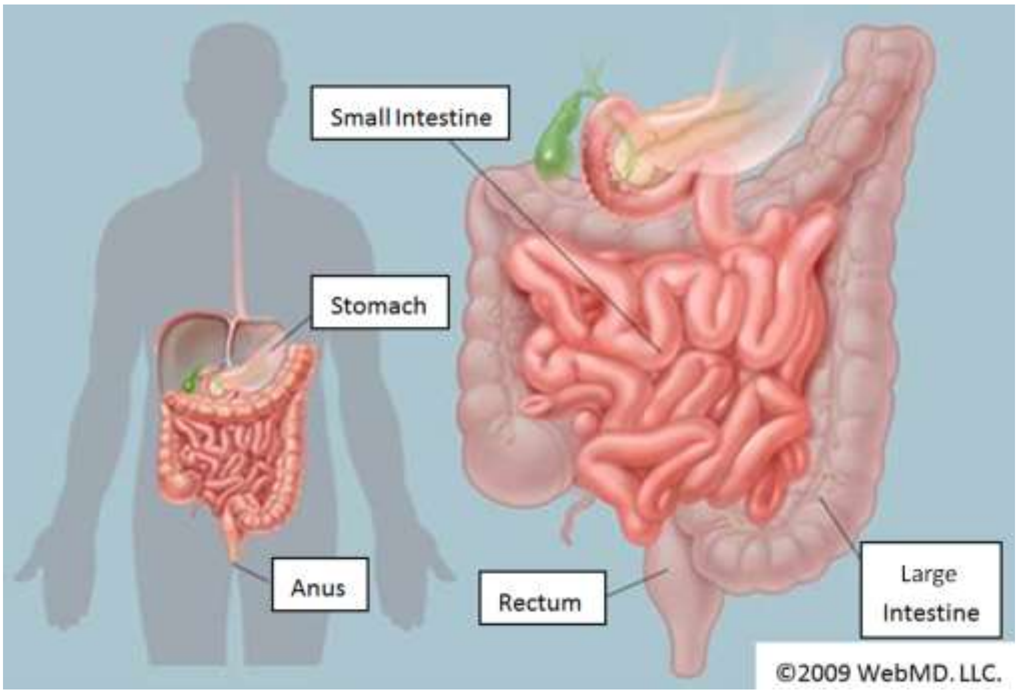

Figure 1. 1: Diagram of the digestion system (WebMD, 2009).

The small intestine is responsible for food digestion and absorption. Foods like carbohydrates, proteins and fats are digested in duodenum with the help of pancreatic juices. Later nutrients absorbed from digested food are transferred into the blood stream by jejunum and ileum. Colon is in charge of the final stages of the digestive process, and its function is described in three steps: absorption of water and decomposition of food; storing undigested food; and eliminating waste. With the help of the colon, the human body maintains the fluid balance by absorbing vitamins, processing indigestible material and storing waste before it is eliminated. However, unhealthy lifestyle and increasing age are inducements to colorectal diseases, including colorectal cancer.

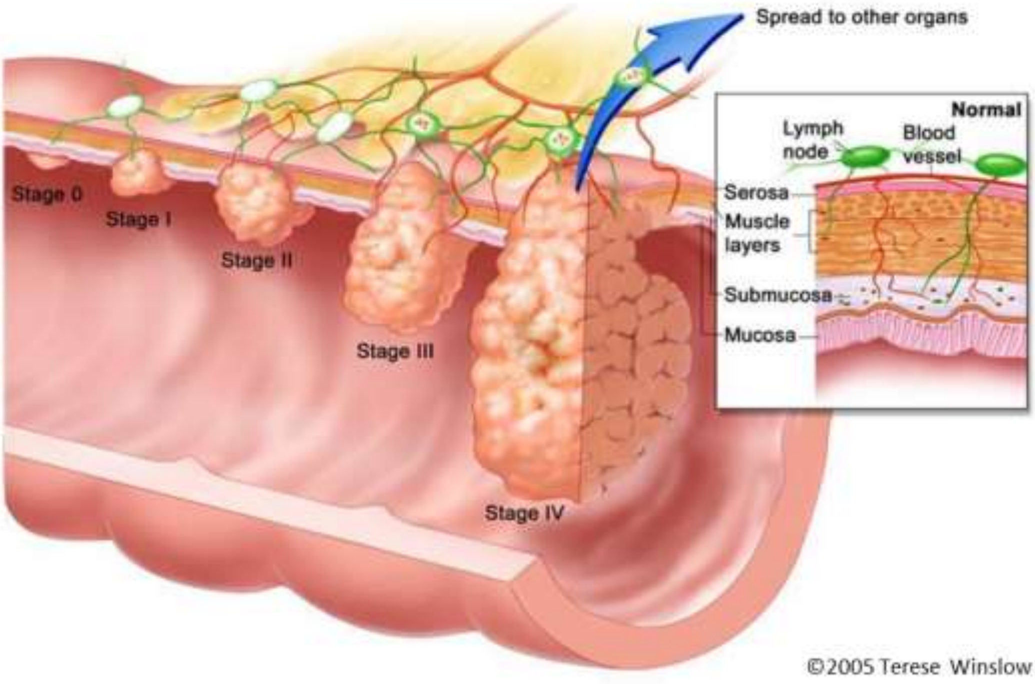

Figure 1. 2: Diagram of cancer tumour in different stages (School of Medicine, 2012).

The cause of colorectal cancer is multi-factorial. Increasing age and an unhealthy lifestyle are well recognised causative factors. Typically, colorectal cancer starts in the lining of the bowel. If leave untreated, the cancer may spread into the muscle layers and eventually may grow through the entire wall of the intestine to spread outside. Colorectal cancer may present with increased constipation, blood in the stool, weight loss, loss of appetite, nausea or vomiting (Alpers et al., 2011). Individuals who are over 65 years old have the highest incidence of developing colorectal cancer (Edwards et al. 2010). Rectal bleeding has high risk in those who are over 50 years old (Astin et al., 2011). Globally, approximate 1 million people are affected by this cancer each year. (Jemal et al., 2011; Merika et al., 2010).

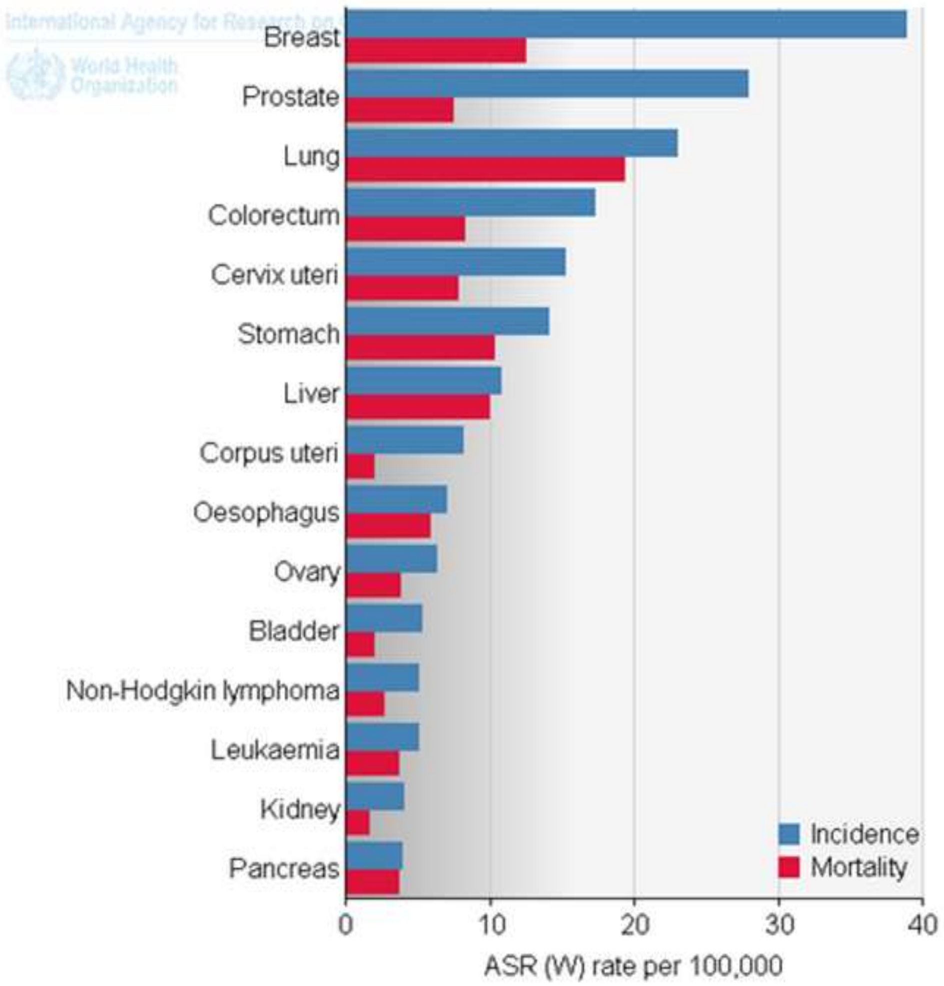

Figure 1. 3: Crude rates for different cancers regarding to incidence and mortality (World Health Organization, 2013).

Figure 1.3 above shows a chart established by International Agency for research on World Health Organization. Colorectal cancer is the fifth cause of cancer death after lung, breast, stomach, and liver cancers. The crude rate of mortality is 50%. Figure

1.4 records the statistics of colorectal cancer population in the whole world area. Although, colorectal cancer is a stubborn illness, there are certain cures that can extend lifetime and making people comfortable.

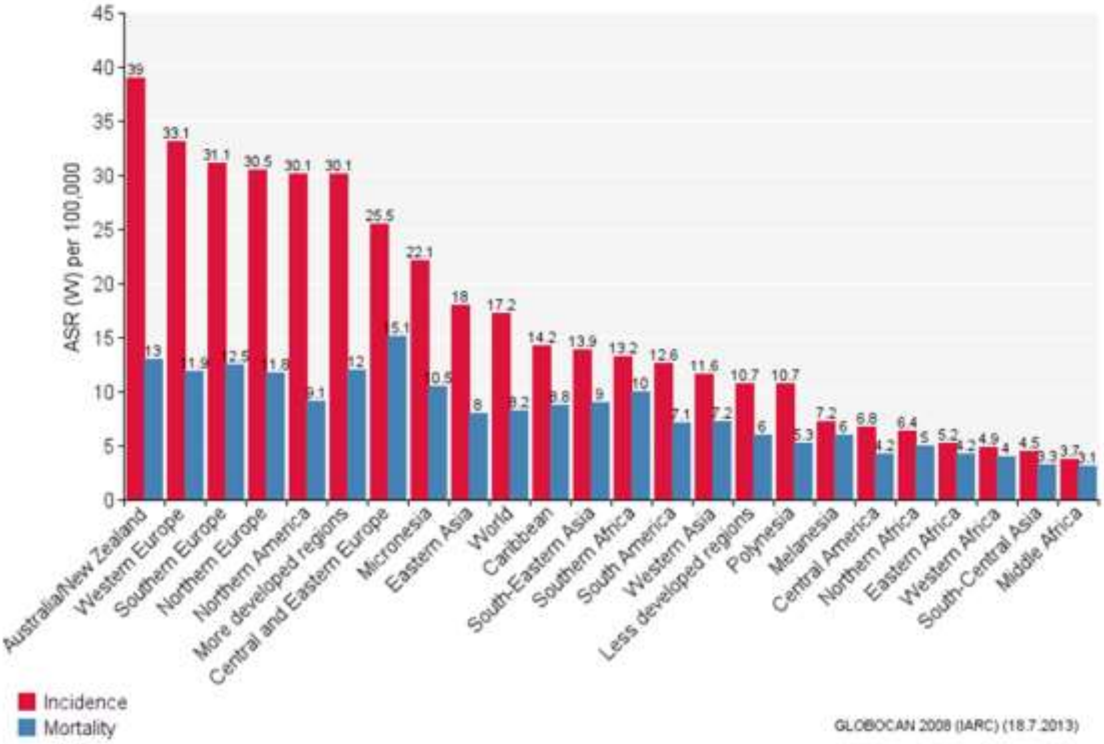

Figure 1. 4 Colorectal cancer becomes the fifth cause of cancer death (World Health Organisation, 2013).

1.2 Project background

Colorectal cancer is uncontrolled cancer cell growing in the intestine. Carrying out a colectomy is one of the effective treatments to deal with colorectal cancer at an early stage. The other treatments are radiation therapy, chemotherapy and targeted therapy (National Cancer Institute, 2016). Traditionally, colorectal resection is carried out via a laparotomy (open colorectal surgery), which involves a long incision of the abdominal wall. Increasingly, in the last two decades, colectomy including for cancer are done through laparoscopic or keyhole approach (Milsom, 2006). In contrast to open surgery, laparoscopic colorectal surgery uses several smaller incisions (5mm to 10 mm long) on access the abdominal cavity. The laparoscopic instruments and surgical camera are then passed through these small incisions to reach the inside working area. With the help of the laparoscopic camera, the surgeon is able to observe the surgical filed that allows them to safely remove the diseased segment of the bowel from the outside using the long laparoscopic instrument. This is usually followed by reconnecting the colon/rectum through an anastomosis. Compared to open colorectal surgery, laparoscopic colorectal surgery is relatively new and is an evolving surgical method. Laparoscopic colorectal surgery, which makes smaller incisions, has several advantages over open surgery. This includes reduced surgical stress, lesser postoperative pain, lower wound infection rates, short hospital stay and fast recovery (Golub, 1998). However, laparoscopic surgery introduces a higher skills requirement and challenges of significant pose, as the surgeon does not have the same haptic feedback from the long laparoscopic instruments, which he/she operates remotely from the surgical field (Botden, 2008). Therefore, there is a need to improve laparoscopic techniques and particularly laparoscopic instrumentation to make surgery easier and safer. This is especially true as currently laparoscopic colorectal surgery is accepted as a safe and feasible alternative to open colorectal surgery (Cummings, 2012).

In any surgery, a clear and an unobstructed view of the surgical field is paramount as it allows the surgeon to operate safely without damaging the organ being operated and safe guarding the adjacent vital structures. Retractors are thus vital instruments in surgery. In open surgery, retraction of tissues is achieved by a combination of using the surgeons and assistants hands, and with custom designed retracting instruments. In laparoscopic colorectal surgery, retraction of tissues to obtain adequate visualisation of the surgical field is more challenging due mainly to the long distance involved, narrow instruments used, and loss of haptic feedback. Typically, retractor is a crucial surgical part which plays a role of holding, pushing tissues and establishing area for operation during surgical procedures. A retractor consists of a handle, a long pole and an end-effector. In commercial retractor models, the end-effectors are in different shapes such as polyarticular pole, broad paddle and multi-fan blades. Most of the end-effectors have only one degree of freedom which can only open in a plane. Due to the limited movements, the end-effectors cannot keep the rest of intestine away from the working space. Moreover, any little disturbance on the intestine may cause it moving away from its original position which can be a serious problem when the surgeon is performing the operation. These problems are limitations of operating an effective and safe surgery and good solutions need to be proposed.

1.3 Motivations

For providing more efficient and effective laparoscopic colorectal surgery, a robotic motorised retractor with multi-degree of freedom will be designed in this thesis. The retractor to be designed has a lot advantages over current commercial models. To be specific, the well-controlled motorisation of the retractor contributes to the accurate and stable movements, while as multi-degree of freedom makes operation of surgery more convenient. Furthermore, lack of motorised retractor end-effector that can provide multi-degree of freedom makes the development of more functional retractor becoming increasingly necessary.

1.4 Aims and objectives

The aim of this research is to design, fabricate and develop controller for a particular robotic retractor driven by a robotic manipulator for laparoscopic surgery. The objectives of the investigation include,

1. Design a fan-shaped retractor with a hand holding shape.
2. Design the retractor with an adjustable hand-holding angle that can push away obstacles without repositioning the entire retractor.
3. Facilitate the retractor with axial rotation motorisation to reduce movement range for the purpose of reducing the chances of operational disaster.
4. Fabrication of a dual-head fan retractor with necessary components and flexibility defined.
5. Development of compliance control for sophisticated controls for the retractor with the robotic manipulator.
6. Implementation of the Time-Optimal control applies on the robotic manipulator.

1.5 Contribution to knowledge

1.5.1 Design and fabrication of a single-head fan retractor

A single-head fan retractor is designed and manufactured. Compares with commercial fan retractors, the single-head fan retractor is reasonably motorised.

1.5.2 Design and fabrication of a dual-head fan retractor

Previously, the single-head fan retractor is designed but its end-effector expands in a plane which does not meet the requirement of a hand holding shape. Thus, a dual-head fan retractor is designed and its prototype is fabricated later. We will discuss the manufacturing, control system and design of the dual-head fan retractor in more detail in Chapter 3.

1.5.3 Retractor model development

In Chapter 4, the mathematical model of the fan blades and end-effector are established. Later in Chapter 5, the mathematical model of a 3-joint manipulator which has three rotational joints is introduced. The robotic retractor manipulator (2-joint manipulator) with one rotational joint and a prismatic joint has been modelled. At the end of the Chapter 5, another robotic retractor manipulator which has 3-joint (two rotational joints and one prismatic joint) is modelled.

1.5.4 Robotic control of the retractor

The robotic manipulators which manipulate the retractor are dynamically controlled. The kinematic and dynamic equations of the first manipulator (a 3-joint manipulator with three rotational joints) are derived and the corresponding controllers are developed. The controllers applied on the 3-joint manipulator are computed torque PD controllers and each joints are controlled separately. The second manipulator (a 2- joint manipulator with two rotational joints) is mathematically modelled and controlled using Azenha & Machado’s (1997) and Khatib & Burdick’s (1986) position/force control algorithms separately.

1.5.5 Time-optimal control of the robotic retractor manipulator

A time-optimal control law for the robotic retractor 2-joint manipulator (one rotational joint and one prismatic joint) is synthesised by linearising the dynamical model of the manipulator.

1.6 Research Methodology

The mechanical structure drawings of the dual-head fan retractor are developed in SolidWorks. Then, the ratio 2.5 prototype of the fan retractor is fabricated. Among all components, the laminated bar is built by stainless steel cutting by wire cutting machine and rest of the components are built by acrylonitrile butadiene styrene (ABS) using 3D printer. The building procedures of the 3D printer are described as below. The 3D printer first built a holder, and then it creates the component regarding the shape of the holder. Finally, put the whole item, which includes the holder and the components, into boiled water for 24 hours. The holder will dissolve into the boiled water and the component, that melting point is 105 °C, is ready for assembly after drying. After built all the components, the 2.5 ratio prototype of the dual-head fan retractor is assembled. The dual-head fan retractor 2.5 ratio prototype can pass through a 42.3 mm diameter hole and the prototype overall length is 950 mm. The 2.5 ratio prototype is built to show the motorised movement and four degrees of freedom. However, the 2.5 ratio prototype is not able to implement force testing because it is not in the real size prototype. Therefore, SolidWorks Simulation has been chosen to fulfil the stress analysis of the modelled original sized dual-head fan retractor. The SolidWorks Simulation is adept at simulating the results when a particular pressure is loaded on the retractor. The displacement figure, the factor of safety figure and the stress distribution figure are the achieving results. The displacement figure shows the deformation by colour when force is loaded on the retractor. The factor of safety displays the unsafely areas when force is loaded. The stress distribution indicates the pressure distribution utilising colour changing from red to blue and the biggest stress point is marked. Analysing the stress distribution is to alert that breakage and cracking happen on the red colour segment. To sum up, above are the methods of designing, fabricating and analysing the dual-head fan retractor. Our vision of retractor is attached at the end of a robotic manipulator during surgical procedure. The three manipulators are modelled by using MATLAB Simulink: the 3-joint manipulator (three rotational joints); the 2-joint manipulator (two rotational joint); and the other 2-joint manipulator (one rotational joint and one prismatic joint). Modelling and controlling of the 3-joint manipulator help us pursue theoretical study and gain practical experience for establishing and manipulating a robotic manipulator. Modelling the 2-joint manipulator (two rotational joint) helps choose a better algorithm out of Azenha & Machado’s and Khatib & Burdick’s algorithms. The other 2-joint manipulator (one rotational joint and one prismatic joint) is the robotic manipulator which attaches the retractor. Both the 2-joint manipulator and the retractor are modelled in MATLAB Simulink and come with simulation results.

1.7 Thesis outline

Chapter 2 first presents the definition of colorectal cancer and the perniciousness of colorectal cancer. It primarily shows the perniciousness of colorectal cancer to the elderly. Then, the differences of open colorectal surgery and laparoscopic colorectal surgery have illustrated. The traditional laparoscopic retractor is introduced and the review of relevant literature is presented.

Chapter 3 presents the general design of the dual-head fan retractor. The dual-head fan retractor consists of a handle portion, a tubular element, a wrist and two fan expansion devices. The next section is about the design of retractor wrist and axial of the front body. The last section notes the stress analysis of the dual-head fan retractor when put force on it.

Chapter 4 describes the mathematical modelling for the dual-head fan retractor with the manipulator. The fan blade motion is similar as a spherical pendulum. The mathematical modelling of the dual-head fan retractor is performed according to the spherical pendulum. The mathematical model of the clutch is illustrated then.

Chapter 5 presents the modelling of the robotic manipulator for the dual-head fan retractor. First, a three rotational joints manipulator is mathematically modelled and controlled. Second, the dual-head fan retractor with a 2-joint manipulator is modelled. Here, the 2-joint manipulator has one rotational joint and a prismatic joint. Third, the mathematical model for the dual-hand fan retractor with a 3-joint manipulator with two rotatable joints and a prismatic joint is developed. This 3-joint manipulator is modelled for further work.

Chapter 6 illustrates the control law synthesis, the impedance control and its appropriateness explained first; later on, the variable structure control (VSC) impedance control algorithm is presented. Then depending on the methodology of Khatib and Burdick's (1986) report, the Lyapunov design of a VSC is discussed. Finally, a hybrid position and force control with constrained is explained depending on Azenha & Machado's (1997) methods. It is found that Azenha & Machado's algorithm is simpler and provides better performance.

Chapter 7 presents principles and practice of the time-optimal control. In this chapter, on-off control (Vakhrameev, 1997) and Pontryagin's minimum principle (Onori, 2016) reported. A linear theory of time-optimal control of a second order system is utilised on the 2-joint manipulator. The 2-joint manipulator has one rotational joint and a prismatic joint.

Chapter 8 describes conclusion and future works. So far the mathematic model of the fan blades and manipulators are carried out. Future work about a 3-joint manipulator will be considered. The 3-joint manipulator has two rotational joint and a prismatic joint. The difficulty of modelling the 3-joint manipulator will be system singularity.

Chapter 2

Review of literature

When colorectal cancer is detected at a late stage particularly after it has metastasised, treatment is directed mostly at extending the lifetime and making people feel comfortable. Early stage diagnosis of colorectal cancer allows curative treatment mainly by colectomy. As for colectomy, it can be summarised into two steps: cutting and removing the tumour bearing part of the large bowel with adequate margins and reconnecting the cut ends of the intestine or rectum to restore continuity of the bowel.

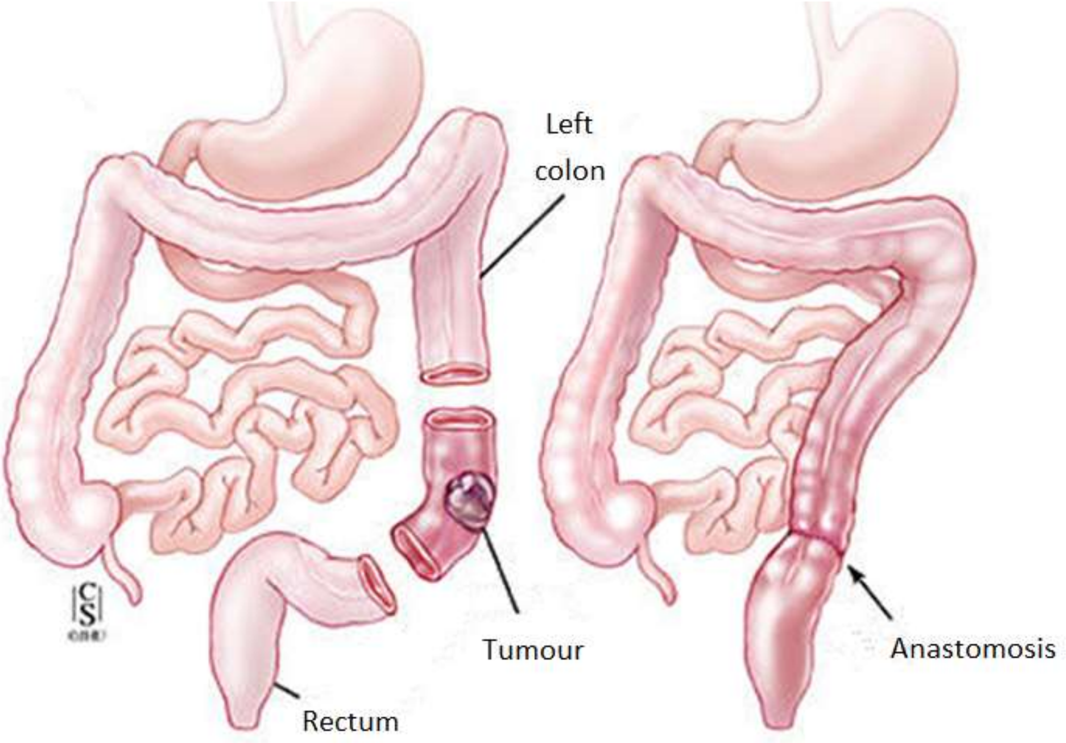

Figure 2. 1: Diagrams of Colorectal surgery (The AnastomoSEAL Project, 2013).

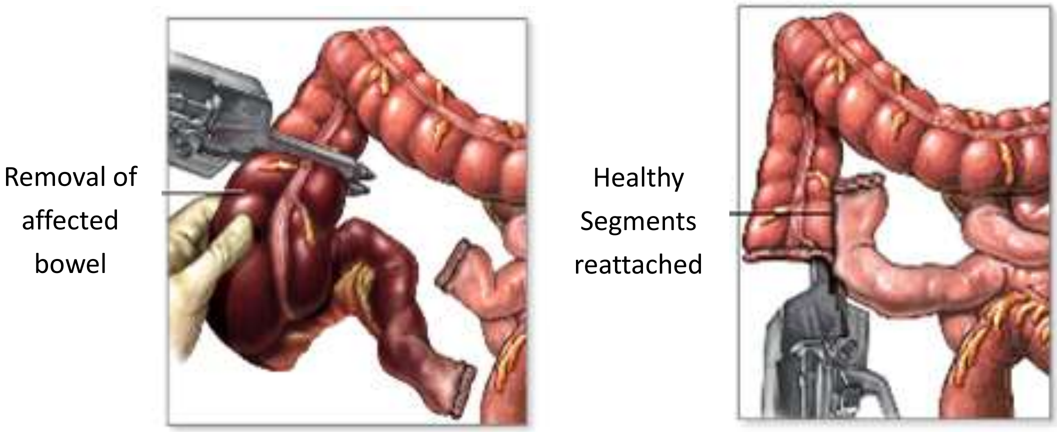

Figure 2. 2: Pictures for colectomy procedures (University of Maryland medical centre, 2012).

The preferred treatment for patients with colorectal cancer is surgical removal carried out either by an open or a laparoscopic approach.

2.1 Open colorectal surgery and laparoscopic colorectal surgery

Open colorectal surgery (OCS), is a surgical procedure involving a 6-14 inches long incision through the abdominal wall to gain access into the abdominal cavity.

Different from open colorectal surgery, laparoscopic colorectal surgery requires one to four small incisions, while each measuring less than 0.5 inches in length.

Compared to OCS, the procedure times for LCS are usually longer and the procedure is also more complicated. LCS has several advantages over OCS. First, LCS reduces blood loss and there is less need for blood transfusion. Second, LCS makes smaller incision which shortens recovery time, lessens the pain and post-operative scarring. Third, in LCS, less pain leads to less pain medication. Fourth, LCS reduces hospital stay or same and facilitates early discharge resulting in a faster return to normalcy. Fifth, LCS limits exposure of tissues to the atmosphere and reduces the risk of acquiring infections (Delaney et al., 2008; Kiran et al., 2004; Tjandra and Chan, 2006).

Randomized controlled trials (RCT) have shown that there is no long-term survival difference between LCS and OCS (Buunen et al., 2009; Fleshman et al., 2007). Commings (2005) argued that the 5-year survival rate is lower than that reported in RCTs. LCS has no association with worse survival when compared with OCS. He also mentioned that LCS is a reasonable choice for older patients suffering from colon cancer as LCS decreases hospital stay because the trauma is much smaller. According to Lacy (2008), Li (2011) Guerrieri (2012), Cannon (2012), Sticca (2013), LCS and OCS for colon cancer offer similar long-term outcomes. One thing to make sure is the operation hours, Fesharakizadeh (2013) states that longer operations cause more prolonged post-operative ileus.

2.2 Traditional retractor

The traditional laparoscopic retractor is divided into three types: polyarticular retractor, plane retractor and fan retractor.

2.2.1 Polyarticular retractor

Polyarticular retractor is an instrument assembled by loops which connecting cylinder or barrel elements. The end-effector of the polyarticular retractor is a polyarticular pole. There is a control rod that provides a rotatable presentation. Here are two examples polyarticular retractors from Kuzmak (1996) and Cuschieri (2004).

Kuzmak (1996) and his group had shown a polyarticular retractor as the United States patent. This patent presents a blunt dissector device particularly adapted for the use of laparoscopic. An elongated dissector element had chosen. The retractor end-effector is a finger-like element which has a flexible distal portion. The end-effector which driven by a control rod is joined to the distal element for controlling a flexible movement. That is to make the curvature under control. For having a rotatable mount, the proximal portion of the dissector element allows the dissector element to be rotated so as to control the tip of the dissector element. The advantageous implementation includes a control rod extending along the distal element.

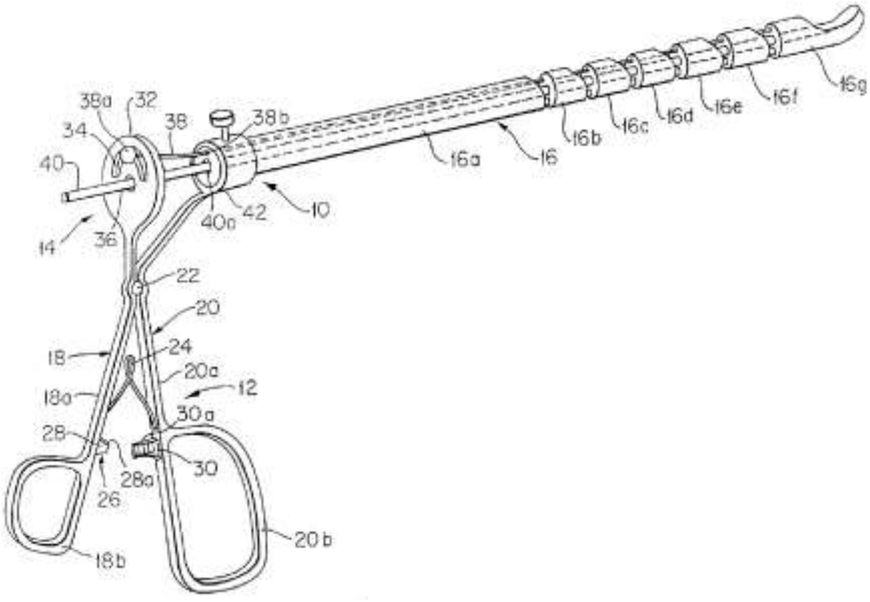

Figure 2. 3: Finger-like laparoscopic blunt dissector device from Kuzmak (1996).

Cuschieri (2004) group presented a retractor for use in endoscopic surgery. The patent is from the United States. The patent notes a retractor comprising a shaft which has a hand grasp arranged on the proximal end. In their patent, the distal end can be moved out at the distal end. For producing a retractor that can be used for hygienic manner, the retractor shaped as a closing ring structure.

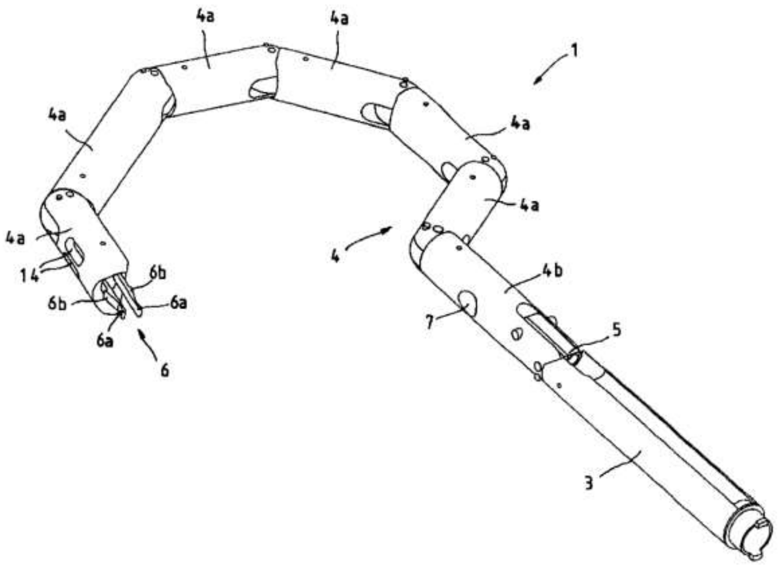

Figure 2. 4: Retractor for use in endoscopic surgery from Cuschieri (2004).

2.2.2 Plane retractor

Plane retractor is a medical instrument that relies on a pushing bar to expand its working space. The end-effector of the plane retractor is a broad paddle. The distal end of the rod is lead by the pushing bar which can promote an open position for the end-effector. Some patents have produced in this regard.

Hiltebrandt (1992) and his group described a patent from the United States. The patent is an organ manipulator which is for exposing an organ that is situated for investigation. The organ manipulator assembled by a multi-joint lever system of articulated arms. It can be simulated from an axial position to an open position. The open position is rhombus shaped structure.

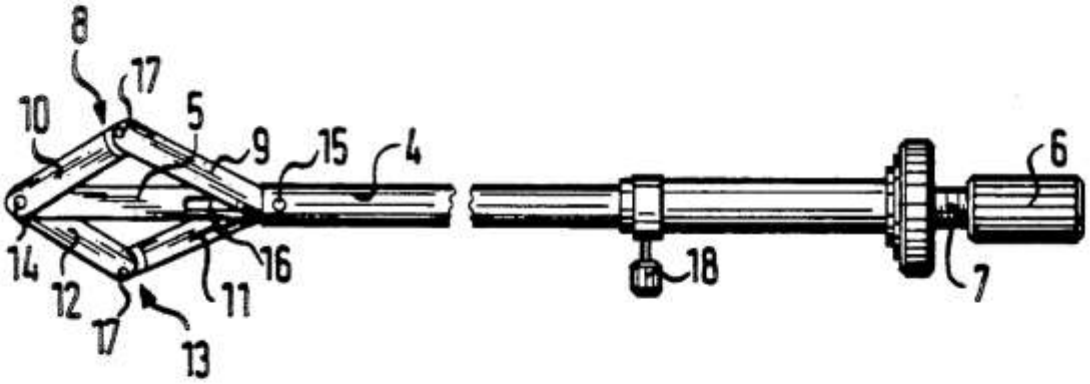

Figure 2. 5: Organ manipulator made by Hiltebrandt (1992).

Jamner (1993) had his group created a patent that is issued by the United States. The patent is related to an endoscopic retractor which is suitable for use in laparoscopic surgery. The retractor is mainly for use in retracting, separating and exposing different tissues, organs and viscera. This retractor constituted by an elongated hollow tubular shaft and an expandable segmented tip. The tubular shaft has an end-effector at the distal end while the segmented tip actuated by a rigid connecting rod. The connecting rod extends through the hollow tubular shaft to the handle. The retractor is manually operated for expanding and collapsing.

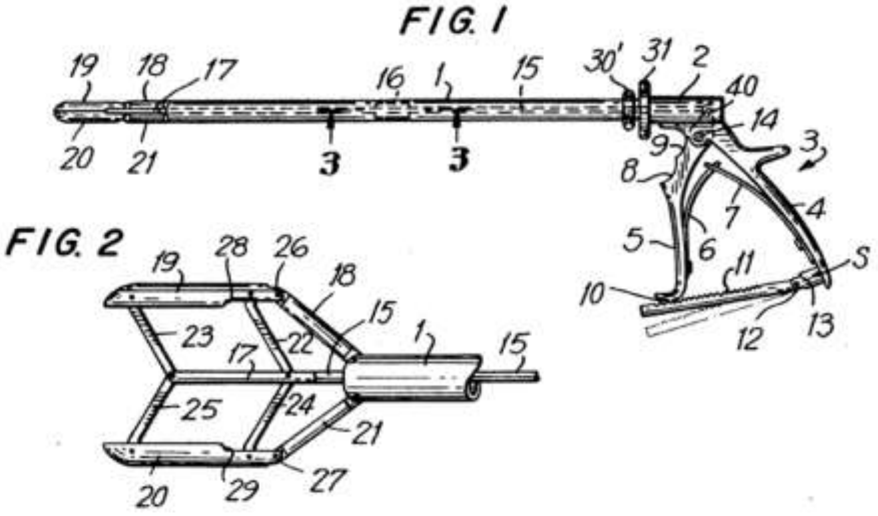

Figure 2.6: Endoscopic retractor created by Jamner (1993).

Koninckx (1997) created a patent from the United States for laparoscopic hysterectomy.

The patent is related to an instrument which composes by a pole and a controllable end-effector. Two wings, which move forwards and backwards, is the end-effector of the instrument. The end-effector is operated by the central pushing bar. During operation, the open position of the end-effector touches the internal wall of the uterus.

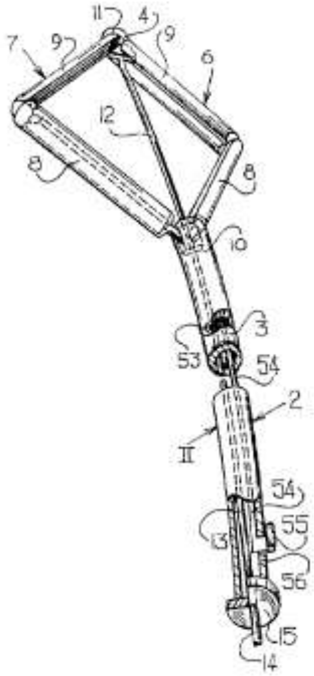

Figure 2.7: Instrument set for laparoscopic hysterectomy from Koninckx (1997).

2.2.3 Fan retractor

Fan retractor has multi-fan blades with an extending laterally end as an end-effector. The extension is achieved by rotation of a control plate or a sliding joint to give a fan-shaped surface. On each blade, there is a slot or groove for guiding the blade to move to a distal end. Josefsen (1993), Matula (1995) and Christian (1998) have their patents issued by the United States.

Josefsen (1993) got his patent published by the United States. The patent is related to a surgical retractor that has an elongated tubular structure and a proximal end. The end-effector is composed of multiple fan blades attached at the end of the elongated tubular structure. The closed position is where the blades are stacked, and the open position is where the blades deployed in a fan construction.

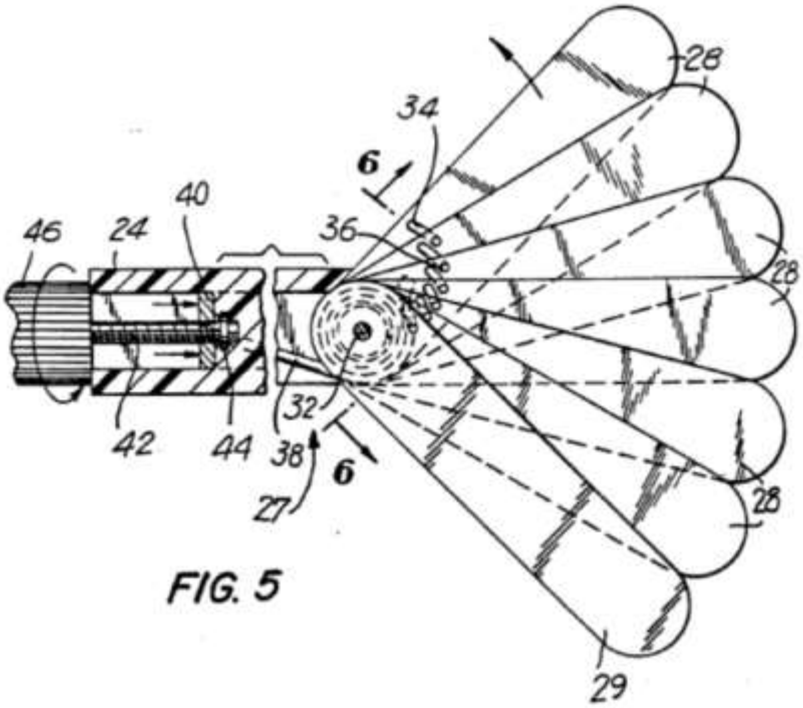

FIG. 5

Figure 2.8: Surgical retractor designed by Josefsen (1993).

Matula (1995) and his group presented a patent of a surgical retractor issued by the United States. This medical retractor is a fan-shaped effector connects to the end of a tubular element. The tubular element extends from the handle portion which involves an actuating structure for driving the fan blades.

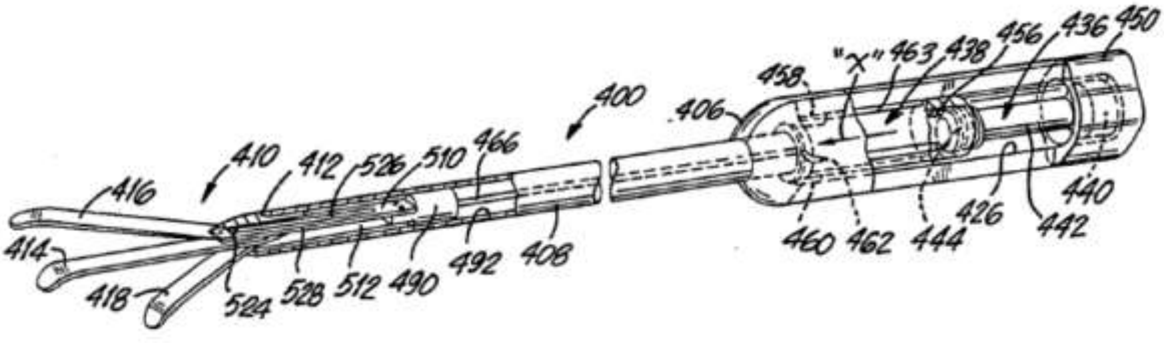

Figure 2.9: Surgical retractor created by Matula (1995).

Christian (1998) and his group got a patent issued which is related as a laparoscopic retractor. The retractor has a plurality of fingers which extends from an end-effector. For getting the extension, the centred control plate, which is connected to the handle, needs to be rotated. In his design, each blade has a slot. The slot guides the pin to move through and drives the fan to extend or collapse.

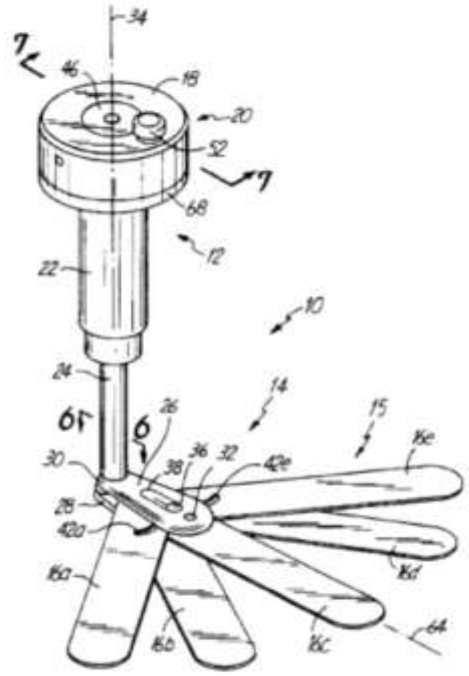

Figure 2.10: Laparoscopic retractor made by Christian (1998).

2.3 Retractor control

In colorectal surgery, the retractor establishes the area and assists in finding the target tissue. There are some drawbacks by using hand to drive the retractor. First, the hand may get stressed and tired after holding the retractor for a long time. This may mislead the surgeon to the incorrect location of surgery. As the inside tissue are tender, the misleading may cause unexpected bleeding or trauma. Second, hand holding has limitation of operating orientation. During operation, surgeon cannot let go the instruments so that if surgeon wants a particular retractor orientation, then, his hand may presents an uncomfortable position and feel lack in strength. Third, hand control has undesired wobble which may damage the tissue as well. For more precise surgery result, the hand-hold retractor needs to be replaced by a robotic retractor. The robotic retractor driven by a manipulator has more accuracy during operation. Without using one hand to hold the retractor, the surgeon can better focus on the surgery.

2.4 Robotic control of the retractor

People operate robots to complete high-intensity job since the telecontrol manipulator was created. Most of the transferring, conveying, welding and spraying robots are position control robots, while the conventional control systems are now matured after years' development. However, conventional robots are not capable to do works like assembling, polishing and burring because position error may cause damage to the robot or the object without force control. Different from the conventional robots, active controlled robots system is proposed with both force control and position control. In the last few decades, active control methods have been a key research direction. With the development of computing, sensor technique, materials science, mechanical engineering and control theory, the intelligence of robots is rapidly improving and successive outstanding robots rely on demanding force control systems have been developed, for example, surgical robots and rehabilitation training robots (Chen et al., 2009; Ha et al., 2002; Hurd et al., 2005; Nagata et al., 2001; Nef et al., 2007; Schreuder and Verheijen, 2009). However, it is impossible to add new functions based on the traditional position control because the traditional position controllers are close frame system (Hassan et al., 2010; Huang et al., 2008).

The manipulator attached with the dual-head fan retractor in this thesis is featured with active control. The advantage for utilising active control is that the end-effector would not over pushing the internal tissue. Active control can be presented into two parts: impedance control and ~~hybrid~~ position/force control.

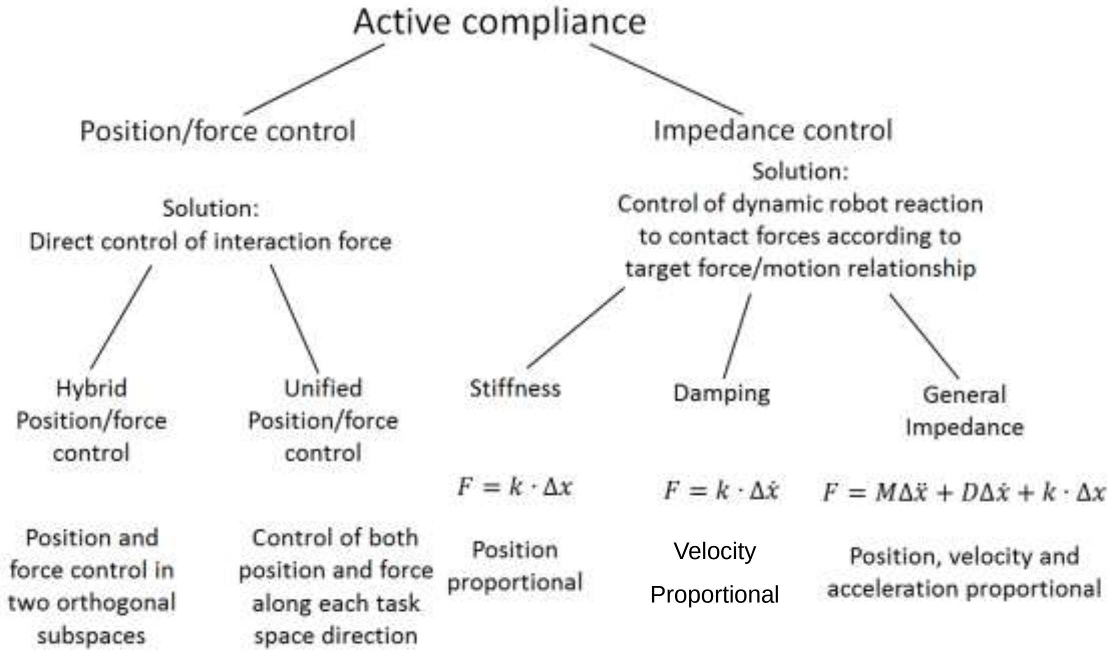

Figure 2.11: Active compliance control methods (Vukobratovic, 2009).

2.4.1 Position/force control

In hybrid position/force control, both desired interaction force and robotic active position are controlled. Impedance control utilises the relationships between the acting force and manipulator position to adjust the mechanical impedance of the end-effector to external forces. (Vukobratovic, 2009)

Hybrid position/force control, (Raibert and Craig, 1981) which controls the end-effector contact force and position tracking at the same time, this control method utilises the orthogonality principle and decomposes the end-effector movement regarding Cartesian coordinates (Bassi et al., 2009). Hybrid position/force control adopts linear feedback control method, like proportional integral derivative (PID) and proportional derivative (PD) directly adjusts the output torque of each joint. As the robot is a non-linear time-varying system, the joint output torque needs to be accurately calculated through the dynamic model. Additionally, the current joint transmission mechanism has backlash, friction and calculating torque error. Thus, the key to hybrid position/force control research is to promote system robustness for the purpose of decreasing interference (Bechlioulis et al., 2009; Katic and Vukobratovic, 2002). Some strategies of position/force control were presented to overcome these drawbacks. Cui and Sarkar (2001) derived a dynamic model for the underwater vehicle manipulator system, which combines impedance control with hybrid position/force control. Wang and Hao (2007) presented an intelligent prediction algorithm which is not only can be applied to impedance controller, but also hybrid position/force controller. Azenha (1997) noted variable structure algorithms in position/force hybrid control of robotic manipulators. Khatib (1986) illustrated an approach for control the motions and active forces of a manipulator based on the operational space formulation. The hybrid control scheme proposed by Bassi (2009) includes position and force controllers based on first and second order sliding modes. Komati (2014) proposed a new method to estimate the environment parameters using force and position measurements.

Although early investigations in active control strategies depend on a foundation for position/force control system, the relevant application range and control effects are insufficient. More works for overcoming complicated and variable environment of position/force robots need to be carried out (Lefebvre et al., 2005).

2.4.2 Impedance control

The design theory of impedance control is to establish the dynamic relationship between end-effector force and position error. Controlling the robot displacement for the purpose of adjusting the end-effector force, and it guarantees robot receive the desired contact force on the restraint direction (Seraji, 1997). This kind of control methods is adjusted in term of the position error, also known as feed-forward control mode. The impedance control methods are generally utilised in applications of assembling and metalworking: drilling, fraising, devilling, polishing, cutting, bending etc (Richardson et al., 2005). In impedance control, the controller structure does not change when the robot is converting from restraint environment, free space motion movement and restraint motion movement.

In impedance control model, end-effector contact force tracking control can be fulfilled based on the impedance control of joint space position control. The effect on system dynamic model, outer interference and force measurement is small, as current industry robots are generally based on joint space position impedance control. However, for increasing the property of force control, the ideal parameters of impedance model must be adjusted with the change of the parameters of the environment dynamic model. In practical experiments, the parameters of the environment dynamic model are unknown in most cases. Thus, that is the key problem of impedance control now (Lee, 2008;

Owen, 2008).

The designs and optimisation of impedance algorithms and controllers are valued highly by scholars and experts. Jung presents a force tracking control scheme for determining the reference trajectory under the condition of an unknown environment (Jung et al., 2001; Jung et al., 2004). An impedance control of dual-arm cooperative manipulator is evaluated by Caccavale (2008). The impedance control system includes a centralised impedance control strategy. Another decentralised impedance control aims at avoiding significant internal loading of the object, which enforces at the end-effector level. Tsuji (2008) states a possibility that anthropopathic strategies can be generated in robot position control, and he developed hand impedance for ball-catching tasks. Dutta (2002) enumerated three different impedance control systems for a robotic grasper. Chang and Jin (2006) proposed the nonlinear target impedance which is better for tracking discontinuous trajectory and more robust against Coulomb friction in free space position control. Wang (2009) presented a fast online estimation method of impedance parameters based on the forgetting factor recursive least squares identification method. Matinfar (2005) described a geometric view on impedance control that minimises a combined generalised position and force trajectory error metric. He proposes a classic quadratic optimal control strategy which is employed to design a novel controller with control parameters based upon environment stiffness and damping. Hogan (1984) formulated that the objective of impedance control is to establish a desired user-specified dynamical relationship, considered as target impedance, between the end-effector position and the contact force. Lee (2008) explained a novel force tracking impedance control strategy in which target stiffness is varied on-line to regulate the desired contact force in an unknown environment.

Chapter 3

Design and control of the retractor

In this chapter, the detailed design of the retractor and its actuation are considered, including the general design architecture, the design of the fan device, the retractor wrist, the axial rotation system and their design validation. Here, the fan device includes the fan end-effector, the expansion mechanism and the clutch-spring mechanism.

3.1 General design of the dual-head fan retractor

The laparoscopic colorectal procedures can be divided into five steps. The first step is finding the target tissue which is assumed to have been marked earlier through endoscopy; the second is establishing an appropriate and feasible operational working space; the third is cutting the target tissue and launching the extraction; the fourth is anastomosis; the fifth is suturing the tissue to reseal the cut.

It is evident that intestine floods easily when little disturbance is applied, which is contributed to intestine mucus decreases the friction between tissues. Hence, it implies that the intestine is not stable although it has been nicely placed and controlled before cutting. During operation, big movements are unappreciated because they may cause intestine flooding. Repositioning of the entire retractor is highly likely to lead worse intestine flooding. Intestine flooding may drown the working space and lead to target tissue missing which may cost time for disposal the working area and recovery to the operation status.

A retractor is utilised as an instrument for establishing a robust plane in operation. In laparoscopic surgery, instruments have to pass through the trocar which is a distinct elongated cannula with a relatively thin cross section from 5mm to 10 mm in diameter to access the operational working space. A traditional laparoscopic retractor has three types of end-effectors, they are: the polyarticular retractor with a polyarticular pole end-effector; the plane retractor with a broad paddle end-effector; the fan retractor with multi-fan blades end-effector.

In this chapter, the dual-head fan retractor for laparoscopic colorectal surgery has a similar design with the traditional fan retractor. Figure 3.1 shows the schematic of the general design of the dual-head fan retractor. The dual-end fan retractor consists of a handle, a tubular element, a wrist and two fan expansion devices. The handle includes five operational buttons and two printed circuit boards (PCBs) which drive two gear motors by manipulating the five buttons. The tubular element is a combination of a cylinder at one end and an elliptic cylinder at the other end. Two gear motors are attached to the cylinder of the tubular element. The two fan devices are confined by the tubular element because their housings and the internal holders are located in the localisation holes of the tubular element. The wrist encloses the elliptic cylinder of the tubular element.

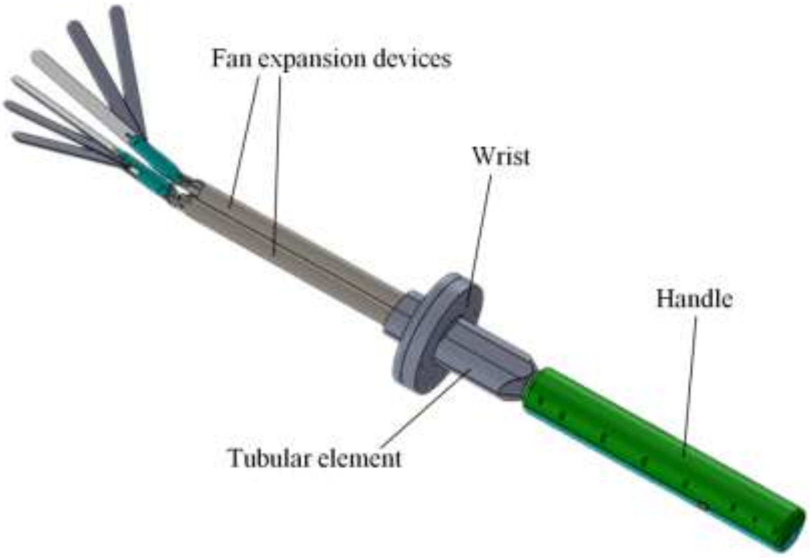

Figure 3.1: The overall schematic of the dual-head fan retractor.

The fan-shaped end-effectors of the fan devices which rely on their anthropoid hand-holding shape efficiently help with establishing operational working space. Moreover, the hand-holding angle of the fan devices is adjustable. Furthermore, the axial rotation of the front body (from fan devices to tubular element) is motorised so that the rotational motion has more accuracy when implementing a servo command. The advantages result in three benefits: first, the hand-holding shape is more efficient for operating the slippery and massive intestine; second, the adjustable hand-holding angle can push away obstacles without repositioning the entire retractor, especially when the intestine approaches from one side; third, the motorisation of the axial rotation reduces the range of movement which eliminates operational disasters to a maximum extent. Therefore, the dual-head fan retractor is worthy of further research and development.

3.2 Design of the fan device

Each of the fan devices is composed of a fan-shaped end-effector, an expansion mechanism and a clutch-spring mechanism.

The design of the fan device is a fan-shaped end-effector attached at the end of a long pole as shown in Figure 3.2. There are two types of fan devices, one is a rotatable fan device, and the other is a non-rotatable fan device. The rotatable fan device has one rotatable tubular joint and one normal tubular joint, while the non-rotatable fan device has two normal tubular joints. Both tubular joints are tubular sections combined with a bar located on its bottom used for depressing the trigger of the clutch-spring mechanism. The bar of the rotatable tubular joint is longer than that of the normal tubular joint, which helps rotating the rotatable fan device. The non-rotatable fan device is fixed by the grooves on the tubular element, which constrains the rotating of the non-rotatable. The coordination of the rotatable and non-rotatable fan devices forms an anthropoid hand-holding shape. Compared with the plane shape of the traditional retractor, the hand-holding shape retractor is more effective in holding and moving the intestine, because it has bigger holding volume.

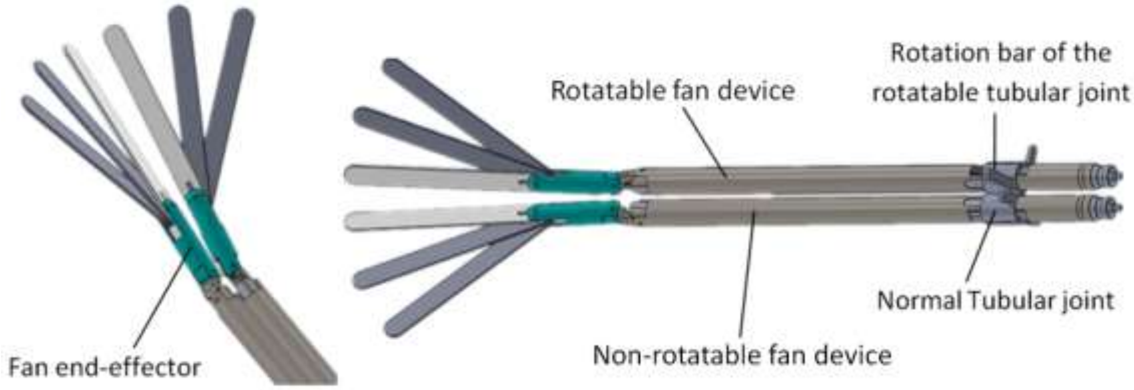

Figure 3.2: Schematics of a holding shape retractor and the fan devices.

As shown in Figure 3.3, the detailed structure drawing presents the assembly of the laminated stainless steel bars. The elongated, thin, laminated stainless steel bars connected by a welded joint are the key components for fan expanding and collapsing. The laminated bars which can bend slightly are rigid in the axial direction and can swing about a normal axis. By pushing or pulling the laminated bars in the axial direction, the expansion and collapse of the fan end-effector is facilitated. By manually pulling back the trigger of the clutch-spring mechanism, the two palms of the fan devices are able to bend laterally about a normal axis. This function is explained in detail in a latter section regarding the clutch-spring mechanism.

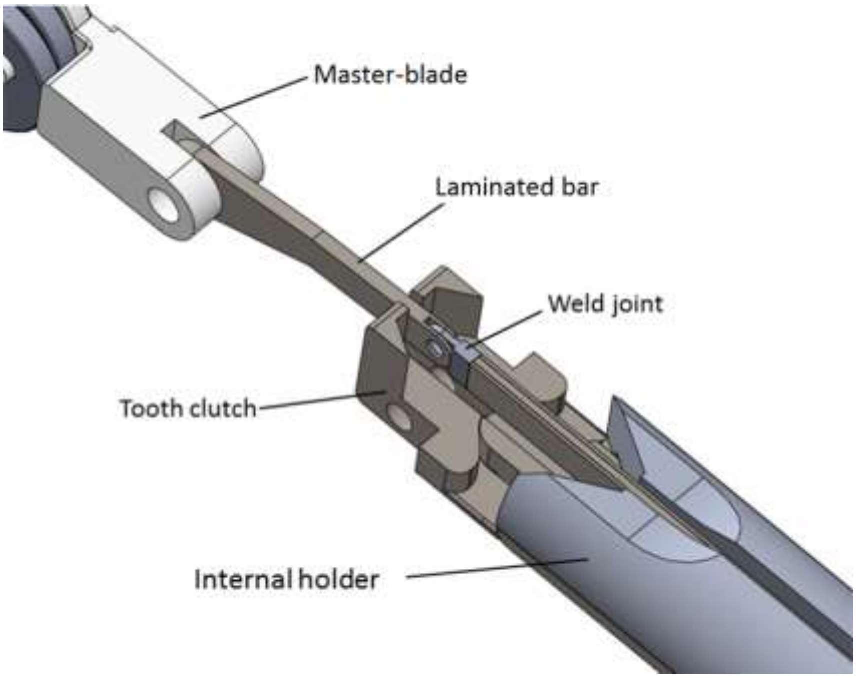

Figure 3.3: Structure drawing of the elongated stainless steel laminated bar.

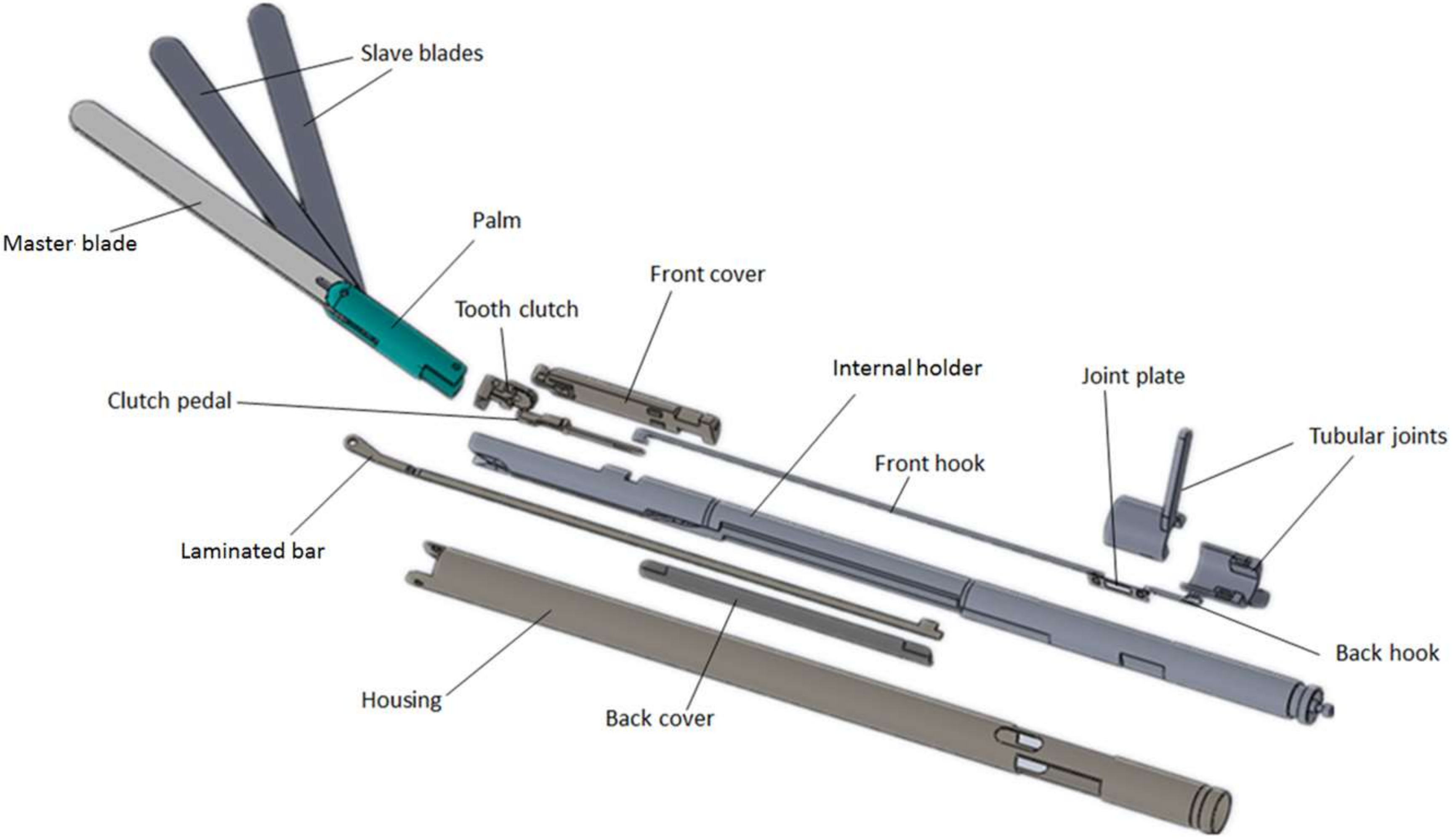

Figure 3.4: The exploded view of the dual-head fan device.

3.2.1 Fan end-effector

There are two fan end-effectors in the dual-head retractor, and each one is attached to a fan device. The fan end-effector is a fan shaped mechanism attached at the end of a long pole. The fan end-effector consists of one master blade, two slave blades, three pin joints and a retractor palm as shown Figure 3.6. For meeting the surgical requirements, the fan end-effector is designed as two anthropoid fan-shaped planes when expands and two elongated poles when collapses.

In Figure 3.5, it shows the diagrams of the master blade and two slave blades. Each blade has a long slot. The slot of the master blade is a straight slot; one of the two slave blades has a slot which has a radian; and the other slave blade has a slot which has a bigger radian. The three blades are connected by two pins. When the pin in the slots is at the right end, three blades overlap closely and present a pole shape. When the pin in the slots is at the left end, two slave blades expand to their maximum angles and present a fan shaped plane.

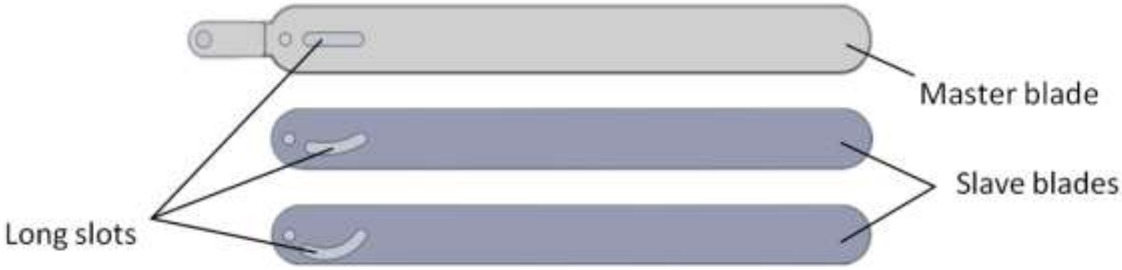

Figure 3.5: Diagrams of the master blade and two slave blades.

The master blade connects with the two slave blades through the first pin joint as shown in Figure 3.6. The second pin joint concentrically fixes the retractor palm and the three blades. The third pin joint links the master blade with the laminated bar of the expansion mechanism. When the master blade moves backwards, the fan closes and the three blades return to their original state, and the retractor takes the form of an elongated pole.

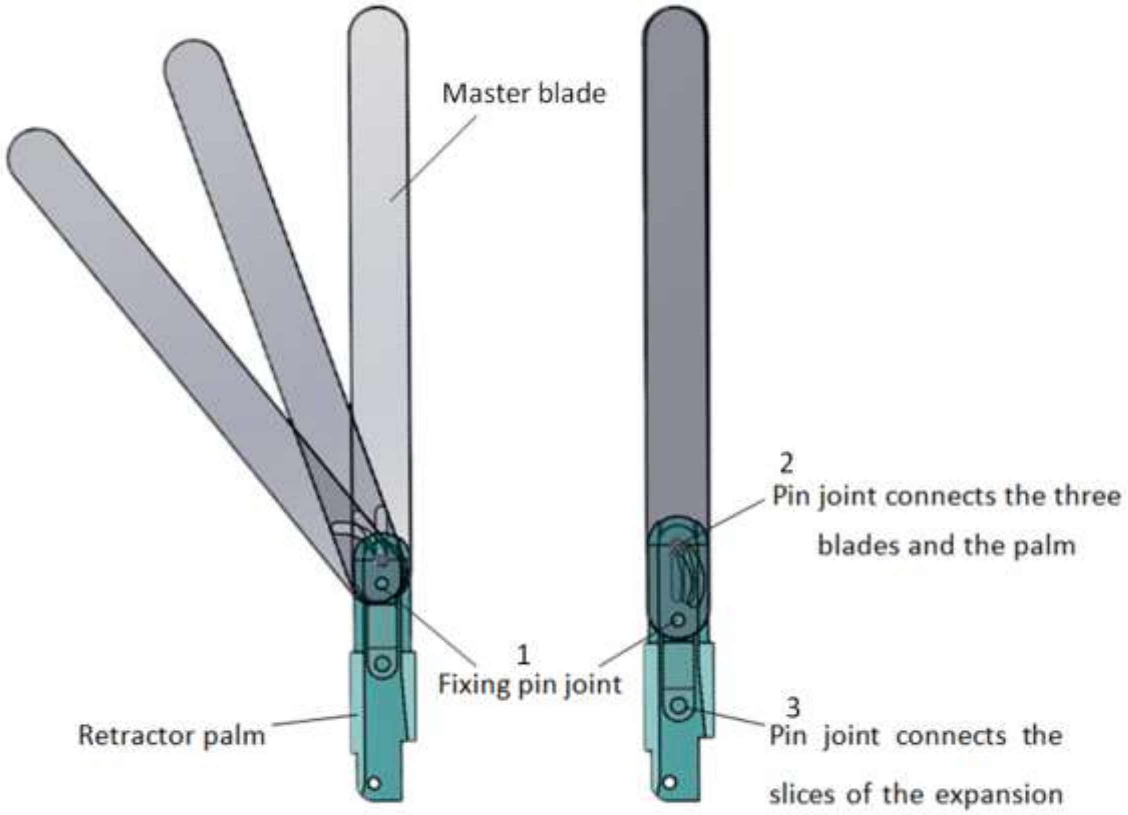

Figure 3.6: The schematics of the fan end-effector.

To control the maximum of two slave blades, we established a mathematic model in order to calculate the angle values of two slave blades. Below is the code created in MATLAB that calculates the angle values of two slave blades,

```
syms x y c d
[x,y]=solve('(x+6)^2+(y-3.6)^2=6.995^2','x^2+y^2=2.37^2') ;
[c,d]=solve('(c+2.4)^2+(d-3.6)^2=4.315^2','c^2+d^2=2.37^2') ;
x=double(x(1,1));
y=double(y(1,1));
phi=90-atan(y/x)*180/3.1415926
c=double(c(1,1));
d=double(d(1,1));
theta=90-atan(d/c)*180/3.1415926
```

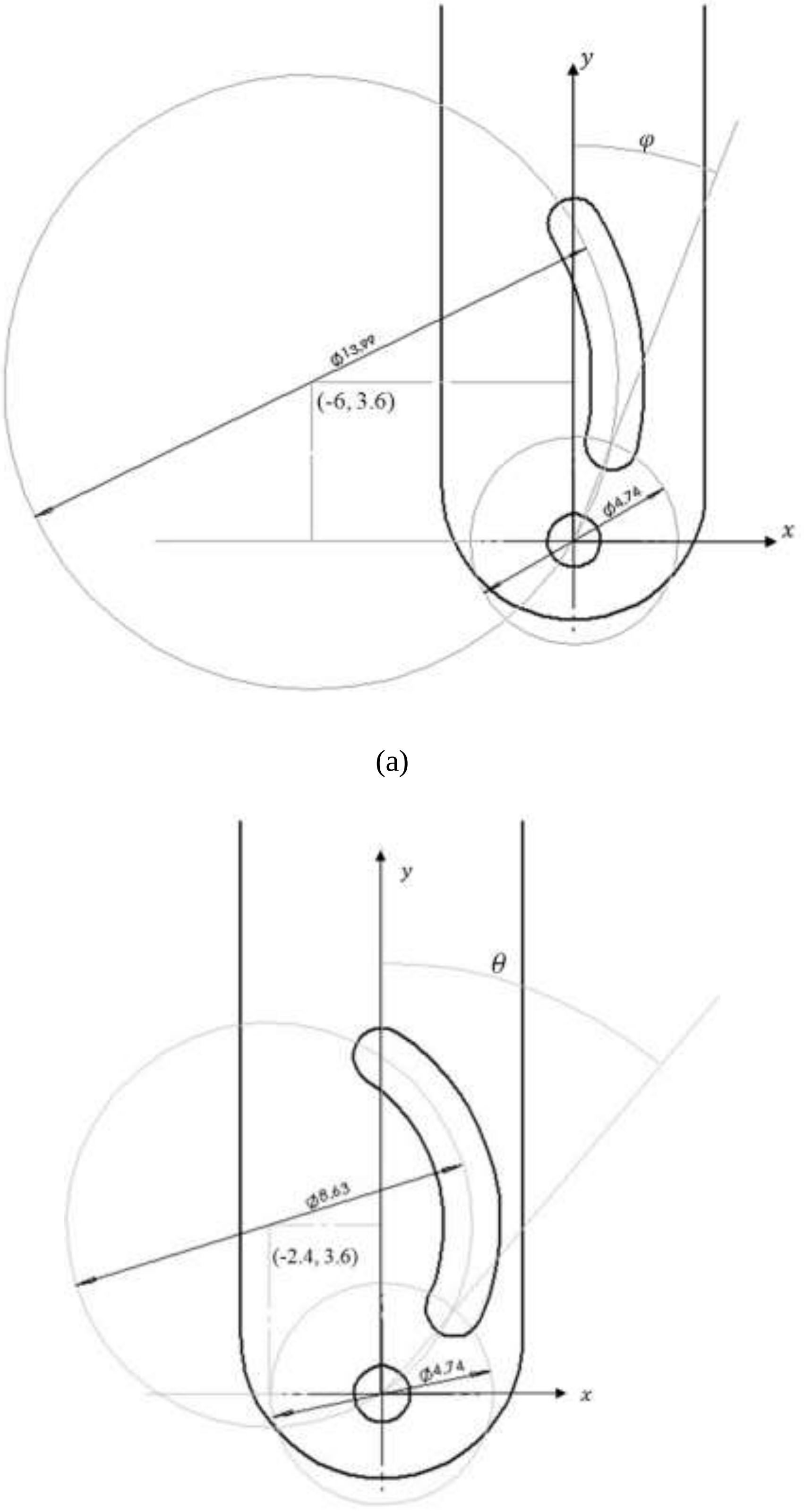

(a)

(b)

Figure 3.7: (a) The groove on fan salve blade I; (b) The groove on fan slave blade II.

Get

$\varphi = 21.1854\,^{\circ}$, $\theta = 40.3978\,^{\circ}$

Have two blades angles increase to 21.1854° and 40.3978° separately. In this case, when the sliding joint moves forwards and backwards, the fan blades obtain different joint values.

3.2.2 Expansion mechanism

The expansion mechanism facilitates the expanding or collapsing of the fans and each fan devices has an expansion mechanism. As explained in the design of the fan end-effector, the collapsing and expanding motions are implemented by moving the master blade upwards and backwards. That makes the master blade an essential component of the expansion mechanism. The master blade connects to the heads of the three elongated stainless steel laminated bar by using a pin joint. The ends of the stainless steel laminated bar dual-headed slider are caught by a pushing bar as shown in Figure 3.9, while the bottom of the pushing bar is clamped by the head of a dual-headed slider. The dual-headed slider, a screw and a gear motor constitute a sliding joint transmission and the sliding joint transmission makes the upward and backward movement of the master blade achievable. The end-effector opens when the master blade moves upwards, and the end-effector collapses when the master blade moves backwards. In Figure 3.8, when the end-effector fully opens, there is a 15° angle between the axial and the palm according to the design of the stainless steel laminated bar.

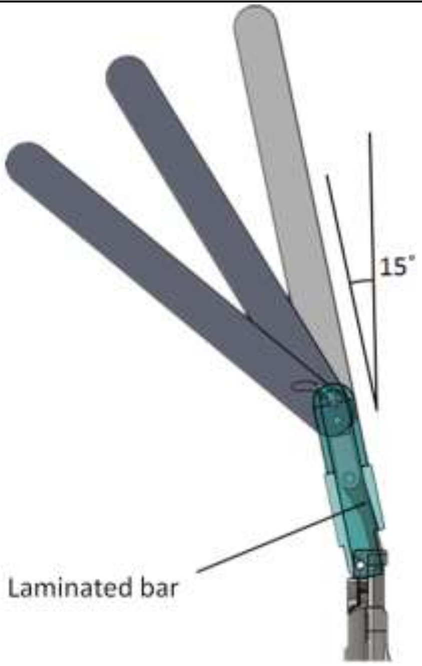

Figure 3. 8:The left view of the end-effector

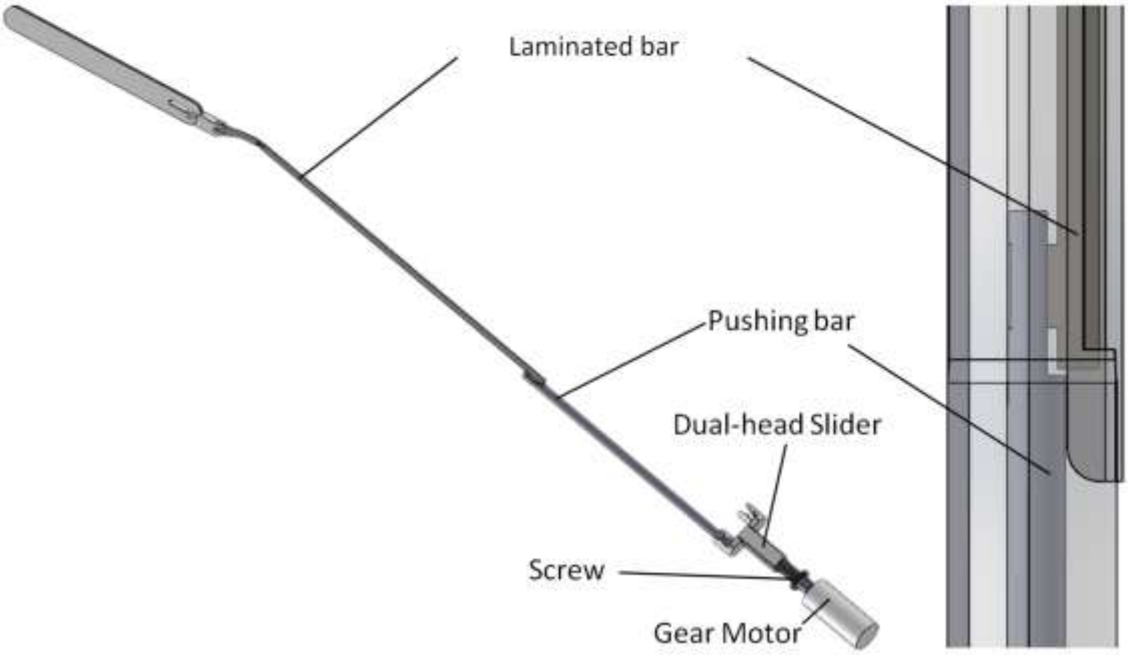

Figure 3.9: The diagrams of the expansion mechanism.

As explained in the preceding section that the master blade is a key component for the expansion mechanism and the master blade attaches to the dual-headed slider through the laminated bar and the pushing bar (Figure 3.9). For achieving the linear master blade movement, the sliding joint transmission is used. The sliding joint transmission inherently operates by conversion of rotary movement to linear movement. Normally, a conversion of the linear motion of the sliding joint transmission is accomplished by a screw, cam, and wheel and axle, assembly where the screw mechanism includes a lead-screw, a screw jack, a ball screw and a roller screw (Anaheim Automation, 2016). Here, the lead-screw is utilised by using a gear motor and a screw. The lead-screw mechanism implements conversion from rotary movement to linear movement. The types of lead-screw are classified into the square thread, acme thread, buttress thread, the British standard Whit worth thread and the V-thread according to the geometry of their threads. Each external thread matches a corresponding internal threaded hole constituting a screwed fastener.

The terms associated with the screw threads are discussed in Appendix B.

In Figure 3.10, it shows part of the schematic of the sliding joint transmission. The gear motor in the figure is fixed on the tubular element. The screw connects with the gear motor through a pin hole. An annular terraced washer attached to the tubular element and fixed to the gear motor shaft to prohibit the translational movement of the screw. That means the screw can only produce rotational movements without translational movements when driven by the gear motor. In Figure 3.11 there are two heads attached on the dual-headed slider. Each of the heads clamps a pushing bar which pushes on the master blade through the laminated bar.

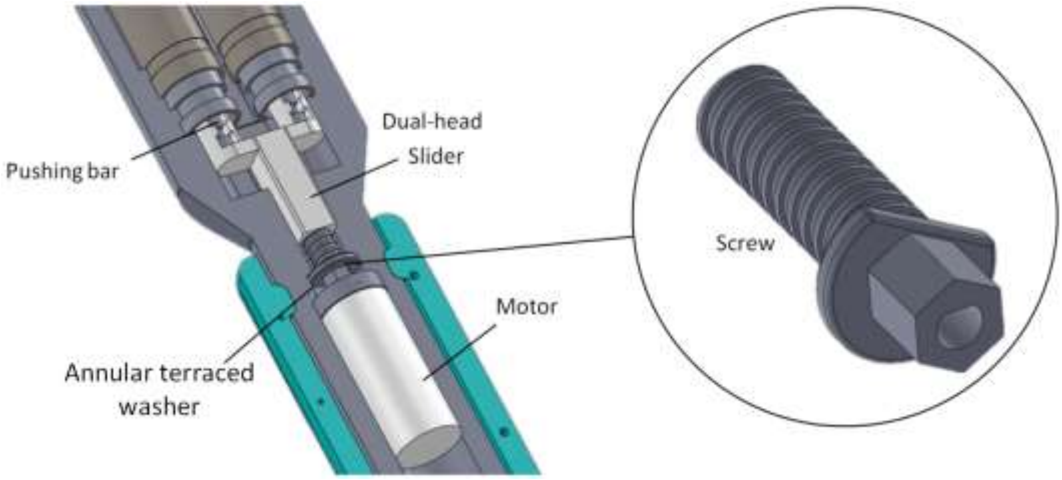

Figure 3.10: The scheme of part of the sliding joint transmission.

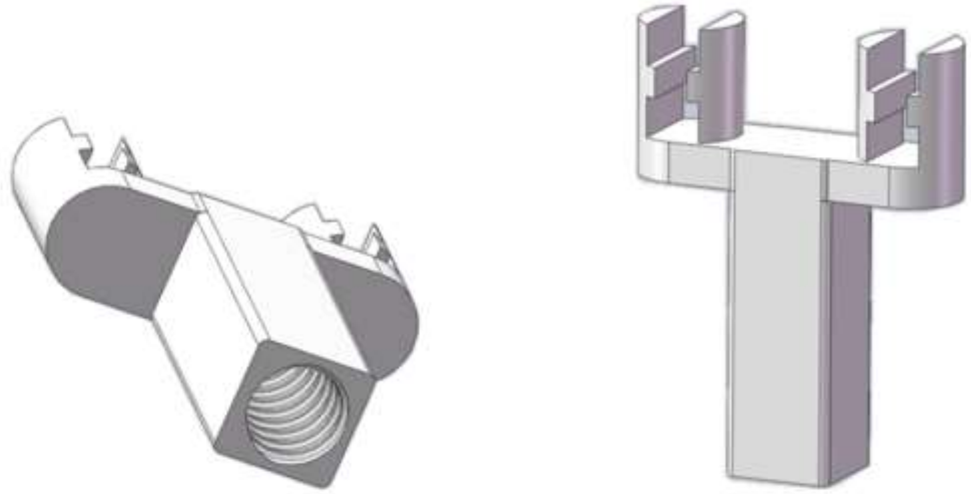

Figure 3.11: Physical diagram of the dual-headed slider.

In the sliding joint transmission, the gear motor provides the power source. According to the design of the fan end-effectors, the three blades expand to a fan shape when each of the master blades moves upwards. When the screw rotates in the forward direction, the screw pushes out the dual-headed slider. The dual-headed slider then drives the two master blades forward which push the fans to expand. When the screw rotates in the reverse direction, the screw pulls back the dual-headed slider. The dual-headed slider then pulls back two master blades which cause the fans to collapse.

3.2.3 Clutch-spring mechanism

The clutch-spring mechanism aims to support the fan end-effector palms to obtain desired angles. The concept of the clutch-spring mechanism follows the design of gear transmission. The clutch-spring mechanism is attached on the internal holder of the fan device. As shown in Figure 3.12 to Figure 3.16, the clutch-spring mechanism consists of an internal holder, a tooth clutch, a clutch pedal, a spring, a front hook, a joint plate, a back hook and two tubular joints.

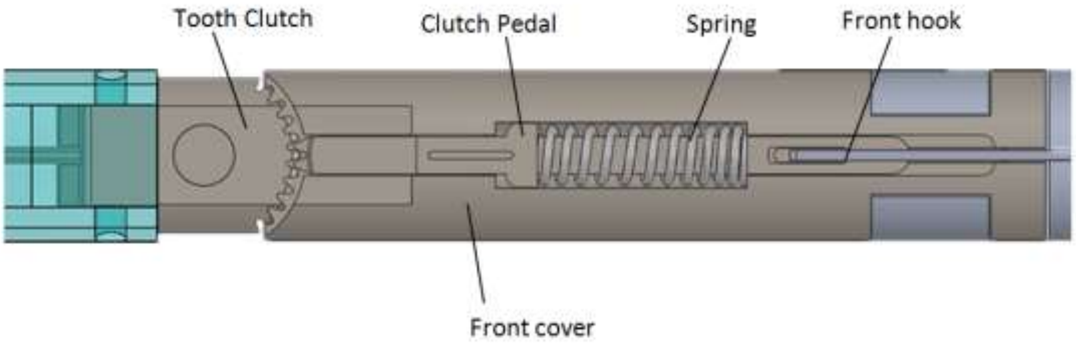

Figure 3.12: Front view of the front of the clutch-spring mechanism.

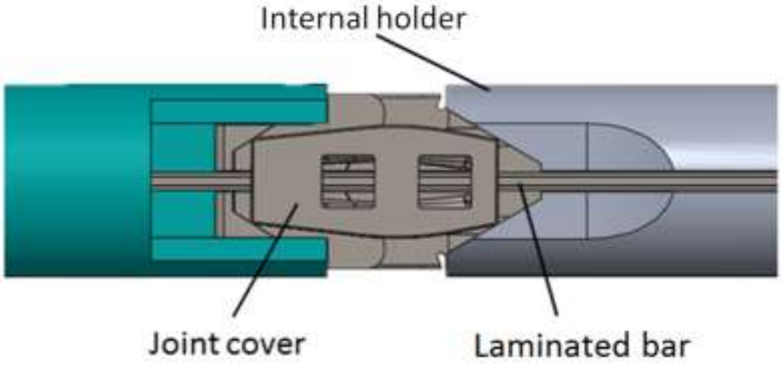

Figure 3.13: Back view of the front of the clutch-spring mechanism.

The whole clutch-spring mechanism is based on the internal holder. The front of the clutch-spring mechanism is attached on the front cover as shown in Figure 3.12. In Figure 3.13, the laminated bar is covered by a joint cover. When the palm rotates, the joint cover helps the laminated bar to provide smooth bending pose. When the trigger of the clutch-spring mechanism is not activated, the spring pushes the clutch pedal towards the tooth clutch so that the retractor palm is not capable for rotating. The front hook connects with the clutch pedal in order to combine the front of the clutch-spring mechanism with the rear of the clutch-spring mechanism.

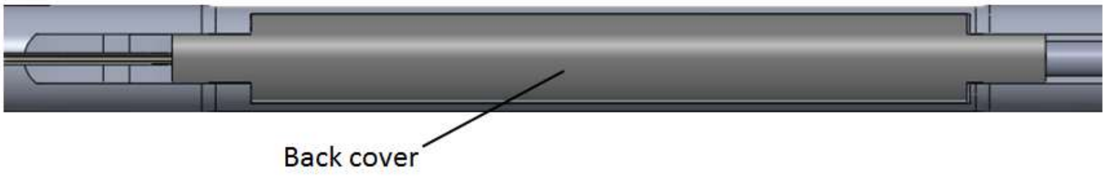

Figure 3.14: Back view of the back of the clutch-spring mechanism.

The back cover in Figure 3.14 has a groove which holds the laminated bar. This design allows the laminated bar to move along the groove and to provide axial pull/push movement.

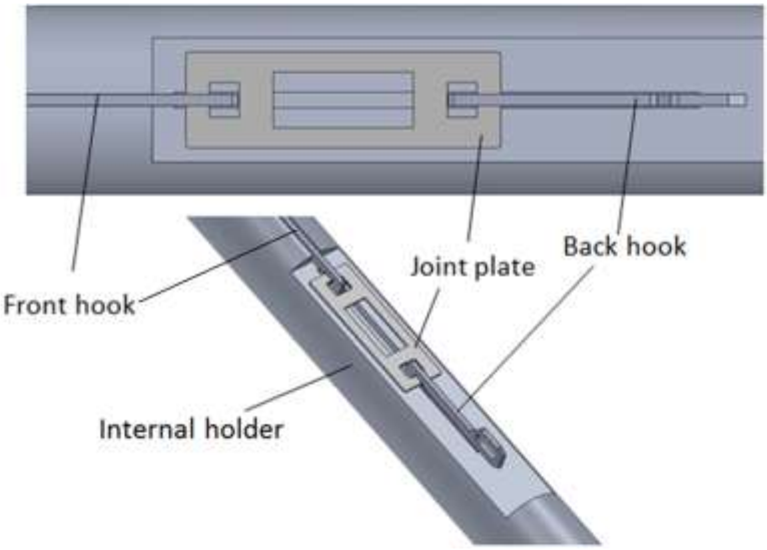

Figure 3.15: The rear concept diagrams of the clutch-spring mechanism.

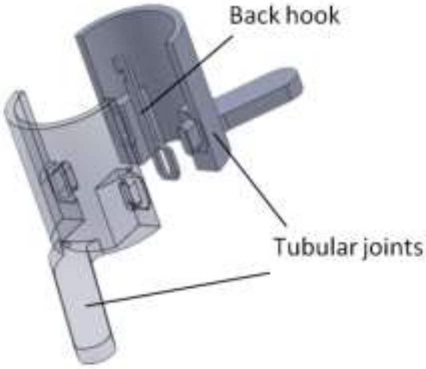

Figure 3.16: The schematics of the tubular joints.

In Figure 3.15, the tubular joints clamp the back hook which connects the terminal of the front hook through the joint plate. The head of the front hook links the clutch pedal, and the spring wraps the mid-body of the clutch pedal. The teeth of the clutch pedal and the teeth of the tooth clutch are fitted. When tubular joints are pulled back, the front hooks pull the clutch pedals backwards against the springs that allow the tooth clutches to rotate (the palms are able to rotate) and the maximum rotation value is ± 30^{o} which makes the anthropoid hand motion achievable. Loose the tubular joints after the palms reaching the desired angles. Meanwhile, the clutch pedals, pushed by the spring, get their tooth access into the tooth sockets of the tooth clutches for fastening the end-effector palms. The elastic springs push the clutch pedals towards the tooth clutches and preserve the desired angles of the fan end-effector palms. There is non-interference between the two fan devices so that they can present different palm angles at the same time. The advantage of the clutch-spring mechanism is that two fan end-effectors are capable for multiple hand-holding shapes.

3.3 Design of the retractor wrist

The retractor wrist consists of an internal annular region and an external annular grip. The external annular grip encloses the internal annular region. The retractor wrist is used for pulling back tubular joints to trigger the clutch-spring mechanism. Additionally, the retractor wrist is utilised for rotating the rotatable fan device rotational.

3.3.1 Triggering for clutch-spring mechanism

Figure 3.17 shows the top view of the tubular joints and the left view of the tubular joints and the internal holder. The internal holder has two grooves on its two sides, and the tubular joints clamp on the internal holder through these two grooves. The tubular joints restrict the rotational freedom of the internal holder. That means the internal holder rotates when the tubular joints rotate and the tubular joints are capable of moving up and down along the grooves of the internal holder. There is a small gap on the internal holder grooves which allow the tubular joints to move upwards and backwards. Therefore, the tubular joints move along the gap for triggering the clutch-spring mechanism.

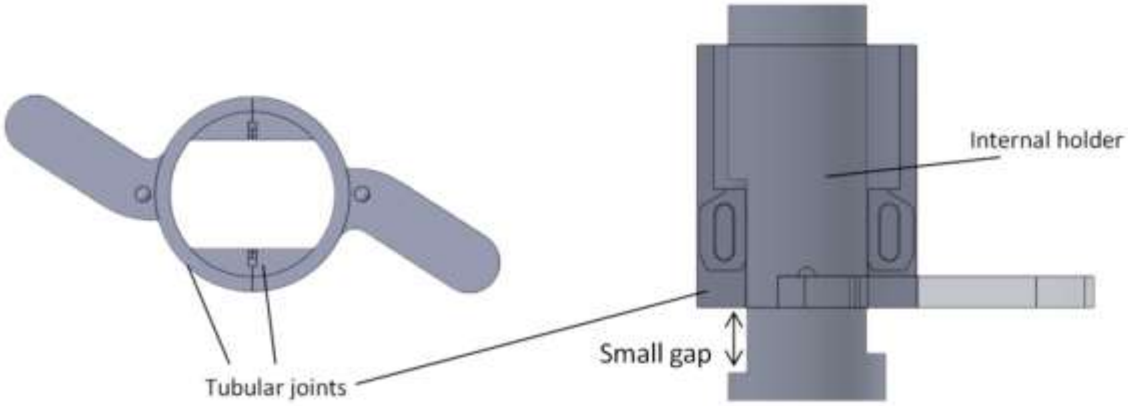

Figure 3.17: Top view of the tubular joints; Left view of the assembly comprised of tubular joints and the internal holder.

3.3.2 Rotational capability of the rotatable fan device

As shown in Figure 3.18, there are holes on the internal annular region and six ball plungers are installed in the screw holes on the external annular grip. The balls which are spring loaded in the plunger pulled back by the internal annular region before approaching the holes. Rotate the external annular grip, the spring loaded ball slip from one hole to another hole. The holes are close to each other for getting smooth angle change. It is 5˚ variation whenever to move to the next hole.

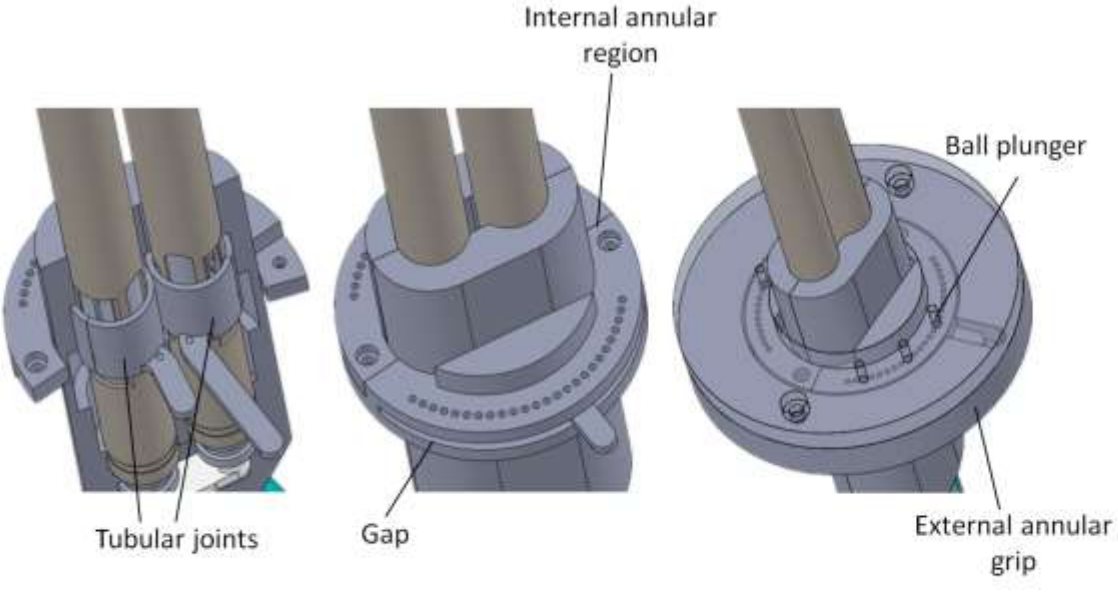

Figure 3.18: Diagrams of the wrist.

The ball plunger is a device that is used for releasing stoppages in spring plumbing. In this thesis, six M4 ball plungers have been installed in the external annular grip. The mechanical parameter of the ball plunger has shown below.

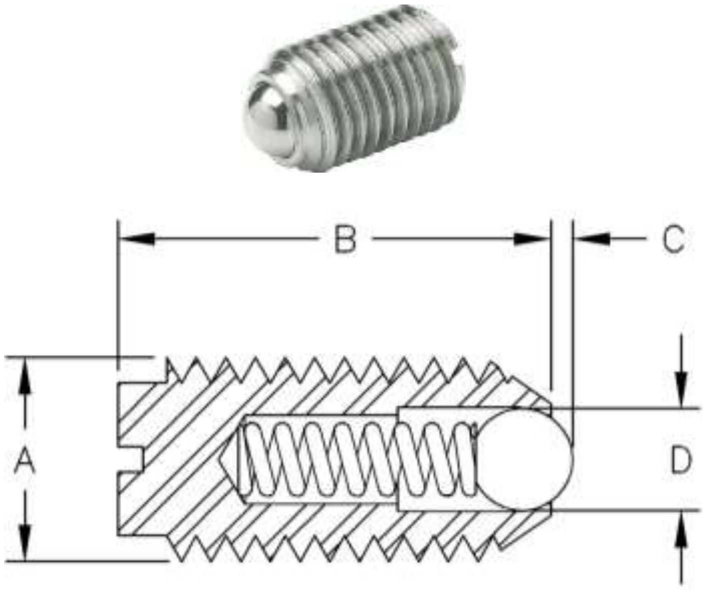

Figure 3.19: Mechanical drawing of the M4 ball plunger (Springplungers, 2015).

Table 3.1: Mechanical parameter of M4 ball plunger (Springplungers, 2015).

D	C	B	A	Super light load		Light load		Heavy load		Super heavy load	
				Min.	Max.	Min.	Max.	Min.	Max.	Min.	Max.
2.5mm	0.8mm	9mm	M4	0.6N	1.6N	2N	4.9N	3.9N	9.8N	2.5N	12.5N

3.4 Axial rotation of the front body

In Figure 3.20, the transfer shaft connects with the shaft of the gear motor through a coupling. The transfer shaft is a combination a 25mm long cylinder section and a 2.5mm long cube section. The cube section clamped by the cube groove of the handle. On the other side of the transfer shaft, the gear motor is fixed on the tubular element. Therefore the tubular element rotates relative to the handle when the gear motor rotates. There is a slip wire ring assembled at the end of the tubular element to make the wires of the gear motors rotating together with the tubular element at the same time.

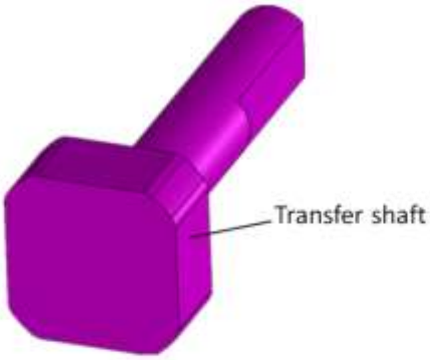

Figure 3.20: Schematic of the transfer shaft.

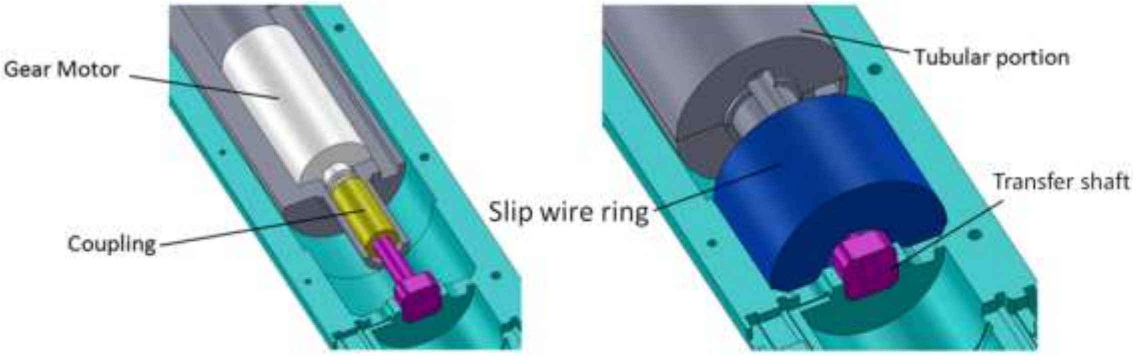

Figure 3.21: Schematics of Co-axial spin system of the tubular element.

Figure 3.22: Photos of slip wire ring and coupling.

Slip wire ring is a ring sized integrated unit with housing and bearings. There is a capsule inside the slip wire ring which is a rotational device. The twist capsule is used typically in scanning applications where continuous rotation is required. It helps wires to rotate without rotating to a mess.

The motor selection and driver control of the dual-head fan retractor are discussed in Appendix C.

3.5 Stress analysis of the dual-head fan retractor

3.5.1 General information of the large intestine and small intestine

In laparoscopic colorectal surgery, the working area is beneath the abdomen. Retractor moves among large intestine and small intestine and does jobs like lifting, pushing and establishing working space. Below is a table describes the approximate dimension and weight of large intestine and small intestine.

Table 3.2: The approximate dimension and weight of large intestine and small intestine.

	Large intestine	Small intestine
Weight	2 kg	1.75 kg
Length	1500 mm	6000 mm
Diameter	65 mm	40 mm

One retractor has good serving life, lower cost and high reliability is desired. Strict studies about the cost competitiveness, availability of materials, manufacturing facilities and the suitable mechanisms for the retractor have been investigated.

3.5.2 Information of the expanding end-effectors and force detail

The expanding end-effectors of the dual-head fan retractor are two fan-shaped planes and each of the end-effectors consists of three fan blades and a retractor palm. For obtaining the necessary reliability, the dual-head fan retractor needs to be robust and does elastic deformation when operated. The elastic deformation is desired because this type of deformation is reversible so that once the tensile is unloaded the components get back to its original shape. In Figure 3.23, it shows one of the working shapes of the end-effectors during operation. This working shape has the biggest touching area so that the largest stress appears when end-effectors stay in this state.

The detailed stress analysis of the expanding end-effectors is discussed in Appendix A.

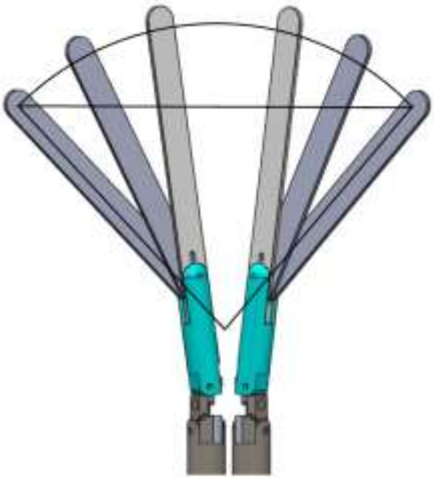

Figure 3.23: Diagram of the holding shape.

3.6 Kinematic and functional description of the complete retractor

After surgeon makes small incisions on the abdomen and settles the trocar, the collapsed dual-head fan retractor goes through the trocar. Then, the dual-head fan retractor would be able to reach the inside tissue beneath the abdomen. The end-effectors of the fan retractor open like hands shape and push away the internal tissues when the surgeon is looking for the target tissue. Later on, the end-effectors help to create a suitable working area after surgeon finds the abnormal target. During these moments, retractor does axial rotation, wrist spinning and motion optimisation to help the surgeon to locate the target and establish a comfortable working space. Finally, the surgeon collapses the dual-head fan retractor and pulls it back through the trocar after surgeon finishes the colorectal surgery.

3.7 Summary

This chapter presented the design and control of the dual-head fan retractor and it also included the stress analysis of the retractor. Later, the chapter discussed the kinematic and functional description of the retractor.

The general design of the dual-head fan retractor is divided into three sections. The first is design of the fan device. The second is design of the retractor wrist. The third is design of the axial rotation. Here, the fan device has three parts, the fan end-effector, expansion mechanism and clutch-spring mechanism. The retractor wrist has two functions. First, it is the trigger for clutch-spring mechanism. Second, it is the trigger for rotate the rotatable fan device. Then, in this chapter it provides the stress analysis of the dual-head fan retractor. The stress loaded on the retractor end-effector is calculated. Then, the material for building the retractor has been illustrated. The SolidWorks is utilised to obtain the result of the stress analysis.

Chapter 4

Mathematical modelling of retractor: Dynamics and actuation

The end-effector of the retractor is a multi-body system. In this chapter, the dynamics of multi-body systems will be illustrated. The dynamics of multi-body system includes the approach of Newton-Euler, the recursive Newton-Euler formulation and Lagrangian method. Then, the Jacobians are described. Later, the Lagrangian dynamics and mathematical model of the fan blades are considered.

4.1 Dynamics of multi-body system

A complete understanding of manipulator dynamics is essential for investigating the relationship between the body movement and the force. The manipulator dynamics is the basis for solving two problems: First, to calculate the movement of the link in response to the force or torque applied on the link; second, to calculate the force and torque necessary to move along the trajectory, with a certain velocity and acceleration. Manipulator dynamic problems have been dealt with substantially based on the methods developed by Newton and Euler, Lagrange, Gauss, Kane, Roberson and Wittenburg. In this thesis, only the Newton-Euler and Lagrange methods are used and described in some detail.

4.1.1 The Newton-Euler approach

Robot manipulator links are connected with each other by joints. Here, each link is considered as a rigid body. Characterise the mass distribution of the robot manipulator once when the location of the centre of mass and the inertia tensor of the rigid body have been aware of.

Consider one of the links of the manipulator as a rigid body, the centre of mass is accelerating $\dot{\boldsymbol{v}}_c$. The force **F** is acting on the centre of mass which drives the acceleration. Get Newton's equation (Craig, 2005)

$$\mathbf{F} = \boldsymbol{m}\dot{\boldsymbol{v}}_c \tag{4.1}$$

Here, $\boldsymbol{m}$ is the mass of the manipulator link.

When the manipulator link is rotating with an angular velocity and acceleration which causing by a torque, get the Euler's equation (Craig, 2005)

$$\boldsymbol{\Gamma} = \boldsymbol{I}_c\dot{\boldsymbol{\omega}} + \boldsymbol{\omega}\times(\boldsymbol{I}_c\boldsymbol{\omega}) \tag{4.2}$$

where $\boldsymbol{\omega}$ is angular velocity, $\dot{\boldsymbol{\omega}}$ is angular acceleration, $\boldsymbol{I}$ is the inertia tensor and n is the acting torque.$\{\mathrm{c}\}$ notes the centre mass of the manipulator link. The $\boldsymbol{I}_c$ is defined as a 3×3 symmetric matrix. $\boldsymbol{\Gamma}$ is torque acting on the body to cause motion. It is the characteristics of mass distribution. (Craig, 2005)

$$\boldsymbol{I}_c = \begin{bmatrix} I_{xx} & -I_{xy} & -I_{xz} \\ -I_{xy} & I_{yy} & -I_{yz} \\ -I_{xz} & -I_{yz} & I_{zz} \end{bmatrix} \tag{4.3}$$

In equation 4.3, the elements I_{xx}, I_{yy} and I_{zz} are the mass moment inertias for coordinate *x, y* and *z*. (Craig, 2005)

$$\begin{aligned} I_{xx} &= \iiint_V (y^2 + z^2)\rho dV \\ I_{yy} &= \iiint_V (x^2 + z^2)\rho dV \\ I_{zz} &= \iiint_V (x^2 + y^2)\rho dV \end{aligned} \tag{4.4}$$

The rest of the elements I_{xy}, I_{xz} and I_{yz} are the products of inertia.

$$\begin{aligned} I_{xy} &= \iiint_V xy\rho dV \\ I_{yz} &= \iiint_V yz\rho dV \\ I_{zx} &= \iiint_V zx\rho dV \end{aligned} \tag{4.5}$$

where ρ is the density of the rigid body, dV is the differential body volume.

The iterative Newton-Euler dynamic problem is to calculate joint torque according to the trajectory. Assume that the position, velocity and acceleration of the joint are given. The Newton-Euler dynamic formulation can be implemented recursively. The recursive implementation is discussed in the next section.

4.1.2 The recursive Newton-Euler formulation

The recursive Newton-Euler dynamic formulation has two sections. The first step is to outward the velocities and accelerations for the links and obtains the torques of the links by using Newton-Euler formulation. The second step is to inward the torques of the links and to calculate the joint force (Craig, 2005).

Outward iterations

For getting the inertial forces acting on each link, we need to compute the rotational velocity and linear and rotational acceleration of the centre of mass. The computation starts with link one and outward to link *n*. (Craig, 2005)

$${}^{i+1}\boldsymbol{\omega}_{i+1} = \begin{cases} {}^{i+1}_{i}\boldsymbol{R}\ {}^{i}\boldsymbol{\omega}_{i} + \dot{\boldsymbol{\Theta}}_{i+1}\,{}^{i+1}\boldsymbol{z}_{i+1} & \text{(For rotational joint } i+1) \\ {}^{i+1}_{i}\boldsymbol{R}\ {}^{i}\boldsymbol{\omega}_{i} & \text{(For prismatic joint } i+1) \end{cases} \tag{4.6}$$

$$ {}^{i+1}\dot{\boldsymbol{\omega}}_{i+1} = \begin{cases} {}^{i+1}_{i}\boldsymbol{R}\ {}^{i}\dot{\boldsymbol{\omega}}_i + {}^{i+1}_{i}\boldsymbol{R}\ {}^{i}\boldsymbol{\omega}_i \times \dot{\boldsymbol{\Theta}}_{i+1}{}^{i+1}\boldsymbol{z}_{i+1} + \ddot{\boldsymbol{\Theta}}_{i+1}{}^{i+1}\boldsymbol{z}_{i+1} & \text{(Rotational joint)} \\ {}^{i+1}_{i}\boldsymbol{R}\ {}^{i}\dot{\boldsymbol{\omega}}_i & \text{(Prismatic joint)} \end{cases} \quad (4.7) $$

$$ {}^{i+1}\dot{\boldsymbol{v}}_{i+1} = \begin{cases} {}^{i+1}_{i}\boldsymbol{R}[\ {}^{i}\dot{\boldsymbol{v}}_i + {}^{i}\dot{\boldsymbol{\omega}}_i \times {}^{i}\boldsymbol{p}_{i+1} + {}^{i}\boldsymbol{\omega}_i \times (\ {}^{i}\boldsymbol{\omega}_i \times {}^{i}\boldsymbol{p}_{i+1})] \text{(Rotational joint)} \\ {}^{i+1}_{i}\boldsymbol{R}[\ {}^{i}\dot{\boldsymbol{v}}_i + {}^{i}\dot{\boldsymbol{\omega}}_i \times {}^{i}\boldsymbol{p}_{i+1} + {}^{i}\boldsymbol{\omega}_i \times (\ {}^{i}\boldsymbol{\omega}_i \times {}^{i}\boldsymbol{p}_{i+1})] \\ +2{}^{i+1}\boldsymbol{\omega}_{i+1} \times \dot{\boldsymbol{d}}_{i+1}{}^{i+1}\boldsymbol{z}_{i+1} + \ddot{\boldsymbol{d}}_{i+1}{}^{i+1}\boldsymbol{z}_{i+1} \text{ (Prismatic joint)} \end{cases} \quad (4.8) $$

$\boldsymbol{R}$ is the rotational matrix and ${}^{i}\boldsymbol{p}_{i+1}$ is the constant in frame {i}. $\dot{\boldsymbol{v}}$ is the linear velocity and $\dot{\boldsymbol{\omega}}$ is the angular velocity. The linear acceleration of the centre of mass of each link, which is shown as (Craig, 2005) $\boldsymbol{z}_{i+1}$ is the unit vector of coordinate axes *z* of joint *i+1*.

$$ {}^{i+1}\dot{\boldsymbol{v}}_{c_{i+1}} = {}^{i+1}\dot{\boldsymbol{v}}_{i+1} + {}^{i+1}\dot{\boldsymbol{\omega}}_{i+1} \times {}^{i+1}\boldsymbol{p}_{c_{i+1}} + {}^{i+1}\boldsymbol{\omega}_{i+1} \times ({}^{i+1}\boldsymbol{\omega}_{i+1} \times {}^{i+1}\boldsymbol{p}_{c_{i+1}}) \quad (4.9) $$

where $\{c_{i+1}\}$ is the centre of mass of each link.

Use Newton-Euler equations (4.1) and (4.2) to calculate the inertial force and torque effecting on the centre of mass of each link. Have equations as (Craig, 2005)

$$ {}^{i+1}\boldsymbol{F}_{c_{i+1}} = \boldsymbol{m}_{i+1}{}^{i+1}\dot{\boldsymbol{v}}_{c_{i+1}} \quad (4.10) $$

and

$$ {}^{i+1}\boldsymbol{\Gamma}_{c_{i+1}} = {}^{c_{i+1}}\boldsymbol{I}_{i+1}{}^{i+1}\dot{\boldsymbol{\omega}}_{i+1} + {}^{i+1}\dot{\boldsymbol{\omega}}_{i+1} \times ({}^{c_{i+1}}\boldsymbol{I}_{i+1}{}^{i+1}\boldsymbol{\omega}_{i+1}) \quad (4.11) $$

where $\boldsymbol{F}$ is the force acting at the centre of the mass and $\boldsymbol{\Gamma}$ is torque acting on the body to cause motion.

Inward iteration

We knew the force and torques acting on each link. Now we have to calculate the joint toques that are applied on each link. (Craig, 2005)

$$ {}^{i}\boldsymbol{F}_i = {}^{i}_{i+1}\boldsymbol{R}{}^{i+1}\boldsymbol{F}_{i+1} + {}^{i}\boldsymbol{F}_{c_i} \quad (4.12) $$

$$ {}^{i}\boldsymbol{n}_i = {}^{i}_{i+1}\boldsymbol{R}{}^{i+1}\boldsymbol{n}_{i+1} + {}^{i}\boldsymbol{n}_{c_i} + {}^{i}\boldsymbol{p}_{c_i} \times {}^{i}\boldsymbol{F}_{c_i} + {}^{i}\boldsymbol{p}_{i+1} \times {}^{i}_{i+1}\boldsymbol{R}{}^{i+1}\boldsymbol{F}_{i+1} \quad (4.13) $$

$$ \boldsymbol{\Gamma}_i = \begin{cases} {}^{i}\boldsymbol{n}_i^T\ {}^{i}\boldsymbol{z}_i & \text{For rotational joint} \\ {}^{i}\boldsymbol{F}_i^T\ {}^{i}\boldsymbol{z}_i & \text{For prismatic joint} \end{cases} \quad (4.14) $$

There are two sections to calculate the joint torques from the motion of the links. First, the Newton-Euler equations are applied on each link for computing link velocities and accelerations, from link 1 to link *n*. Second is the calculation of the force and torques, from link *n* to link 1.

4.1.3 Lagrangian method

The Newton-Euler method is based on the dynamic formulas (4.1) and (4.2). Lagrangian method is as an alternative to Newton-Euler. The difference between Newton-Euler approach and Lagrangian method is that Newton-Euler is identified as torque balance approach while Lagrangian method is identified as energy balance approach. To a mechanical system, the definition of Lagrange is the difference between system kinetic energy and system potential energy.

$$L(q,\dot{q}) = E_k(q,\dot{q}) - E_p(q) \tag{4.15}$$

where $q = [q_1, q_2, \dots, q_n]$ are the general positions, $\dot{q} = [\dot{q}_1, \dot{q}_2, \dots, \dot{q}_n]$ are related velocities.

The kinetic energy of the link *i* th is expressed as (Craig, 2005)

$$E_{ki} = \frac{1}{2} m_i v_{ci}^2 + \frac{1}{2} I_{ci} {\omega_i}^2 \tag{4.16}$$

In equation (4.16), the left section is kinetic energy according to linear velocity of the centre mass while the right section is the kinetic energy according to angular velocity of the link. The total kinetic energy is the sum of the kinetic energies of every link, as

$$E_k = E_{k1} + E_{k2} + \cdots + E_{kn} \tag{4.17}$$

In equation (4.16), v_{ci} and $\omega_i$are functions of joint position q and angular velocity

$\dot{q}$. Thus, the total kinetic energy can be described by a formula of the joint position and the joint velocity

As the total kinetic energy must be positive, the manipulator mass matrix is a positive definite matrix. Here, the quadratic form of every property in the positive definite matrix is a positive scalar. The familiar expression of the kinetic energy for a mass point is shown below

$$E_k = \frac{1}{2}mv^2 \tag{4.18}$$

The potential energy is (Craig, 2005)

$$E_p = -m_i g p_c \tag{4.19}$$

Here, g is acceleration vector of the gravity, p_c is the location vector of the *i* th link. The total potential energy is the sum of the potential energies of every link, as

$$E_p = E_{p1} + E_{p2} + \cdots + E_{pn} \tag{4.20}$$

As p_c in equation (4.19) are functions of q, so that potential energy also can be expressed by a scalar formula as a function shown as $E_p(q)$.

Lagrangian is originating the equation of motion from a scalar function. It is defined as the difference between the kinetic energy and potential energy. The Lagrangian is shown as

$$L(q, \dot{q}) = E_k(q, \dot{q}) - E_p(q) \tag{4.21}$$

Utilising the Lagrangian, get the dynamic equation

$$\frac{d}{dt}\frac{\partial L}{\partial \dot{\mathbf{\Theta}}} - \frac{\partial L}{\partial \mathbf{\Theta}} = \mathbf{\Gamma} \tag{4.22}$$

where $\mathbf{\Gamma}$ is a $n \times 1$ torque vector. Because there is no $\dot{q}$ in potential energy E_P, the dynamic equation becomes

$$\frac{d}{dt}\frac{\partial E_k}{\partial \dot{\boldsymbol{\Theta}}} - \frac{\partial E_k}{\partial \boldsymbol{\Theta}} + \frac{\partial E_p}{\partial \boldsymbol{\Theta}} = \boldsymbol{\Gamma} \tag{4.23}$$

4.2 Jacobians

The geometrical relationship between joint rates and velocity of the end-effector can be described in a matrix called the Jacobian. The research of velocities and forces leads to a matrix called the Jacobian. The Jacobian is a multidimensional form of the derivative. Suppose there are *n* functions. (Craig, 2005)

$$\begin{gathered} y_1 = f_1(x_1, x_2, \dots, x_n) \\ y_2 = f_2(x_1, x_2, \dots, x_n) \\ \vdots \\ y_n = f_n(x_1, x_2, \dots, x_n) \end{gathered} \tag{4.24}$$

Calculating the differentials of y_i consists of functions of differentials of x_j, we have

$$\begin{gathered} \delta y_1 = \frac{\partial f_1}{\partial x_1}\delta x_1 + \frac{\partial f_1}{\partial x_2}\delta x_2 + \cdots + \frac{\partial f_1}{\partial x_n}\delta x_n \\ \delta y_2 = \frac{\partial f_2}{\partial x_1}\delta x_1 + \frac{\partial f_2}{\partial x_2}\delta x_2 + \cdots + \frac{\partial f_2}{\partial x_n}\delta x_n \\ \vdots \\ \delta y_n = \frac{\partial f_n}{\partial x_1}\delta x_1 + \frac{\partial f_n}{\partial x_2}\delta x_2 + \cdots + \frac{\partial f_n}{\partial x_n}\delta x_n \end{gathered} \tag{4.25}$$

Later the equations in (4.25) can be written as vector.

$$\delta \boldsymbol{Y} = \frac{\partial \boldsymbol{F}}{\partial \boldsymbol{X}}\delta \boldsymbol{X} \tag{4.26}$$

The partial derivatives in (4.26) is the Jacobian. Use the notation,

$$\delta \boldsymbol{Y} = J(\boldsymbol{X})\delta \boldsymbol{X} \tag{4.27}$$

Dividing both sides of the equation (4.27) by differential time, we consider the Jacobian as velocities shown as,

$$\dot{\boldsymbol{Y}} = J(\boldsymbol{X})\dot{\boldsymbol{X}} \tag{4.28}$$

$\boldsymbol{X}$ has a value at any particular time, and $J(\boldsymbol{X})$ is a linear transformation. In another new time instant, the $\boldsymbol{X}$ may be changed and the linear transformation may change too.

4.3 Application to the fan blades

The fan blade is similar as the spherical pendulum that moves in a three-dimensional space. A new variable φ is introduced to describe the rotation of the fan blade around the *z*-axis. We can then define the position of the fan blade regarding the variables θ and φ. To describe this system with the new variable φ , use fan blade polar coordinates

$$X = l\sin\theta\cos\varphi \tag{4.29}$$

$$Y = l\sin\theta\cos\varphi \tag{4.30}$$

$$Z = l\cos\theta + z \tag{4.31}$$

where l is the length and z is the displacement of the fan blade on Z axis. The Lagrangian of the system is,

$$L = E_k - E_p \tag{4.32}$$

Consider the configuration, the *T* and *V* are the kinetic energies and potential energies of the system, respectively.

$$E_k = \frac{m}{2}(\dot{X}^2 + \dot{Y}^2 + \dot{Z}^2) \tag{4.33}$$

$$E_p = -mgZ \tag{4.34}$$

Differentiate X, Y, Z as velocities on three coordinates,

$$\dot{X} = \dot{\theta}l\cos\theta\cos\varphi - \dot{\varphi}l\sin\theta\sin\varphi \tag{4.35}$$

$$\dot{Y} = \dot{\theta}l\cos\theta\sin\varphi + \dot{\varphi}l\sin\theta\cos\varphi \tag{4.36}$$

$$\dot{Z} = -l\dot{\theta}\sin\theta + \dot{z} \tag{4.37}$$

Substitute (4.35), (4.36) and (4.37) into equations (4.33), (4.34), get

$$E_k = \frac{m}{2}\left(\dot{\theta}^2 l^2 + \dot{\varphi}^2 l^2 \sin^2\theta + \dot{z}^2 - 2\dot{z}l\dot{\theta}\sin\theta\right) \tag{4.38}$$

$$E_p = -mg(l\cos\theta + z) \tag{4.39}$$

Then, substitute (4.38) and (4.39) into (4.32), have Lagrangian of the fan blade is

$$L = \frac{m}{2}\left(\dot{\theta}^2 l^2 + \dot{\varphi}^2 l^2 \sin^2\theta + \dot{z}^2 - 2\dot{z}l\dot{\theta}\sin\theta\right) + mg(l\cos\theta + z) \tag{4.40}$$

The generalized equations of the movement regarding the energy of the system is described by the following expressions,

$$\frac{d}{dt}\frac{\partial L}{\partial \dot{\theta}} - \frac{\partial L}{\partial \theta} = M_\theta \tag{4.41}$$

$$\frac{d}{dt}\frac{\partial L}{\partial \dot{\varphi}} - \frac{\partial L}{\partial \varphi} = \mathrm{F}_\varphi \tag{4.42}$$

$$\frac{d}{dt}\frac{\partial L}{\partial \dot{z}} - \frac{\partial L}{\partial z} = \mathrm{F}_z \tag{4.43}$$

Differential θ and $\dot{\theta}$ for getting the $\ddot{\theta}$,

$$\frac{\partial L}{\partial \theta} = \dot{\varphi}^2 l^2 m \sin\theta\cos\theta - m\dot{z}l\dot{\theta}\cos\theta - mgl\sin\theta \tag{4.44}$$

$$\frac{\partial L}{\partial \dot{\theta}} = ml^2\dot{\theta} - m\dot{z}l\sin\theta \tag{4.45}$$

$$\frac{d}{dt}\frac{\partial L}{\partial \dot{\theta}} = ml^2\ddot{\theta} - m\ddot{z}l\sin\theta - m\dot{z}\dot{\theta}l\cos\theta \tag{4.46}$$

have the equation,

$$\frac{d}{dt}\frac{\partial L}{\partial \dot{\theta}} - \frac{\partial L}{\partial \theta} = M_\theta \tag{4.41}$$

Because there is a $\ddot{\theta}$ in equation (4.46), substitute (4.44), (4.45) and (4.41) into (4.46), get the expression of $\ddot{\theta}$,

$$\ddot{\theta} = \frac{\ddot{z}\sin\theta + \dot{\varphi}^2 l\sin\theta\cos\theta - g\sin\theta + M_\theta/ml}{l} \tag{4.47}$$

Using the same method to get the $\ddot{\varphi}$,

$$\frac{\partial L}{\partial \varphi} = 0 \tag{4.48}$$

$$\frac{\partial L}{\partial \dot{\varphi}} = m\dot{\varphi}l^2\sin^2\theta \tag{4.49}$$

$$\frac{d}{dt}\frac{\partial L}{\partial \dot{\varphi}} = m\ddot{\varphi}l^2\sin^2\theta + 2\dot{\theta}m\dot{\varphi}l^2\sin\theta\cos\theta \tag{4.50}$$

have equation,

$$\frac{d}{dt}\frac{\partial L}{\partial \dot{\varphi}} - \frac{\partial L}{\partial \varphi} = \mathrm{F}_\varphi \tag{4.42}$$

Because there is a $\ddot{\varphi}$ in equation (4.50), substitute (4.48), (4.49) and (4.42) into (4.50), get the expression of $\ddot{\varphi}$,

$$\ddot{\varphi} = \frac{\frac{\mathrm{F}_{\varphi}}{ml^2} - 2\dot{\theta}\dot{\varphi}\sin\theta\cos\theta}{\sin^2\theta} \tag{4.51}$$

Same method to get the $\ddot{z}$,

$$\frac{\partial L}{\partial z} = mg \tag{4.52}$$

$$\frac{\partial L}{\partial \dot{z}} = m\dot{z} - m\dot{\mathrm{\theta}}l\sin\theta \tag{4.53}$$

$$\frac{d}{dt}\frac{\partial L}{\partial \dot{z}} = m\ddot{z} - m\ddot{\theta}l\sin\theta - m\dot{\theta}^2 l\cos\theta \tag{4.54}$$

We have equation,

$$\frac{d}{dt}\frac{\partial L}{\partial \dot{z}} - \frac{\partial L}{\partial z} = \mathrm{F}_z \tag{4.43}$$

Because there is a $\ddot{\mathrm{z}}$ in equation (4.44), substitute (4.52), (4.53) and (4.43) into (4.44), get the expression of $\ddot{z}$,

$$\ddot{z} = \frac{\mathrm{F}_z}{m} + \ddot{\theta}l\sin\theta + \dot{\theta}^2 l\cos\theta + g \tag{4.55}$$

Gather all the equations, we have

$$\ddot{\theta} = \frac{\ddot{z}\sin\theta + \dot{\varphi}^2 l\sin\theta\cos\theta - g\sin\theta + M_\theta/ml}{l} \tag{4.56}$$

$$\ddot{\varphi} = \frac{\frac{\mathrm{F}_{\varphi}}{ml^2} - 2\dot{\theta}\dot{\varphi}\sin\theta\cos\theta}{\sin^2\theta} \tag{4.57}$$

$$\ddot{z} = \frac{\mathrm{F}_z}{m} + \ddot{\theta}l\sin\theta + \dot{\theta}^2 l\cos\theta + g \tag{4.58}$$

Consider $\ddot{\theta}, \ddot{\varphi}$ and $\ddot{z}$ as v_1, v_2 and v_3 which are auxiliary control,

$$\ddot{\theta} = \frac{\ddot{z}\sin\theta + \dot{\varphi}^2 l\sin\theta\cos\theta - g\sin\theta + M_\theta/ml}{l} \tag{4.59}$$

$$\ddot{\varphi} = \frac{\frac{\mathrm{F}_{\varphi}}{ml^2} - 2\dot{\theta}\dot{\varphi}\sin\theta\cos\theta}{\sin^2\theta} \tag{4.60}$$

$$\ddot{z} = \frac{\mathrm{F}_z}{m} + \ddot{\theta}l\sin\theta + \dot{\theta}^2 l\cos\theta + g \tag{4.61}$$

The error equation for the standard form is,

$$\ddot{\theta} = \ddot{\theta}_d - 2\zeta\omega_n\dot{e}_\theta - \omega_n^2 e_\theta \tag{4.62}$$

$$e_\theta = \theta - \theta_d \tag{4.63}$$

θ_d is the desired joint position, while denotes the real-time joint position, (4.63) equation describes the changing rule of deviation of the trajectory in certain system. It needs to ensure that $\theta_d \in (-\pi, \pi]$, each θ_d is processed before applying as input. θ is the real-time angle value, after substitution of θ_d and θ , have,

$$\ddot{\theta} - \ddot{\theta}_d + 2\zeta\omega_n\left(\dot{\theta}_d - \dot{\theta}\right) + \omega_n^2(\theta_d - \theta) = 0 \tag{4.64}$$

$$\ddot{\theta} = \ddot{\theta}_d + 2\zeta\omega_n\left(\dot{\theta}_d - \dot{\theta}\right) + \omega_n^2(\theta_d - \theta) \tag{4.65}$$

Substitute (4.65) into (4.59), yield,

$$\frac{\ddot{z}\sin\theta + \dot{\varphi}^2 l \sin\theta\cos\theta - g\sin\theta + M_\theta/ml}{l} = \ddot{\theta}_d + 2\zeta\omega_n\left(\dot{\theta}_d - \dot{\theta}\right) + \omega_n^2(\theta_d - \theta) \tag{4.66}$$

Simplify the equation (4.66) and get,

$$\begin{gathered} M_\theta = ml[\ddot{\theta}_d l + 2\zeta\omega_n l\left(\dot{\theta}_d - \dot{\theta}\right) + \omega_n^2 l(\theta_d - \theta) \\ -\ddot{z}\sin\theta - \dot{\varphi}^2 l \sin\theta\cos\theta + gsin\theta] \end{gathered} \tag{4.67}$$

Have M_θ as the control torque input to the motor. Equation (4.67) shows the control law of the fan blade.

In equations (4.60) and (4.61), set the control force F_φ and F_z to zero as there are no actuators to deliver these forces. For this reason, it is important to check if the zero dynamics

$$\ddot{\varphi}\sin^2\theta + 2\dot{\theta}\dot{\varphi}\sin\theta\cos\theta = 0 \tag{4.68}$$

and

$$\ddot{z} = \ddot{\theta} l \sin\theta + \dot{\theta}^2 l \cos\theta + g = 0 \tag{4.69}$$

is stable. In the design and construction, both φ and z are restrained and forced to remain stable.

4.4 Mathematical model of the fan blades

According to the design in Chapter 3, there are two fan devices in the dual-head fan retractor. Each end-effector of the fan devices consists of a palm and three blades. There are a master blade and two slave blades in a fan device. Now consider the palm as one link, and three blades as another three links shown in Figure 4.1. The mathematical model of the fan blades can be obtained by the Lagrangian method.

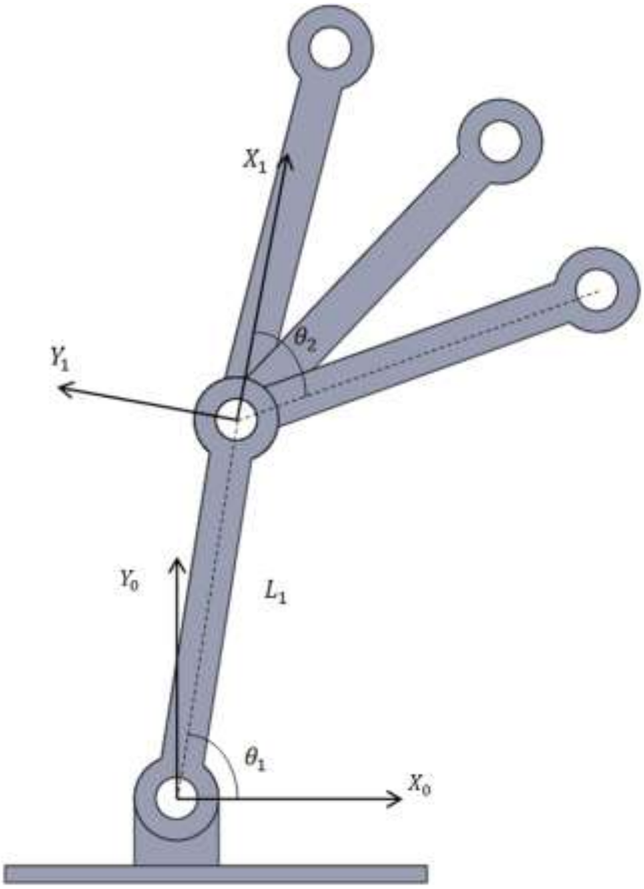

Figure 4.1: Four-link planar manipulator.

$$
\begin{gathered}
I_{11}\ddot{\theta}_1 + \sum_{k=2}^{4} I_{1k}\left(\ddot{\theta}_1 + \ddot{\theta}_k\right) \\
+ \sum_{k=2}^{4} (m_k l_{kcg} + M_k l_k) l_1 \sin\theta_k \left(\dot{\theta}_1^2 - (\dot{\theta}_1 + \dot{\theta}_k)^2\right) \\
+ g b_1 = \Gamma_1
\end{gathered}
\tag{4.70}
$$

$$
I_{k1}\ddot{\theta}_1 + I_{k2}\left(\ddot{\theta}_1 + \ddot{\theta}_2\right) + \left(m_k l_{kcg} + M_k l_k\right) L_1 \sin\theta_k \, \dot{\theta}_1^2 + g b_k = \Gamma_k \tag{4.71}
$$

where $k = 2,3,4$.

Here, m_i, l_i, l_{icg} and u_{icg} are the mass, length, the position of the centre gravity according to *i*-th joint and radius of gyration about the centre gravity of the *i* th link. M is the mass of intestine.

$$\begin{aligned} I_{11} = m_1\left(l_{1cg}^2 + u_{1cg}^2\right) + (m_2 + M_2)l_1^2 + \left(m_2 l_{2cg} + M_2 l_2\right)l_1 \cos\theta_2 \\ +\left(m_3 l_{3cg} + M_3 l_3\right)l_1 \cos\theta_3 + \left(m_4 l_{4cg} + M_4 l_4\right)l_1 \cos\theta_4 \end{aligned} \tag{4.72}$$

$$I_{1k} = m_k\left(l_{kcg}^2 + u_{kcg}^2\right) + M_k l_k^2 + \left(m_k l_{kcg} + M_k l_k\right)l_1 \cos\theta_k \tag{4.73}$$

$$I_{k1} = \left(m_k l_{kcg} + M_k l_k\right)l_1 \cos\theta_k \tag{4.74}$$

$$I_{k2} = m_k\left(l_{kcg}^2 + u_{kcg}^2\right) + M_k l_k^2 \tag{4.75}$$

where $k = 2,3,4$.

$$\begin{aligned} b_1 = (m_1 l_{1cg} + m_2 l_1 + m_3 l_1 + m_4 l_1 + M_2 l_1 + M_3 l_1 + M_4 l_1)\cos\theta_1 \\ +\left(m_2 l_{2cg} + M_2 l_{2cg}\right)\cos(\theta_1 + \theta_2) + \left(m_3 l_{3cg} + M_3 l_{3cg}\right)\cos(\theta_1 + \theta_3) \\ +\left(m_4 l_{4cg} + M_4 l_{4cg}\right)\cos(\theta_1 + \theta_4) \end{aligned} \tag{4.76}$$

$$b_k = \left(m_k l_{kcg} + M_k l_{kcg}\right)\cos(\theta_1 + \theta_k) \tag{4.77}$$

where $k = 2,3,4$.

Now, four links have been mathematically modelled. The control torques are established by the method outlined in the preceding section and similar to the equations (4.59) and (4.62).

4.5 Summary

The mathematical modelling of the tractor is described in this chapter. The dynamics of multi-body system is illustrated in three ways, the Newton-Euler approach, the recursive Newton-Euler formulation and Lagrangian methods. Next section introduces the Jacobians which is the relationship between the joint rate and velocity of the end-effector. Then, the fan blade is presented by considering the fan blade as a spherical pendulum. A new variable φ is introduced to describe the rotation of the fan blade around the z-axis. Later, the mathematical model of the fan end-effector is provided by using Lagrangian method. Each end-effector of the fan devices consists of a palm and three blades.

Chapter 5.

Modelling of active robotic manipulator for retractor applications

5.1 The 3-joint manipulator and its mathematical modelling

A 3-joint manipulator is mathematically modelled and controlled. First, the mechanical design of the 3-joint manipulator was created in SolidWorks. Second, the kinematic and dynamic equations were derived. Third, a computed torque PD controller was applied to dominate the rotational joints of the manipulator respectively. Fourth, the control based on the mathematical model was applied in a physical model created in SimMechanics. With the help of SimMechanics in MATLAB, the 3-joint manipulator can be controlled reasonably. Figure 5.1 shows the architecture of the 3-joint manipulator.

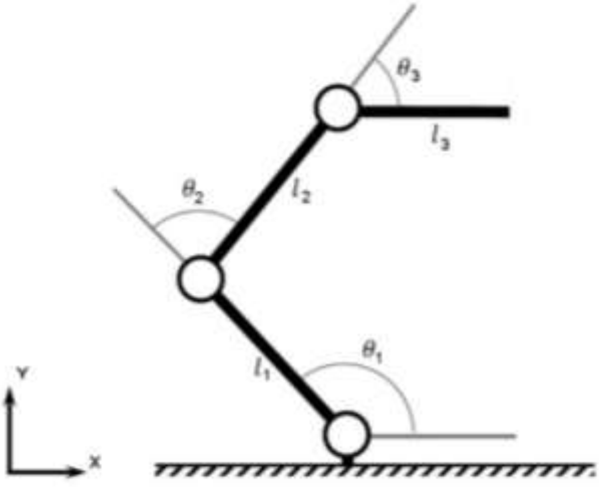

Figure 5.1: Architecture of the 3-joint manipulator.

Figure 5.2: Mechanical design in SolidWorks.

The mechanical design was created in SolidWorks as illustrated in Figure 5.2.

The 3-joint manipulator has three planar chains. The planar chains are connected with three rotational joints. The three rotational joints give three degrees of freedom. The 3-joint manipulator parameters shown below are link lengths, masses, inertia tensors, desired angles and gravitational acceleration. Here, link lengths of the three bars are l_1, l_2, l_3 ; the masses are m_1, m_2, m_3; the inertia tensors are shown below; the values of desired angles θ_d are shown below; and the gravitational acceleration is 9.8 m/s^2.

Table 5. 1: Parameters for the 3-joint manipulator

l_1	l_2	l_3	m_1	m_2	m_3
$1\ m$	$1\ m$	$1\ m$	$1\ kg$	$1\ kg$	$1\ kg$
I_1	I_2	I_3	θ_{d1}	θ_{d2}	θ_{d3}
$1\ kg \cdot m^2$	$1\ kg \cdot m^2$	$1\ kg \cdot m^2$	$0.1\ rad$	$0.2\ rad$	$0.4\ rad$

Figure 5.3 shows the manipulator with an end-effector. The joint 1 structure is known as the base structure which has coordinate x_1, y_1, z_1 and the subsequent structures are assigned by x_2, y_2, z_2, x_3, y_3, z_3 and ends by x_4, y_4, z_4.

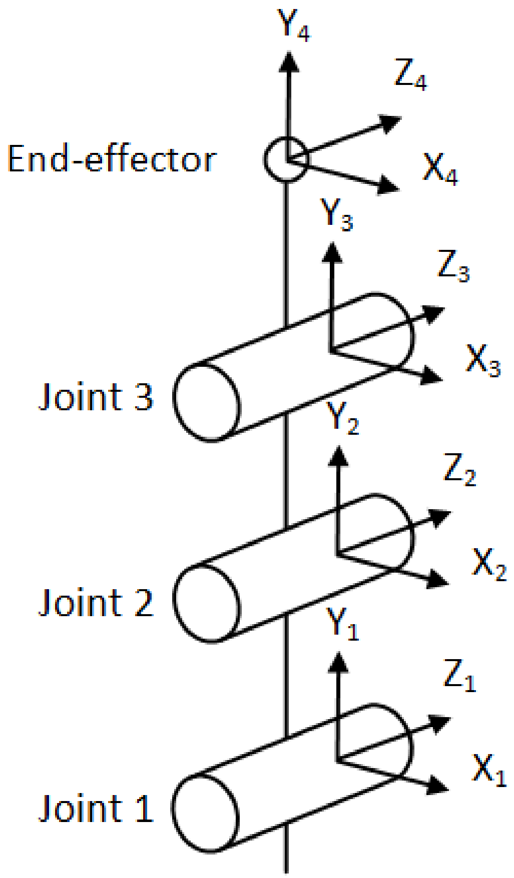

Figure 5.3: Model of the 3-joint manipulator.

The forward kinematic solution of the manipulator is assigned using Denavit-Hartenberg (DH) method (Denavit, 1955). The Denavit-Hartenberg parameters, also called DH parameters, illustrate each joint point. Four parameters associated with each joint point are shown in DH note. Here, the parameters of the 3-joint manipulator are presented in Table 5.2.

Table 5.2: Parameters of the 3-joint manipulator.

Link i	Angle θ_i	Link offset d_i	Link length a_{i-1}	Twist angle α_{i-1}
1	θ_1	0	l_1	0
2	θ_2	0	l_2	0
3	θ_3	0	l_3	0

The design of a robot manipulator controller is typically started by solving equations of its kinematics, dynamics, and feedback control. Both Newton-Euler and Lagrangian methods can be utilised to generate the dynamic equations. The dynamic equations are directed to the chain of links that are connected by rotational joints. Newton-Euler method considers static force in dynamics, by using velocities accelerations and torques to build the mathematic model, while Lagrangian formulation includes kinetic and potential energies and mainly focuses on energy. Here, the Lagrangian formulation has been chosen to develop the mathematical model. The objective of direct kinematics is to determine the position and orientation of the end-effector.

The position of the end-effector is,

$$\begin{aligned}
&\mathrm{X} = l_1 \cos\theta_1 + l_2 \cos(\theta_1+\theta_2) + l_3 \cos(\theta_1+\theta_2+\theta_3) \\
&\mathrm{Y} = l_1 \sin\theta_1 + l_2 \sin(\theta_1+\theta_2) + l_3 \sin(\theta_1+\theta_2+\theta_3) \\
&Z = 0
\end{aligned} \tag{5.1}$$

To model the 3-joint manipulator, the Lagrangian method is considered. In the generalized coordinate, Lagrangian formulation is defined by the difference between the kinetic energies and the potential energies as,

$$L = E_k - E_p \tag{5.2}$$

L is the Lagrangian, while E_k and E_p are the kinetic energies and potential energies of the system, respectively.

The generalized equations of the movement in terms of the energy of the system is described by the following expression,

$$\frac{d}{dt}\frac{\partial L}{\partial \dot{\boldsymbol{\Theta}}} - \frac{\partial L}{\partial \boldsymbol{\Theta}} = \boldsymbol{\Gamma} \tag{5.3}$$

where $\boldsymbol{\Gamma} \epsilon \mathbb{R}^{3\times1}$ means generalized forces, $\dot{\boldsymbol{\Theta}} \epsilon \mathbb{R}^{3\times1}$ is the joint velocities and $\boldsymbol{\Theta} \epsilon \mathbb{R}^{3\times1}$

denotes the joint positions.

Substitute (5.2) into (5.3) gets,

$$\frac{d}{dt}\frac{\partial L}{\partial \dot{\mathbf{\Theta}}} - \frac{\partial E_k}{\partial \mathbf{\Theta}} + \frac{\partial E_p}{\partial \mathbf{\Theta}} = \mathbf{\Gamma} \tag{5.4}$$

Since the input of the system is torque, the equation of the motion can be expressed as,

$$E_k = \frac{1}{2}I_1\dot{\theta}_1^2 + \frac{1}{2}I_2\dot{\theta}_2^2 + \frac{1}{2}I_3\dot{\theta}_3^2 + \frac{1}{2}m_1v_1^2 + \frac{1}{2}m_2v_2^2 + \frac{1}{2}m_3v_3^2 \tag{5.5}$$

where I is the moments of inertia, v is the linear velocity, m is the mass. Here, bars are well-distributed, so that the potential energy is expressed as,

$$\begin{gathered} E_p = \frac{1}{2}m_1gl_1 sin\theta_1 + m_2g\left[l_1 sin\theta_1 m_1 + \frac{1}{2}l_2\sin(\theta_1+\theta_2)\right] \\ +m_3g[l_1 sin\theta_1 + l_2\sin(\theta_1+\theta_2) + \frac{1}{2}l_3\sin(\theta_1+\theta_2+\theta_3)] \end{gathered} \tag{5.6}$$

Substituting (5.62) and (5.63) into (5.61), the dynamics can be shown as,

$$\mathbf{\Gamma} = \mathbf{H}(\theta)\ddot{\mathbf{\Theta}} + \mathbf{C}(\theta,\dot{\theta}) + \mathbf{G}(\theta) \tag{5.7}$$

$$\mathbf{\Gamma} = \mathbf{H}(\theta)\begin{bmatrix}\ddot{\theta}_1\\ \ddot{\theta}_2\\ \ddot{\theta}_3\end{bmatrix} + \mathbf{\Phi}(\theta)\begin{bmatrix}\dot{\theta}_1\\ \dot{\theta}_2\\ \dot{\theta}_3\end{bmatrix} + \mathbf{\Psi}(\theta)\begin{bmatrix}\dot{\theta}_1\dot{\theta}_2\\ \dot{\theta}_1\dot{\theta}_3\\ \dot{\theta}_2\dot{\theta}_3\end{bmatrix} + \mathbf{G}(\theta)\begin{bmatrix}cos\,\theta\\ cos(\theta_1+\theta_2)\\ cos(\theta_1+\theta_2+\theta_3)\end{bmatrix} \tag{5.8}$$

$\ddot{\mathbf{\Theta}}\epsilon\mathbb{R}^{3\times1}$ is the joint accelerations, $\mathbf{H}\epsilon\mathbb{R}^{3\times3}$ is the inertia matrix where the analysis of the manipulator is performed, $\mathbf{C}\epsilon\mathbb{R}^{3\times3}$ which is known as a matrix denoting Coriolis and centrifugal forces , $\mathbf{G}\epsilon\mathbb{R}^{3\times3}$ is a vector of gravitational forces. $\mathbf{C}(\theta,\dot{\theta})$ consists of two non-linear terms,

$$\mathbf{C}(\theta,\dot{\theta}) = \mathbf{\Phi}(\theta)\begin{bmatrix}\dot{\theta}_1\\ \dot{\theta}_2\\ \dot{\theta}_3\end{bmatrix} + \mathbf{\Psi}(\theta)\begin{bmatrix}\dot{\theta}_1\dot{\theta}_2\\ \dot{\theta}_1\dot{\theta}_3\\ \dot{\theta}_2\dot{\theta}_3\end{bmatrix} \tag{5.9}$$

Equation (5.66) is a linear time-invariant differential equation which describes the robot dynamics. The equations below present the values of **H**, **C**, and **G**.

$$\left.\begin{aligned} H_{11} &= 2m_1l_1^2 + (m_2+m_3)\left(l_1^2+l_2^2+2l_1l_2\cos\theta_2\right) + m_3l_3^2 + 2m_3l_1l_3\cos(\theta_2+\theta_3) + 2m_3l_2l_3 \\ H_{12} &= (m_2+m_3)l_2^2 + m_3l_3^2 + l_1l_2\left(m_2+m_3\cos\theta_2\right) + l_1l_3m_3\cos(\theta_2+\theta_3) + l_2l_3m_3\cos\theta_3 \\ H_{13} &= m_3^2l_3^2 + l_1l_3m_3\cos(\theta_2+\theta_3) + l_2l_3m_3\cos\theta_3 \\ H_{21} &= (m_2+m_3)l_2^2 + m_3l_2^2 + l_1l_2m_2 + l_1l_2m_3\cos\theta_2 + l_1l_3m_3\cos(\theta_2+\theta_3) + 2m_3l_2l_3\cos\theta_3 \end{aligned}\right\}$$

$$\left.\begin{aligned}
H_{22} &= 2m_2 l_2^2 + m_3\left(l_2^2 + l_3^2\right) + 2m_3 l_2 l_3 \cos\theta_3 \\
H_{23} &= -m_2 l_2 l_3 \sin\theta_3 \\
H_{31} &= m_3 l_3^2 + m_3 l_1 l_3 \cos\left(\theta_2 + \theta_3\right) + m_3 l_2 l_3 \\
H_{32} &= m_3 l_3^2 + m_3 l_2 l_3 \cos\theta_3 \\
H_{33} &= 2m_3 l_3^2
\end{aligned}\right\} \tag{5.10}$$

$$\left.\begin{aligned}
\Phi_{11} &= \Phi_{21} = \Phi_{22} = 0 \\
\Phi_{12} &= -m_3 l_1 l_2 \sin\theta_2 - m_3 l_1 l_3 \sin(\theta_2 + \theta_3) \\
\Phi_{13} &= -m_3 l_1 l_3 \sin(\theta_2 + \theta_3) - m_3 l_2 l_3 \sin\theta_3 \\
\Phi_{31} &= m_3 l_3^2 + m_3 l_1 l_3 \cos(\theta_2 + \theta_3) + m_3 l_2 l_3 \\
\Phi_{32} &= m_3 l_3^2 + m_3 l_2 l_3 \cos\theta_3 \\
\Phi_{33} &= 2m_3 l_3^2
\end{aligned}\right\} \tag{5.11}$$

$$\left.\begin{aligned}
\Psi_{11} &= -2(m_2 + m_3) l_1 l_2 \sin\theta_2 - 2m_3 l_1 l_3 \sin(\theta_2 + \theta_3) \\
\Psi_{12} &= -2m_3 l_1 l_3 \sin(\theta_2 + \theta_3) \\
\Psi_{13} &= -2m_3 l_1 l_3 \sin(\theta_2 + \theta_3) - 2m_3 l_2 l_3 \sin\theta_3 \\
\Psi_{23} &= -m_3 l_2 l_3 \sin\theta_3 \\
\Psi_{31} &= -m_3 l_1 l_2 \sin\theta_2 - m_3 l_1 l_3 \sin(\theta_2 + \theta_3) \\
\Psi_{32} &= -m_3 l_1 l_3 \sin(\theta_2 + \theta_3) - 2m_3 l_2 l_3 \sin\theta_3
\end{aligned}\right\} \tag{5.12}$$

$$\left.\begin{aligned}
\mathrm{G}_{11} &= g l_1\left(\frac{m_1}{2} + m_2 + m_3\right) \\
\mathrm{G}_{12} &= g l_2\left(\frac{m_2}{2} + m_3\right) \\
\mathrm{G}_{13} &= g m_3 \frac{l_3}{2} \\
\mathrm{G}_{21} &= \mathrm{G}_{31} = \mathrm{G}_{32} = 0 \\
\mathrm{G}_{22} &= m_2 g \frac{l_2}{2} + m_3 g l_2 \\
\mathrm{G}_{23} &= m_3 g \frac{l_3}{2} \\
\mathrm{G}_{33} &= m_3 g \frac{l_3}{2}
\end{aligned}\right\} \tag{5.13}$$

5.2 Control development of the 3-joint manipulator

In this section, the feasibility of controlling the 3-joint manipulator will be demonstrated using a general feedback control. The actual synthesis of the control law will be discussed in chapter 6.

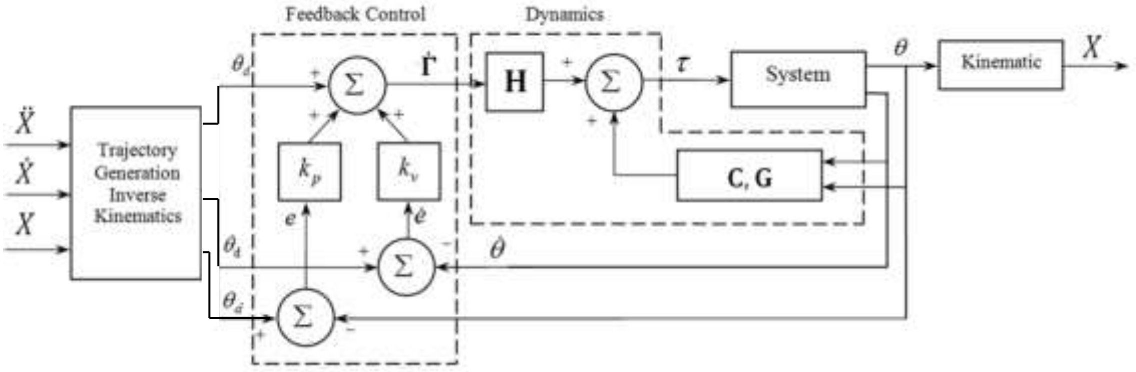

Figure 5.4: Block diagram of the controller of the 3-joint manipulator.(Hamdi-Cherif, 2011)

A multivariable control scheme for the model of the 3-joint manipulator is developed, which additionally, contains an inner loop controller (Kelly, 1994). The multivariable PD controller which utilised by the inner loop aims to stabilise the manipulator by placing the closed-loop poles at the desired value of angle. In the 3-joint manipulator, a PD feedback control law is applied to each joint, independently. The control system separates the controller into two parts, dynamic section and feedback control section. The dynamic equation is expressed as below,

$$\mathbf{\Gamma} = \mathbf{H}(\theta)\ddot{\mathbf{\Theta}} + \mathbf{C}(\theta, \dot{\theta}) + \mathbf{G}(\theta) \tag{5.14}$$

Computed torque control is utilised in this thesis. Joint torque $\mathbf{\Gamma}$ is divided into two parts,

$$\boldsymbol{\Gamma} = \boldsymbol{\alpha}\dot{\boldsymbol{\Gamma}} + \boldsymbol{\beta} \tag{5.15}$$

Where $\boldsymbol{\alpha}$ and $\boldsymbol{\beta}$ are undetermined matrixes. The rule to choose $\boldsymbol{\alpha}$ and $\boldsymbol{\beta}$ is to determine $\dot{\mathbf{\Gamma}}$ as a new input. Combining (5.14) and (5.15), the total system can be expressed as,

$$\mathbf{H}(\theta)\ddot{\mathbf{\Theta}} + \mathbf{C}(\theta, \dot{\theta}) + \mathbf{G}(\theta) = \boldsymbol{\alpha}\dot{\mathbf{\Gamma}} + \boldsymbol{\beta} \tag{5.16}$$

where,

$$\begin{cases} \boldsymbol{\alpha} = \mathbf{H} \\ \boldsymbol{\beta} = \mathbf{C} + \mathbf{G} \end{cases} \tag{5.17}$$

Substituting (5.73) into (5.74) give joint torque as,

$$\dot{\mathbf{\Gamma}} = \ddot{\mathbf{\Theta}} \tag{5.18}$$

which is the system equation. Furthermore, consider (5.18) as open-loop equation of motivation system. Since the control type is PD feedback control, so that assume control laws are,

$$\ddot{\theta}_i = -k_{pi}\theta_i - k_{vi}\dot{\theta}_i \ (i = 1{,}2 \text{ and } 3) \tag{5.19}$$

Apply (5.18) into (5.19) gives second order linear dynamics as below,

$$k_{pi}\theta_i + k_{vi}\dot{\theta}_i + \ddot{\theta}_i = 0 \tag{5.20}$$

In the equation (5.20), k_{pi} and k_{vi} are the control gains, while θ_i is the angle value. Use e_i to present the difference which gives,

$$e_i = \theta_{di} - \theta_i \tag{5.21}$$

$$k_{pi}e_i + k_{vi}\dot{e}_i + \ddot{e}_i = 0 \tag{5.22}$$

θ_{di} is the desired joint position, while θ denotes the real-time joint position, (5.22) equation describes the changing rule of deviation of the trajectory in the system. It needs to ensure that $\theta_{di} \in (-\pi, \pi]$, each θ_{di} is processed before applying as input. After substitution of θ_{di} and θ_i,

$$k_{pi}(\theta_{di} - \theta_i) + k_{vi}\left(\dot{\theta}_{di} - \dot{\theta}_i\right) + \ddot{\theta}_{di} - \ddot{\theta}_i \tag{5.23}$$

$$\ddot{\theta} = k_{pi}(\theta_{di} - \theta_i) + k_{vi}\left(\dot{\theta}_{di} - \dot{\theta}_i\right) + \ddot{\theta}_{di} \tag{5.24}$$

As we already get the $\mathbf{H}(\theta)$, $\mathbf{C}\left(\theta, \dot{\theta}\right)$ and $\mathbf{G}(\theta)$ from (5.10) to (5.13), obtain the joint torque of the motor,

$$\mathbf{\Gamma} = \mathbf{H}(\theta)\begin{bmatrix} k_{p1}(\theta_{d1} - \theta_1) + k_{v1}\left(\dot{\theta}_{d1} - \dot{\theta}_1\right) + \ddot{\theta}_{d1} \\ k_{p2}(\theta_{d2} - \theta_2) + k_{v2}\left(\dot{\theta}_{d2} - \dot{\theta}_2\right) + \ddot{\theta}_{d2} \\ k_{p3}(\theta_{d3} - \theta_3) + k_{v3}\left(\dot{\theta}_{d3} - \dot{\theta}_3\right) + \ddot{\theta}_{d3} \end{bmatrix} + \mathbf{C}\left(\theta, \dot{\theta}\right) + \mathbf{G}(\theta) \tag{5.25}$$

5.3 Results and discussion

The flow chart in Figure 5.5 shows the method used for the determination of the mathematical model. First, derivation of the mathematical model is indicated; second, simulation of the derived mathematical model as the manipulator is affected by gravitation; third, development of chasing control algorithm is carried out; fourth, the control law is simulated.

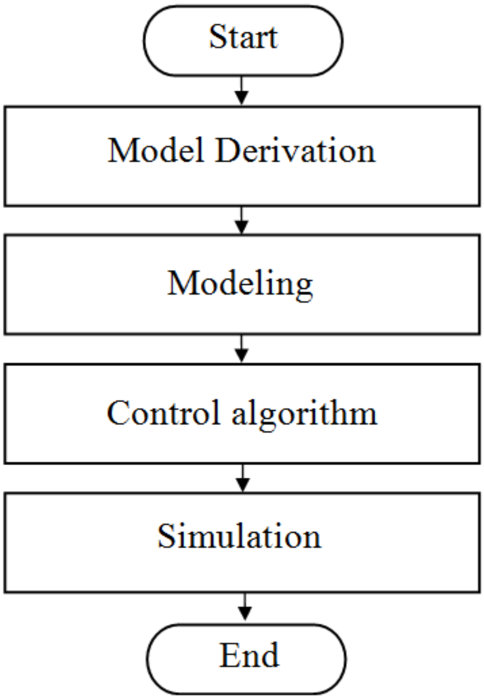

Figure 5.5: Flowchart illustrating the methodology.

A remarkable efficient mathematical function can help with self-contained figure processing, user-friendly interface and feature-rich deployment kit. For creating the mathematical function, MATLAB is chosen to simulate modelling and control algorithms. With the help of Simulink tools in MATLAB, development of the virtual simulation of the system becomes realisable. The simulation diagram is shown in Figure 5.6.

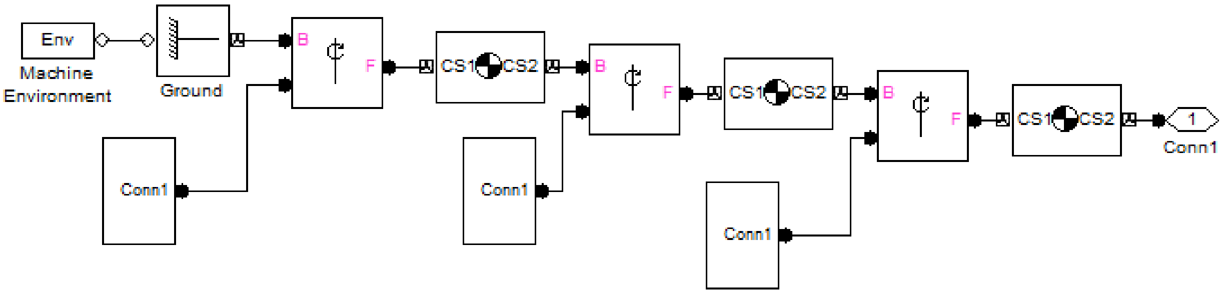

Figure 5.6: Simulation diagram made by Simulink in MATLAB.

The statement and solution of the orientation control problem depend on the following provisions:

- Divide the **Γ** into module control and servo control. The PD control separates controller into two parts. One is feedback controlled, and another is dynamically controlled.
- Find a function in which the θ (angle value) tends to θ_d (desired angle value) by using an optimal PD control law; other adaptive control laws such as PID or Fuzzy servo control may also be used.

The objective of the section is to examine the consequences of the proposed model. Several simulations have been used to estimate the capability of predicting the 3-joint manipulator movements through the proposed model. Figure 5.7 and Figure 5.8 give the animation on how the bars moved in SimMechanics and SolidWorks separately. Control Gains are found as $k_{vi} = 16, k_{pi} = 64$ (i = 1,2 and 3).

The parabola of θ_{id} is determined as,

$$\theta_{id} = (\text{desired\_value\_}i) \cdot (1 - \mathrm{e}^{-t/0.3}) \tag{5.26}$$

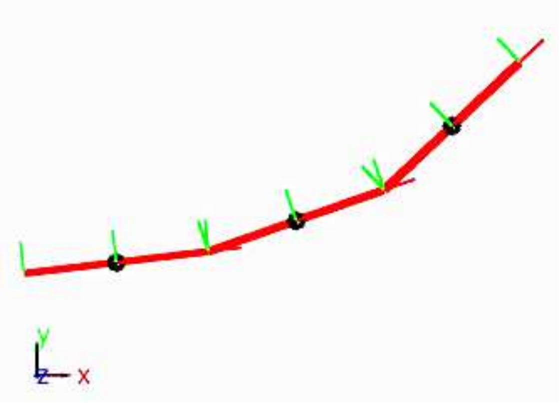

Figure 5.7: Model of 3-joint manipulator in SimMechanics.

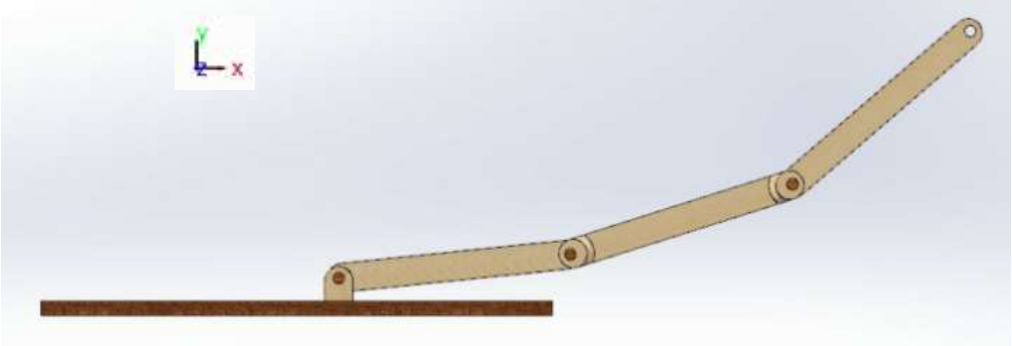

Figure 5.8: Model of 3-joint manipulator in SolidWorks.

As can be seen in Figure 5.9, the trajectories of the desired joint angles and the current joint angles match pretty well. Apparently, the output joint angles positions closely follow the desired command in some case. The usage of computed torques control proved to be effective in those cases in purpose for achieving the position tracking of joint angles. The results have shown that the system is well built and stable.

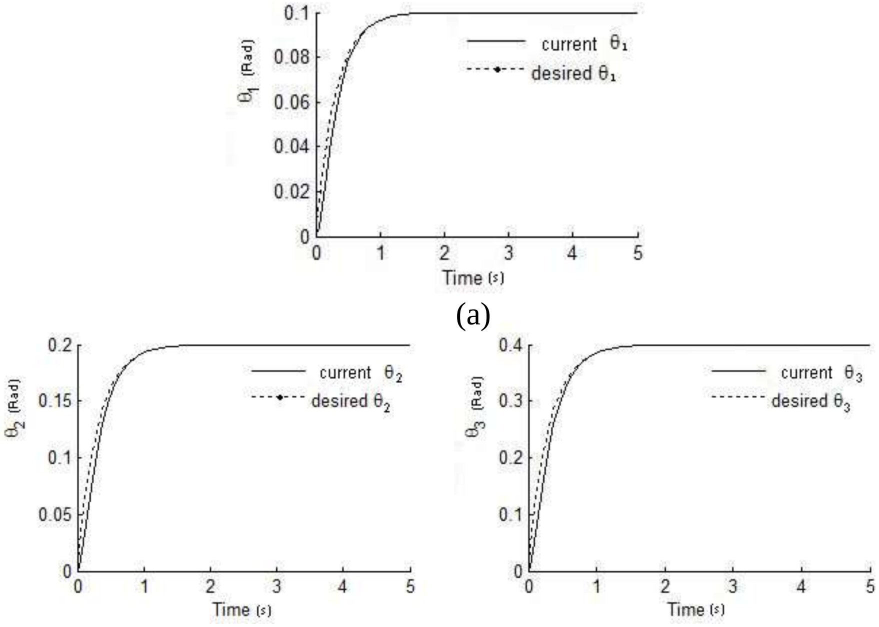

(a)

(b) (c)

Figure 5.9: Position tracking of (a) joint 1, (b) joint 2 and (c) joint 3.

In Figures 5.10 and 5.11, results of joint tracking velocities and torques are shown respectively. The joint angle velocities decreased to zero and remain stable, and the torques become stable on certain values too. It takes approximate two second to reach the right position.

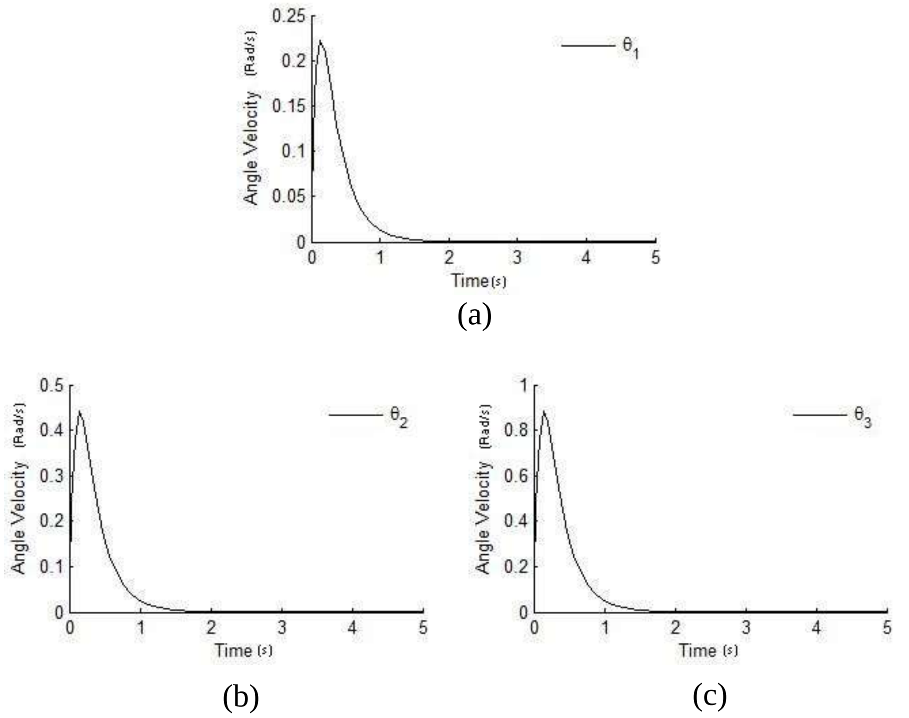

(a)

(b) (c)

Figure 5.10: Velocity results of (a) joint 1, (b) joint 2 and (c) joint 3.

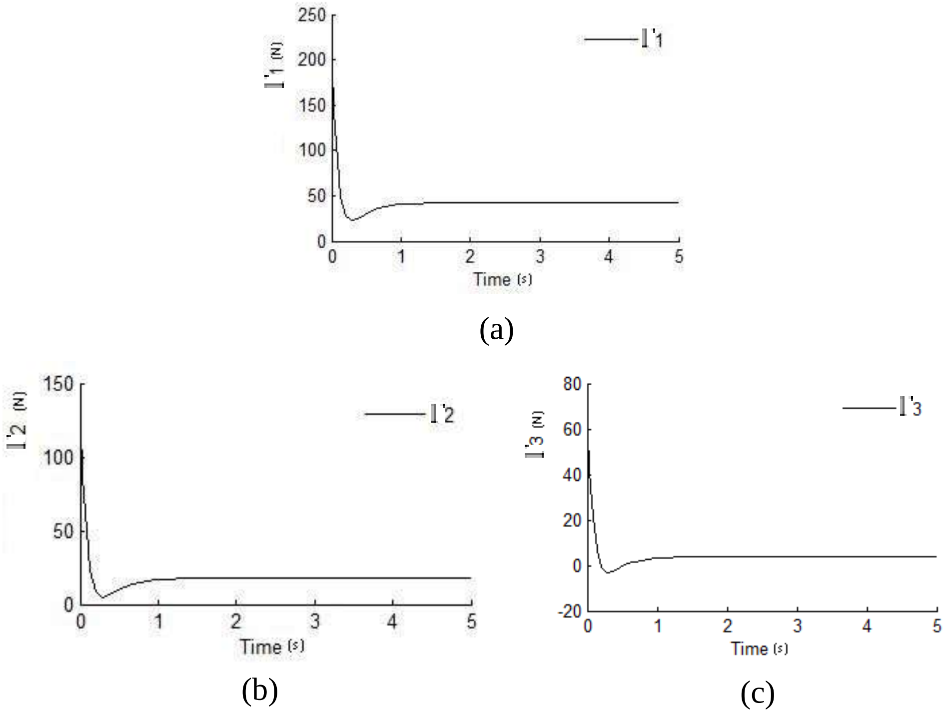

(a)

(b) (c)

Figure 5.11: Joint torque results of (a) joint 1, (b) joint 2and (c) joint 3.

In conclusion, the dynamic model of a 3-joint manipulator has been developed using Lagrangian approach. The control response of the manipulator obtained using computed torque based on PD control approach is satisfactory regarding both speed and accuracy. The trajectory of the desired joint angle and the actual response angle matches closely.

It can be said that the output of the joint position follows the desired joint position.

The usage of computed torque control proved to be effective to achieve the position tracking. Current torque turns out to be smooth and appropriate value, which is good for the whole system. The result shows that the system is stable and efficient. The model is then showed in SolidWorks and SimMechanics, which can intuitively present the movement and trajectory. From the user interface of SimMechanics, development of trajectory and gesture of the manipulator can be made through further analysis and test. Advanced control methods will be investigated to control the system for addressing nonlinearity and other model uncertainties in the future.

5.4 Lagrange equations of the robotic retractor

Previously, a 3-joint manipulator is modelled and controlled. In this section, the retractor modelled and controlled by a 2-joint manipulator is simulated. In the 2-joint manipulator, one joint is a prismatic joint, and another is a rotational joint. The manipulator’s end effector is assumed to be in contact with a soft wall. The Lagrangian formulation is utilised to simulate the mathematical model.

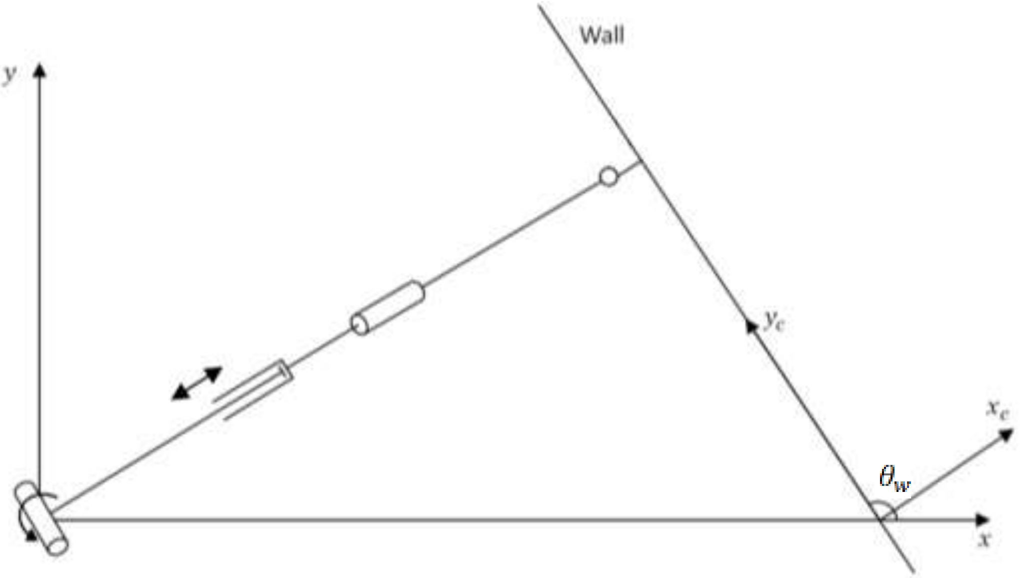

Figure 5.12: Diagram of the 2-joint manipulator with the dual-hand fan retractor.

Assume that the inertia tensor of bars and retractor are

$$I_1 = I_2 = 1\ kg \cdot m^2$$

The kinetic energy equations of the manipulator are,

$$E_{k1} = \frac{1}{2}m_1 l_1^2 \dot{\theta}_1^2 + \frac{1}{2}I_1 \dot{\theta}_1^2 \tag{5.27}$$

$$E_{k2} = \frac{1}{2}m_2\left(l_2^2\dot{\theta}_1^2 + \dot{l}_2^2\right) + \frac{1}{2}I_2\dot{\theta}_1^2 \tag{5.28}$$

The sum kinetic energy is,

$$E_k(q,\dot{q}) = \frac{1}{2}(m_1 l_1^2 + I_1 + I_2 + m_2 l_2^2)\dot{\theta}_1^2 + \frac{1}{2}m_2\dot{l}_2^2 \tag{5.29}$$

The potential energy equations of the manipulator are,

$$E_{p1} = m_1 l_1 s_1 g$$

$$E_{p2} = m_2 l_2 s_1 g$$

The sum potential energy is,

$$E_p(q) = g(m_1 l_1 + m_2 l_2)s_1 \tag{5.30}$$

Get,

$$\frac{\partial E_k}{\partial \dot{\boldsymbol{\Theta}}} = \begin{bmatrix} (m_1 l_1^2 + I_1 + I_2 + m_2 l_2^2)\dot{\theta}_1 \\ m_2 \dot{l}_2 \end{bmatrix} \tag{5.31}$$

$$\frac{\partial E_k}{\partial \boldsymbol{\Theta}} = \begin{bmatrix} 0 \\ m_2 l_2 \dot{\theta}_1^2 \end{bmatrix} \tag{5.32}$$

$$\frac{\partial E_p}{\partial \boldsymbol{\Theta}} = \begin{bmatrix} g(m_1 l_1 + m_2 l_2)c_1 \\ m_2 g s_1 \end{bmatrix} \tag{5.33}$$

Substitute into Euler-Lagrange equation,

$$\boldsymbol{\Gamma} = \frac{d}{dt}\frac{\partial E_k}{\partial \dot{\boldsymbol{\Theta}}} - \frac{\partial E_k}{\partial \boldsymbol{\Theta}} + \frac{\partial E_p}{\partial \boldsymbol{\Theta}} \tag{5.34}$$

Get,

$$\Gamma_1 = (m_1 l_1^2 + I_1 + I_2 + m_2 l_2^2)\ddot{\theta}_1 + 2m_2 l_2 \dot{\theta}_1 \dot{l}_2 + g c_1 (m_1 l_1 + m_2 l_2)\ , \tag{5.35}$$

$$\Gamma_2 = m_2 \ddot{l}_2 - m_2 l_2 \dot{\theta}_1^2 + m_2 g s_1 \tag{5.36}$$

Γ_1 is rotational joint torques, while Γ_2 is prismatic joint force. $c_1$is $\cos\theta_1$, and $s_1$is $\sin\theta_1$. Then, get the dynamic equation,

$$\mathbf{H} = \begin{bmatrix} m_1 l_1^2 + I_1 + I_2 + m_2 l_2^2 & 0 \\ 0 & m_2 \end{bmatrix} \tag{5.37}$$

$$\mathbf{C}(\theta, \dot{\theta}) = \begin{bmatrix} 2m_2 l_2 \dot{\theta}_1 \dot{l}_2 \\ -m_2 l_2 \dot{\theta}_1^2 \end{bmatrix} \tag{5.38}$$

$$\mathbf{G}(\theta) = \begin{bmatrix} g c_1 (m_1 l_1 + m_2 l_2) \\ m_2 g s_1 \end{bmatrix} \tag{5.39}$$

H describes the links' inertia, $\mathbf{C}(\theta, \dot{\theta})$ is the vector of the Coriolis and centrifugal torques, and $\mathbf{G}(q)$ is the vector of the gravitational torques.

Get,

$$\ddot{\theta}_1 = \frac{\Gamma_1 - 2m_2 l_2 \dot{\theta}_1 \dot{l}_2 - g c_1 (m_1 l_1 + m_2 l_2)}{m_1 l_1^2 + I_1 + I_2 + m_2 l_2^2} \tag{5.40}$$

$$\ddot{l}_2 = \frac{\Gamma_2 + m_2 l_2 \dot{\theta}_1^2 - m_2 g s_1}{m_2} \tag{5.41}$$

The error equation for the standard form is,

$$\ddot{\theta}_1 = \ddot{\theta}_{1d} - 2\zeta_1 \omega_{1n} \dot{e}_\theta - \omega_{1n}^2 e_\theta \tag{5.42}$$

$$e_{\theta_1} = \theta_1 - \theta_{1d} \tag{5.43}$$

θ_{1d} is the desired joint angle for θ_1. θ_1 is the real-time angle value, after substitution of θ_{1d} and θ_1 ,

$$\ddot{\theta}_1 - \ddot{\theta}_{1d} + 2\zeta_1 \omega_{1n}(\dot{\theta}_{1d} - \dot{\theta}_1) + \omega_{1n}^2(\theta_{1d} - \theta_1) = 0 \tag{5.44}$$

Substitute (5.99) into (5.95), get,

$$\frac{\Gamma_1 - 2m_2 l_2 \dot{\theta}_1 \dot{l}_2 - g c_1 (m_1 l_1 + m_2 l_2)}{m_1 l_1^2 + I_1 + I_2 + m_2 l_2^2} = \ddot{\theta}_{1d} + 2\zeta_1 \omega_{1n}(\dot{\theta}_{1d} - \dot{\theta}_1) + \omega_{1n}^2(\theta_{1d} - \theta_1) \tag{5.45}$$

Simplify (5.100) get Γ_1,

$$\begin{gathered}\Gamma_1 = \left[\ddot{\theta}_{1d} + 2\zeta_1\omega_{1n}\left(\dot{\theta}_{1d} - \dot{\theta}_1\right) + \omega_{1n}^2(\theta_{1d} - \theta_1)\right] \cdot (m_1 l_1^2 + I_1 + I_2 + m_2 l_2^2) \\ +2m_2 l_2 \dot{\theta}_1 \dot{l}_2 + g c_1(m_1 l_1 + m_2 l_2)\end{gathered} \tag{5.46}$$

Here, $\zeta_1 = 1$ so that the result is critically damped.

The error equation for the standard form is,

$$\ddot{l}_2 = \ddot{l}_{2d} - 2\zeta_2\omega_{2n}\dot{e}_\theta - \omega_{1n}^2 e_\theta \tag{5.47}$$

$$e_{l_2} = l_2 - l_{2d} \tag{5.48}$$

l_{2d} is the desired prismatic joint position for chain two. l_2 is the real-time translating value, after substitution of l_{2d} and l_2.

$$\ddot{l}_2 - \ddot{l}_{2d} + 2\zeta_2\omega_{2n}\left(\dot{l}_{2d} - \dot{l}_2\right) + \omega_{2n}^2(l_{2d} - l_2) = 0 \tag{5.49}$$

Substitute (5.104) into (5.96), get,

$$\frac{\Gamma_2 + m_2 l_2 \dot{\theta}_1^2 - m_2 g s_1}{m_2} = \ddot{l}_{2d} - 2\zeta_2\omega_{2n}\dot{e}_\theta - \omega_{1n}^2 e_\theta \tag{5.50}$$

Simplify (5.105) get Γ_2,

$$\begin{gathered}\Gamma_2 = \left[\ddot{l}_{2d} + 2\zeta_2\omega_{2n}\left(\dot{l}_{2d} - \dot{l}_2\right) + \omega_{2n}^2(l_{2d} - l_2)\right] \cdot m_2 \\ -m_2 l_2 \dot{\theta}_1^2 + m_2 g s_1\end{gathered} \tag{5.51}$$

Here, $\zeta_2 = 1$ so that the result is critically damped.

5.5 Euler-Lagrange equations for the robotic retractor with additional degree of freedom

In the preceding chapter, a 2-joint manipulator is mathematically modelled and controlled. Different from the 2-joint manipulator, a 3-joint manipulator, which has two rotational joints and a prismatic joint, is mathematically modelled in this section. The reason for considering this 3-joint manipulator is to assess the benefits of introducing an additional rotational joint in the design of the retractor manipulator. In particular, including an additional rotational joint seems to improve the available workspace and operational gesture.

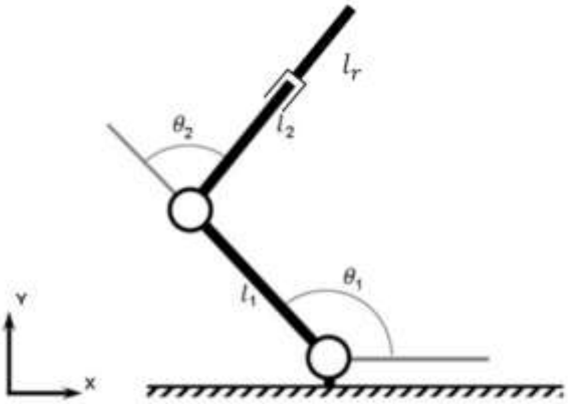

Figure 5. 13: Architecture of retractor manipulator.

Here, the length of the bar-1 and bar-2 are l_1, l_2 while the length between retractor mass point and the end of joint-2 is l_r. Rotational joints are θ_1 and θ_2 separately. The masses of bar-1, bar-2 and retractor are m_1, m_2 and m_r. Two rotational joints give two degrees of freedom, and one prismatic joint gives one degree of freedom.

Assume that the inertia tensor of bars and retractor are

$$I_1 = I_2 = I_3 = 1\ kg \cdot m^2$$

The kinetic energy of the manipulator and the retractor are,

$$E_{k1} = \frac{1}{2} m_1 l_1^2 \dot{\theta}_1^2 + \frac{1}{2} I_1 \dot{\theta}_1^2 \tag{5.52}$$

$$E_{k2} = \frac{1}{2} m_2 l_2^2 \dot{\theta}_2^2 + \frac{1}{2} I_2 \dot{\theta}_2^2 + \frac{1}{2} I_2 \dot{\theta}_1^2 \tag{5.53}$$

$$E_{k3} = \frac{1}{2} m_3 \left(l_3^2 \dot{\theta}_2^2 + \dot{l}_3^2 \right) + \frac{1}{2} I_3 (\dot{\theta}_1^2 + \dot{\theta}_2^2) \tag{5.54}$$

The sum kinetic energy is,

$$E_k(\mathrm{q}, \dot{\mathrm{q}}) = \frac{1}{2}(m_1 l_1^2 + I_1 + I_2 + I_3)\dot{\theta}_1^2 + \frac{1}{2}(m_2 l_2^2 + I_2 + m_3 l_3^2 + I_3)\dot{\theta}_2^2 + \frac{1}{2} m_3 \dot{l}_3^2 \tag{5.55}$$

The potential energy of the manipulator and the retractor are,

$$E_{p1} = m_1 l_1 s_1 g \tag{5.56}$$

$$E_{p2} = m_2 l_1 g s_1 + m_2 l_3 g s_2 \tag{5.57}$$

The sum potential energy is,

$$E_p(q) = g(m_1 l_1 s_1 + m_2 l_1 s_1 + m_2 l_3 s_2) \tag{5.58}$$

Get,

$$\frac{\partial E_k}{\partial \dot{\mathbf{\Theta}}} = \begin{bmatrix} (m_1 l_1^2 + I_1 + I_2 + I_3)\dot{\theta}_1 \\ (m_2 l_2^2 + I_2 + I_3 + m_3 l_3^2)\dot{\theta}_2 \\ m_3 \dot{l}_3 \end{bmatrix} \tag{5.59}$$

$$\frac{\partial E_k}{\partial \mathbf{\Theta}} = \begin{bmatrix} 0 \\ 0 \\ m_3 l_3 \dot{\theta}_2^2 \end{bmatrix} \tag{5.60}$$

$$\frac{\partial E_p}{\partial \mathbf{\Theta}} = \begin{bmatrix} g(m_1 l_1 + m_2 l_2) c_1 \\ g m_2 l_3 c_2 \\ m_2 g s_2 \end{bmatrix} \tag{5.61}$$

Substitute into Euler-Lagrange equation,

$$\mathbf{\Gamma} = \frac{d}{dt}\frac{\partial E_k}{\partial \dot{\mathbf{\Theta}}} - \frac{\partial E_k}{\partial \mathbf{\Theta}} + \frac{\partial E_p}{\partial \mathbf{\Theta}} \tag{5.62}$$

Get,

$$\Gamma_1 = (m_1 l_1^2 + I_1 + I_2 + I_3)\ddot{\theta}_1 + g c_1 (m_1 l_1 + m_2 l_2) \tag{5.63}$$

$$\Gamma_2 = (m_2 l_2^2 + I_2 + I_3 + m_3 l_3^2)\ddot{\theta}_2 + 2 m_3 l_3 \dot{\theta}_2 \dot{l}_3 + g m_2 l_3 c_2 \tag{5.64}$$

$$\Gamma_3 = m_3 \ddot{l}_3 - m_3 l_3 \dot{\theta}_2^2 + m_2 g s_2 \tag{5.65}$$

Γ_1 and Γ_2 are rotational joint torques, while $\mathit{\Gamma}_3$ is prismatic joint force. Then, get the dynamic equation,

$$\mathbf{H}(\theta) = \begin{bmatrix} m_1 l_1^2 + I_1 + I_2 + I_3 & 0 & 0 \\ 0 & m_2 l_2^2 + I_2 + I_3 + m_3 l_3^2 & 0 \\ 0 & 0 & m_3 \end{bmatrix} \tag{5.66}$$

$$\mathbf{C}(\theta, \dot{\theta}) = \begin{bmatrix} 0 \\ 2 m_3 l_3 \dot{\theta}_2 \dot{l}_3 \\ -m_3 l_3 \dot{\theta}_2^2 \end{bmatrix} \tag{5.67}$$

$$\mathbf{G}(\theta) = \begin{bmatrix} g c_1 (m_1 l_1 + m_2 l_2) \\ g m_2 l_3 c_2 \\ m_2 g s_2 \end{bmatrix} \tag{5.68}$$

5.6 Summary

To sum up, the 3-joint manipulator, which has three rotational joints, and its mathematical model has been illustrated. Later the control methods and results of the 3-joint manipulator are shown using PD computed control. It is important to implement the 3-joint manipulator first because the robotic manipulators for the retractor has one (or two) rotational joint(s) and one prismatic joint. Model and control of the 3-joint manipulator scrape up experience for better control of the robotic manipulator. The reason why we need a prismatic joint is because the prismatic joint can help push or pull intestine or organ in one direction which is convenient than operating rotational joints. Later, the Lagrange equations of the robotic retractors are designated. The first manipulator is a 2-joint manipulator with one prismatic joint and one rotational joint. The second manipulator is a 3-joint manipulator with one prismatic joint and two rotational joints. The reason why implementing the second manipulator is that the 2-joint manipulator has the limitation of operating different position and orientation while the 3-joint manipulator has more working space and gestures than the 2-joint manipulator.

Chapter 6.

Control law synthesis for active compliance control

The interaction between robot and environment position and force control methods are classified into two parts: passive compliance and active compliance. Passive compliance applies mechanisms like spring and damper to store energy. Active compliance relies on impedance control and hybrid position/force control. In this chapter, the active compliance is investigated.

6.1 Impedance control and its appropriateness

Impedance control was raised by Hogan (Hogan 1984). The control concept is one of the basic robot elasticity control algorithms, and it is popular when using in manipulators control. The impedance control basic on a manipulator impedance parameter which makes force and position related in a dynamic relationship. Impedance control mainly considers the relationship between environment and the end-effector. The manipulating period contains multiple mechanical power translation. In some circumstance the external force can be ignored so that the manipulator typically regards as an isolated system. This is so called position control. However, manipulator cannot be considered as an isolated system.

Impedance control method considering target impedance force or position instead of real robot dynamic model. When there is error between the end-effector real-time position $\boldsymbol{X}$ and ideal trajectory $\boldsymbol{X}_{\mathbf{d}}$, which is

$$\mathbf{e} = \boldsymbol{X}_{\mathbf{d}} - \boldsymbol{X} \tag{6.1}$$

Because of the error, the robot end-effector gets the relative F_{imp} impedance force from the contact object. The relationship has shown below,

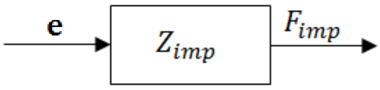

Figure 6.1: Diagram of the impedance control.

$$\mathbf{F}_{imp} = \mathbf{M}\ddot{\mathbf{e}} + \mathbf{B}\dot{\mathbf{e}} + \mathbf{K}\mathbf{e} \tag{6.2}$$

Here, **M, B, K** are the impedance parameters of the robot manipulator, $\boldsymbol{Z}_{imp}$ is the impedance of the manipulator. The definition Hogan gave was one system must compensate another. If one system is impedance controlled, then, the other must have admittance characteristic. That means, once there is an error in the impedance control system so that an impedance force generates. To say in another way, when the system has impedance force, then a certain error will occur.

To almost all the control assessment, the environment includes stiffness and dynamic constraint condition. Admittance characteristic generates when input force affects the other object, and the outside environment has only admittance characteristic instead of impedance force. When the outside environment gains acting force, displacement generates.

$$\boldsymbol{X} = \frac{\mathbf{F_{imp}}}{\mathbf{H}} \tag{6.3}$$

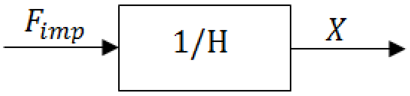

Figure 6.2: Diagram of the admittance force to displacement.

When the robot manipulator is contacting the outer space, robot impedance control strategy is shown below,

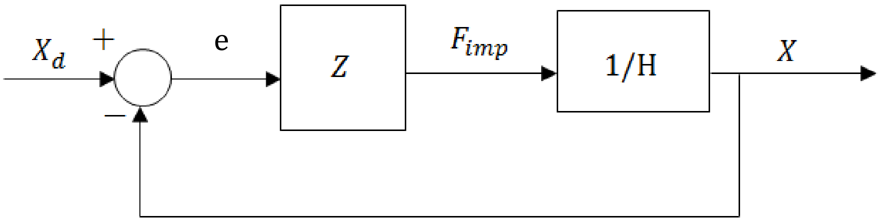

Figure 6.3: Diagram of impedance control of a robot.

Same as the dynamic equation in this report,

$$\mathbf{H}(q)\ddot{\mathbf{\Theta}} + \mathbf{C}(q,\dot{q}) + \mathbf{G}(q) = \mathbf{\Gamma} \tag{6.4}$$

When the robot is contacting with the outer space, the end-effector force is F_e, Γ is the joint force, get the equation as

$$\mathbf{H}(q)\ddot{\mathbf{\Theta}} + \mathbf{C}(q,\dot{q}) + \mathbf{G}(q) = \mathbf{\Gamma} - \mathbf{F_e} \tag{6.5}$$

Variable Structure Control (VSC) scheme was first applied by Young (1978). The theoretical studies (Morgan and Özgüner, 1985; Slotine and Sastry, 1983) and practical implementations (Hashimoto et al., 1987; Hiroi et al., 1986; Klein & Maney, 1979) both verified its feasibility, robustness and low computational expense. VSC is extensively utilised in impedance control (Chan et al., 1991). In impedance VSC, links of the manipulator are induced to match their first order linear decoupled law. Chen and Xiao (2011) noted the development and implementation of a robotic system using variable structure impedance control algorithm.

According to Chen & Xiao's algorithm,

$$\mathbf{M}(X)\ddot{X} + \mathbf{B}(X,\dot{X}) + \mathbf{K}(X) = \mathbf{F} \tag{6.6}$$

$$\mathbf{H}(q)\ddot{q} + \mathbf{C}(q,\dot{q}) + \mathbf{G}(q) = \mathbf{\Gamma} \tag{6.7}$$

$$\mathbf{\Gamma} = \boldsymbol{J}^T(q)\mathbf{F} \tag{6.8}$$

Where,

$$\mathbf{M}(X) = \boldsymbol{J}^{-T}(q)\mathbf{H}(q)\boldsymbol{J}^{-1}(q) \tag{6.9}$$

$$\mathbf{B}(X,\dot{X}) = \boldsymbol{J}^{-T}(q)\mathbf{C}(q,\dot{q})\boldsymbol{J}^{-1}(q) - \boldsymbol{J}^{-T}(q)\mathbf{H}(q)\boldsymbol{J}^{-1}(q)\dot{\boldsymbol{J}}(q)\boldsymbol{J}^{-1}(q) \tag{6.10}$$

$$\mathbf{K}(X) = \boldsymbol{J}^{-T}(q)\mathbf{G}(q) \tag{6.11}$$

The impedance is turned out as a second-order function connect the motion error and the interaction force error,

$$\mathbf{M}_m\ddot{\mathbf{e}} + \mathbf{B}_m\dot{\mathbf{e}} + \mathbf{K}_m\mathbf{e} = -\mathbf{K}_f\mathbf{e}_f \tag{6.12}$$

where $\mathbf{e}$ is the tracking error and $\mathbf{e}_f$ is the interaction force error.

$$\mathbf{e} = \boldsymbol{X}(t) - \boldsymbol{X}_d(t), \quad \mathbf{e}_f = \mathbf{F}(t) - \mathbf{F}_d(t) \tag{6.13}$$

Where $\mathbf{M}_m, \mathbf{B}_m, \mathbf{K}_m$ are the desired inertia, damping, and stiffness. $\boldsymbol{X}_d(t)$ is the desired motion trajectory and $\mathbf{F}_d(t)$ is the desired contact force. $\boldsymbol{X}(t)$ is the modified trajectory and $\mathbf{F}(t)$ is the interaction force. Normally, $\mathbf{M}_m, \mathbf{B}_m, \mathbf{K}_m, \mathbf{K}_f$ are considered as definite diagonal matrices to gain decoupled response.

A dynamic compensator in terms of variable structure model reaching control (VSMRC) method has been provided to solve the impedance control problem,

$$\dot{\mathbf{z}} = \mathbf{A}\mathbf{z} + \mathbf{K}_{pz}\mathbf{e} + \mathbf{K}_{vz}\dot{\mathbf{e}} + \mathbf{K}_{fz}\mathbf{e}_f \tag{6.14}$$

Where $\mathbf{z}$ is the n-dimensional state vector of the compensator, $\mathbf{A}$ is any semi-negative definite matrix, and $\mathbf{K}_{pz}, \mathbf{K}_{vz}, \mathbf{K}_{fz}$ are specified to shape the dynamic sliding mode constant matrices for achieving desired impedance. The compensator is employed in forming the switching function,

$$\mathbf{s}(\mathbf{e}, \dot{\mathbf{e}}, \mathbf{z}) = \dot{\mathbf{e}} + \mathbf{F_1 e} + \mathbf{F_2 z} \tag{6.15}$$

Where $\mathbf{F}_1$ is constant matrices and $\mathbf{F}_2$ is any non-singular matrix. Differentiation of (6.15) is

$$\dot{\mathbf{s}} = \ddot{\mathbf{e}} + \mathbf{F_1}\dot{\mathbf{e}} + \mathbf{F_2}\dot{\mathbf{z}}$$

The resultant sliding mode $\{\mathbf{s} = \mathbf{0}, \dot{\mathbf{s}} = \mathbf{0}\}$ is described by

$$\begin{gathered} \mathbf{z} = -\mathbf{F_2^{-1}}(\dot{\mathbf{e}} + \mathbf{F_1 e} - \mathbf{s}) \\ \dot{\mathbf{z}} = -\mathbf{F_2^{-1}}(\ddot{\mathbf{e}} + \mathbf{F_1}\dot{\mathbf{e}} - \dot{\mathbf{s}}) \end{gathered} \tag{6.16}$$

Substituting (6.14) into (6.16), we can get

$$\ddot{\mathbf{e}} + \left(\mathbf{F_1} - \mathbf{F_2 A F_2^{-1}} + \mathbf{F_2 K_{vz}}\right)\dot{\mathbf{e}} + \left(\mathbf{F_2 K_{pz}} - \mathbf{F_2 A F_2^{-1} F_1}\right)\mathbf{e} = -\mathbf{F_2 K_{fz} e_f} \tag{6.17}$$

as the sliding mode equation.

Comparing (6.17) with (6.12), get

$$\begin{gathered} \mathbf{K_{vz}} = \mathbf{F_2^{-1}}\left(\mathbf{M_m^{-1} B_m} - \mathbf{F_1} + \mathbf{F_2 A F_2^{-1}}\right) \\ \mathbf{K_{pz}} = \mathbf{F_2^{-1}}\left(\mathbf{M_m^{-1} K_m} + \mathbf{F_2 A F_2^{-1} F_1}\right) \\ \mathbf{K_{fz}} = \mathbf{F_2^{-1} M_m^{-1} K_f} \end{gathered} \tag{6.18}$$

both left and right terms multiple M_m. (6.17) will be described as,

$$\mathbf{M_m}\ddot{\mathbf{e}} + \mathbf{B_m}\dot{\mathbf{e}} + \mathbf{K_m e} = -\mathbf{K_f e_f} + \mathbf{M_m}\left(\dot{\mathbf{s}} - \mathbf{F_2 A F_2^{-1} s}\right) \tag{6.19}$$

When $\mathbf{s} = \mathbf{0}$ and $\dot{\mathbf{s}} = \mathbf{0}$ during sliding motion, equation (6.19) is identical to the generalized impedance equation (6.12). The VSC impedance control law indicates that the robot reaches the sliding mode in finite time.

6.2 Hybrid position/force control

Hybrid position/force control is another control scheme in active compliance control. Hybrid position/force control of a robotic system is critical for practical manipulation tasks like grinding, cutting, drilling, insertion, joining, contour following, debarring, scribing, drawing, sweeping and certain related tasks. Craig (1979) reported the concept in hybrid position/force control at the first time. This concept allows robots to utilise different joints to control force and position separately. That means control force in force control algorithm adjusts the position by using the rest orthogonality. Later in 1981, Raibert and Craig noted a new method based on Masons (1981) concept, using Jacobian matrix to figure out working areas direction force and position.

In this chapter, two algorithms of hybrid position/force control will be modelled and compared. One is from Khatib, and another is from Azenha. The models are based on a 2-joint manipulator that both two joints are rotational joints show in Figure 6.4. In the next section, the objective is comparing the result of discovering a better control for the manipulator control of the robotic retractor.

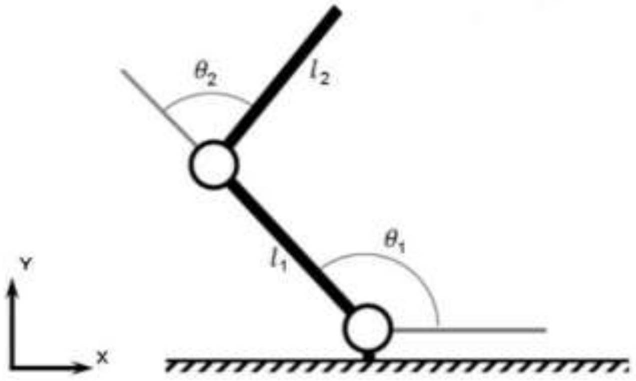

Figure 6.4: 2-joint manipulator.

6.2.1 Hybrid position/force control method from Khatib and Burdick

Depend on Khatib & Burdick's report (Khatib and Burdick, 1987), the end-effector dynamic equations in operational space are,

$$\mathbf{M}(X)\ddot{\boldsymbol{X}} + \mathbf{B}\big(X, \dot{X}\big) + \mathbf{K}(X) = \mathbf{F} \tag{6.19}$$

where $\mathbf{M}(X)$ represents the kinetic energy matrix, and $\mathbf{B}\big(X, \dot{X}\big)$ represent the vector of end-effector centrifugal and Coriolis forces. $\mathbf{K}(X)$ designates the gravity, while F generalized operational force vectors in the robot end-effector.

The manipulator equations in joint space are,

$$\mathbf{H}(q)\ddot{q} + \mathbf{C}(q, \dot{q}) + \mathbf{G}(q) = \boldsymbol{\Gamma} \tag{6.20}$$

where q is the $n \times 1$ joint displacement vector, $\mathbf{H}(\theta)$ is the $n \times n$ joint space inertia matrix, $\mathbf{C}\big(\theta, \dot{\theta}\big), \mathbf{G}(\theta)$ represent the Coriolis and centrifugal vector and gravity vector in joint space. **Γ** describes the generalized torque in joint space.

The relationship between **F** and the joint forces **Γ** is,

$$\boldsymbol{\Gamma} = \boldsymbol{J}^{T}(\theta)\mathbf{F} \tag{6.21}$$

$$\dot{\boldsymbol{X}} = \boldsymbol{J}(\theta)\dot{\boldsymbol{\Theta}} \tag{6.22}$$

$$\ddot{\boldsymbol{X}} = \boldsymbol{J}(\theta)\ddot{\boldsymbol{\Theta}} + \dot{\boldsymbol{J}}(\theta)\dot{\boldsymbol{\Theta}} \tag{6.23}$$

have,

$$\mathbf{M}(X) = \boldsymbol{J}^{-T}(\theta)\mathbf{H}(\theta)\boldsymbol{J}^{-1}(\theta) \tag{6.24}$$

In operational space, the manipulator is relying on the F as a command vector. The move of a manipulator end-effector is based on the inertial coupling, centrifugal, and Coriolis forces. In operational space, the nonlinear dynamic decoupling and motion control for the manipulator end-effector is,

$$\mathbf{F} = \mathbf{F_m} + \mathbf{F_{ccg}} \tag{6.25}$$

where $\mathbf{F_m}, \mathbf{F_{ccg}}$ are the operational command vectors of motion, centrifugal and Coriolis.

$$\mathbf{F_m} = \mathbf{M}(X)\mathbf{F}^*_\mathbf{m} \tag{6.26}$$

$$\mathbf{F_{ccg}} = \mathbf{B}\left(X, \dot{X}\right) + \mathbf{K}(X)\ , \tag{6.27}$$

Consider $\mathbf{h}(\theta, \dot{\theta})$ as,

$$\mathbf{h}\left(\theta, \dot{\theta}\right) = \dot{\boldsymbol{J}}(\theta)\dot{\boldsymbol{\Theta}}\ . \tag{6.28}$$

Using equation (6.21), the joint forces corresponding to the operational command vector **F** in (6.25) can be written as,

$$\boldsymbol{\Gamma} = \boldsymbol{J}^T(\theta)\mathbf{M}(\theta)\mathbf{F}^*_\mathbf{m} + \mathbf{C}\left(\theta, \dot{\theta}\right) + \mathbf{G}(\theta) \tag{6.29}$$

According to Khatib & Burdick's algorithm, get

$$\boldsymbol{\Gamma} = \boldsymbol{J}^T(\theta)\mathbf{M}(\theta)\mathbf{F}^*_\mathbf{m} + \mathbf{C}\left(\theta, \dot{\theta}\right) - \boldsymbol{J}^T(\theta)\mathbf{M}(\theta)\mathbf{h}\left(\theta, \dot{\theta}\right) + \mathbf{G}(\theta) \tag{6.30}$$

The operational command vector for end-effector motion, including in addition the active force control in equation (6.25) is given by,

$$\mathbf{F} = \mathbf{F_m} + \mathbf{F_a} + \mathbf{F_{ccg}} \tag{6.31}$$

where $\mathbf{F_m}, \mathbf{F_a}, \mathbf{F_{ccg}}$ are the operational command vectors of motion, active force control, and centrifugal, Coriolis, and gravity forces written as,

$$\mathbf{F_m} = \mathbf{M}(\theta)\boldsymbol{\Omega}\mathbf{F}^*_\mathbf{m} \tag{6.32}$$

$$\mathbf{F_a} = \widetilde{\boldsymbol{\Omega}}\mathbf{F}^*_\mathbf{a} + \mathbf{M}(\theta)\widetilde{\boldsymbol{\Omega}}\mathbf{F}^*_\mathbf{a} \tag{6.33}$$

$$\mathbf{F_{ccg}} = \mathbf{C}\left(\theta, \dot{\theta}\right) - \boldsymbol{J}^T(\theta)\mathbf{M}(\theta)\mathbf{h}\left(\theta, \dot{\theta}\right) + \mathbf{G}(\theta). \tag{6.34}$$

where $\mathbf{F}^*_\mathbf{a}$ represents the vector of end-effector velocity damping that acts in the direction of force control. Here $\boldsymbol{\Omega}$ is matrix defines the generalized position and force. The control architecture is illustrated in Figure 6.4.

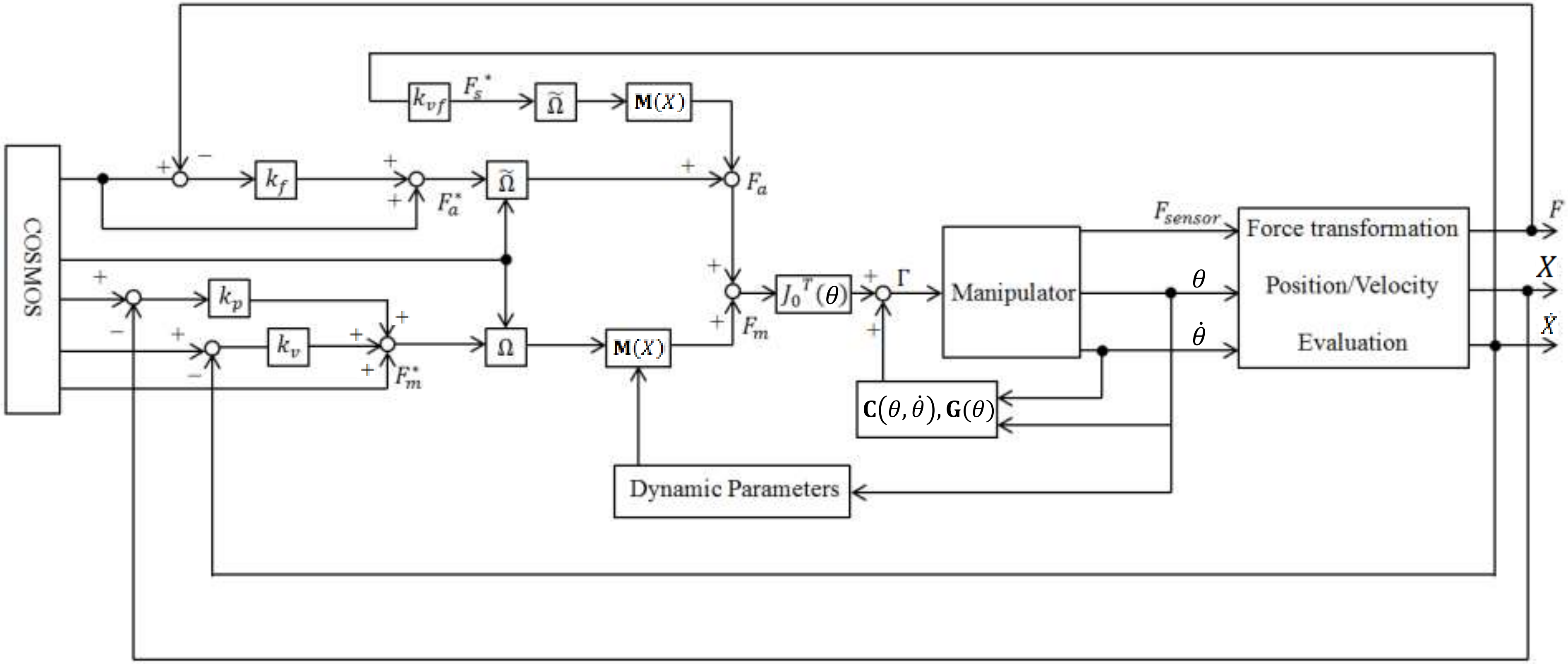

Figure 6.5: Operational space control architecture of Khatib and Burdick's algorithm.

6.2.2 Hybrid position/force control from Azenha and Machado

The diagonal matrix S is the $n\times n$ selection matrix with elements equal to *1/0* in the position/force controlled directions during the experiments, we consider the Cartesian y_c/x_c coordinate to be position/force controlled, below is the Azenha & Machado's method (Azenha and Machado, 1997)

$$\mathbf{\Omega} = \begin{bmatrix} s_{11} & 0 \\ 0 & s_{22} \end{bmatrix} \tag{6.35}$$

$$\boldsymbol{J}_c(q) = \begin{bmatrix} -r_1\, cos(\theta_w-\theta_1) - r_2\, cos(\theta_w-\theta_1-\theta_2) & -r_2\, cos(\theta_w-\theta_1-\theta_2) \\ r_1\, sin(\theta_w-\theta_1) + r_2\, sin(\theta_w-\theta_1-\theta_2) & r_2\, sin(\theta_w-\theta_1-\theta_2) \end{bmatrix} \tag{6.36}$$

$\boldsymbol{J}_c(q)$ is the manipulator Jacobin matrix,

$$\boldsymbol{J}_c(q) = \frac{\partial f(q)}{\partial \mathbf{\Theta}} \tag{6.37}$$

Where x is the position and orientation vector of the end-effector frame.

$$f(q){:}\begin{cases} x_c = r_1\, sin(\theta_w-\theta_1) + r_2\, sin(\theta_w-\theta_1-\theta_2) \\ y_c = r_1\, cos(\theta_w-\theta_1) + r_2\, cos(\theta_w-\theta_1-\theta_2) \end{cases} \tag{6.38}$$

θ_w is the angle of the wall. Real-time calculation of J_c^{-1} may cause limitation in singular points. For overcoming this problem, pseudo-inverse is proposed to be the solution. That means, block $J_c^{-1}S$ is substituted by $(SJ_c)^+$ while the symbol + means the pseudo-inverse of the matrix. Dr Fisher proved the sufficient stability condition (Fisher and Mujtaba, 1992).

As SJ_c is singular, $(SJ_c)^+$ is calculated through the singular value decomposition mode. Therefore, we have $s_{11}=0, s_{22}=1$,

$$\mathbf{\Omega}\boldsymbol{J}_c = \begin{bmatrix} 0 & 0 \\ a & b \end{bmatrix}, \tag{6.39}$$

$$\begin{cases} a = r_1\, sin(\theta_w-\theta_1) + r_2\, sin(\theta_w-\theta_1-\theta_2) \\ b = r_2\, sin(\theta_w-\theta_1-\theta_2) \end{cases}, \tag{6.40}$$

$$(\mathbf{\Omega}\boldsymbol{J}_c)^+ = (\mathbf{\Omega}\boldsymbol{J}_c)^T \cdot (\mathbf{\Omega}\boldsymbol{J}_c \cdot (\mathbf{\Omega}\boldsymbol{J}_c)^T)^{-1}, \tag{6.41}$$

$$(\boldsymbol{\Omega J}_c)^+ = \begin{bmatrix} 0 & a \\ 0 & b \end{bmatrix} \cdot \frac{1}{a^2 + b^2}. \tag{6.42}$$

To transform from a position controlled to a force controlled system, it is fulfilled by changing the s_{11}, s_{22} of the selection matrix $\boldsymbol{\Omega}$ from 1 to 0.

The schematic structure of hybrid position and force control algorithm is represented in Figure 6.6.

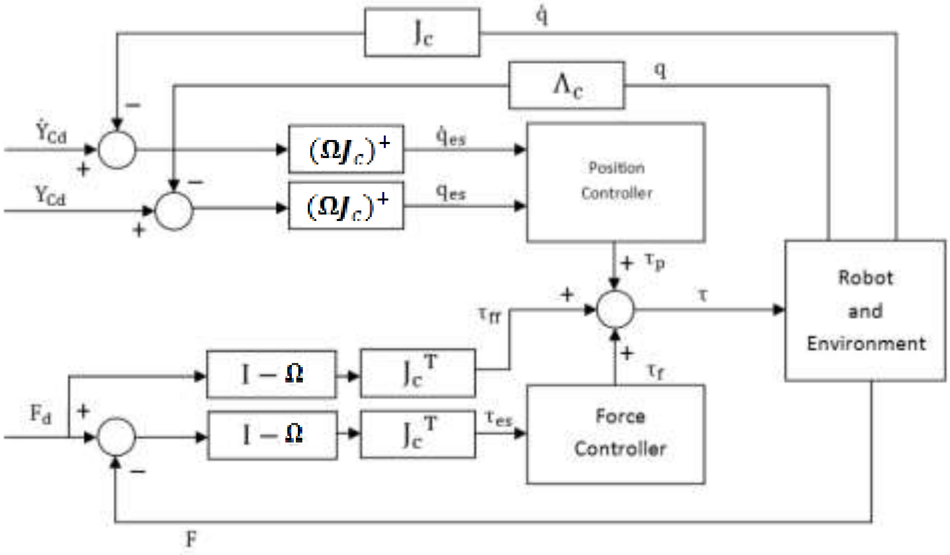

Figure 6.6: Block diagram of the position/force hybrid control of Azenha and Machado's algorithm.

6.2.3 Comparison

Compare to Khatib & Burdick's diagram, Azenha & Machado's method is much concise. Khatib & Burdick's need more parameters than Azenha & Machado's. Khatib & Burdick's requires the Jacobian, errors of position and velocity, the kinetic energy matrix, the vector of end-effector centrifugal and Coriolis forces, the gravity matrix, the force vectors while Azenha & Machado's needs only the Jacobian, errors of position and velocity, and the force vectors. In position control, when the two systems share the same parameters

$$k_p = 1000, k_v = 10,$$

When

$$\boldsymbol{\Omega} = \begin{bmatrix} 1 & 0 \\ 0 & 1 \end{bmatrix}.$$

Both coordinate x and y are position controlled, and the desired positions were $x_d = 0.5, y_d = 0.2$. The results show obvious oscillations when utilising Khatib & Burdick's algorithm, especially when the target position is close to the original position. The preceding positions are $x_0 = 0.56, y_0 = 0.13$.

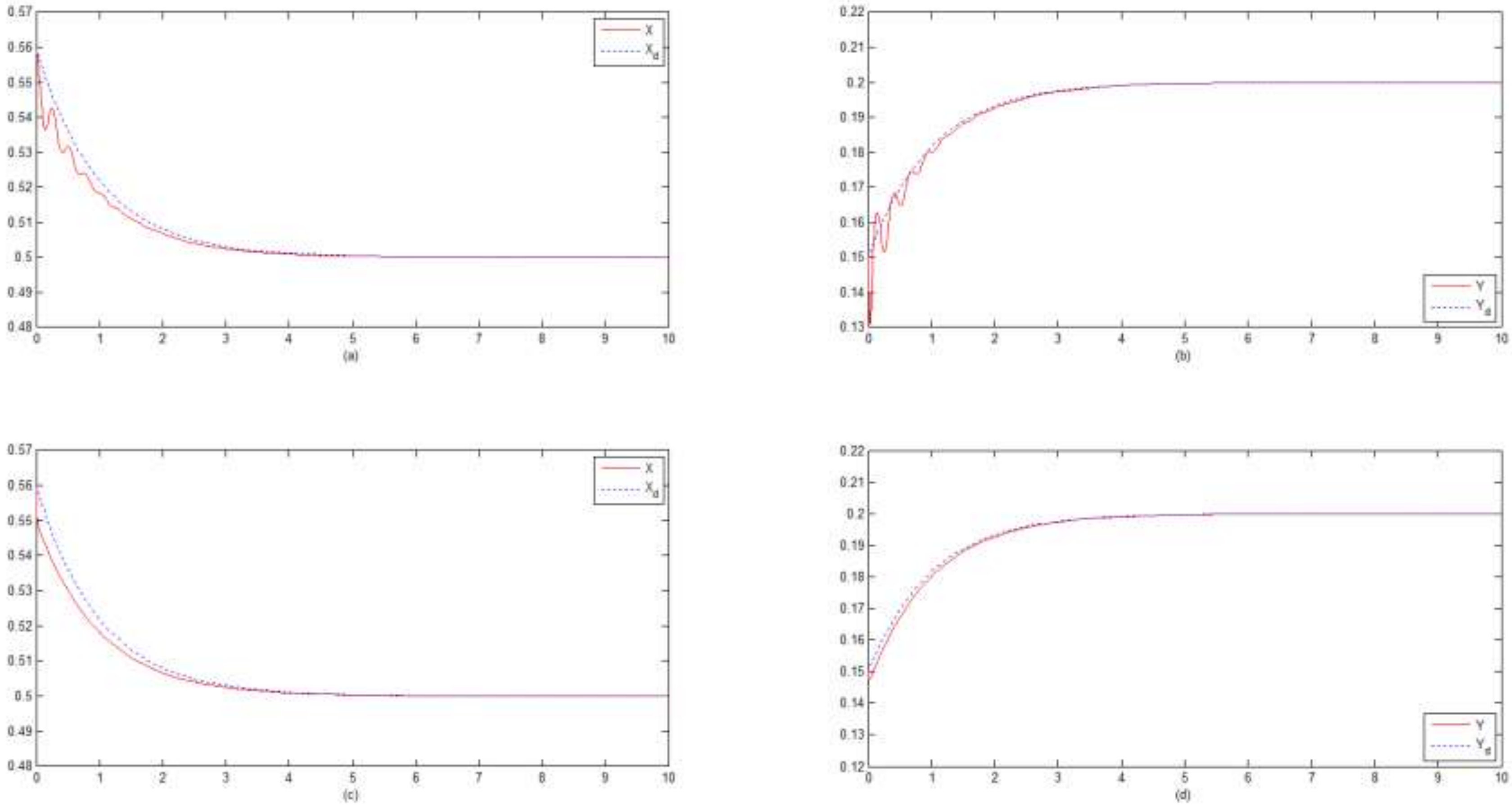

Figure 6.7: Time responses of the position/position control system: (a) Trajectories on coordinate axis X, (b) Trajectories on coordinate axis Y utilising Khatib & Burdick's algorithm; (c) Trajectories on coordinate axis X, (d) Trajectories on coordinate axis Y utilising Azenha & Machado's algorithm

X, Y are real-time value on coordinate X and Y. While X_d, Y_d are desired values.

When

$$\boldsymbol{\Omega} = \begin{bmatrix} 1 & 0 \\ 0 & 0 \end{bmatrix},$$

the system is a position/force control system. Coordinate x is position controlled, coordinate y is force controlled.

The soft wall is placed at 0.2 on coordinate y. Desired position is $x_d = 0.2$, and desired force is $F_d = 10$. The results show that Khatib & Burdick's algorithm and Azenha & Machado's algorithm all work precisely. X, Y are real-time value on coordinate X and Y. While X_d, Y_d are desired values.

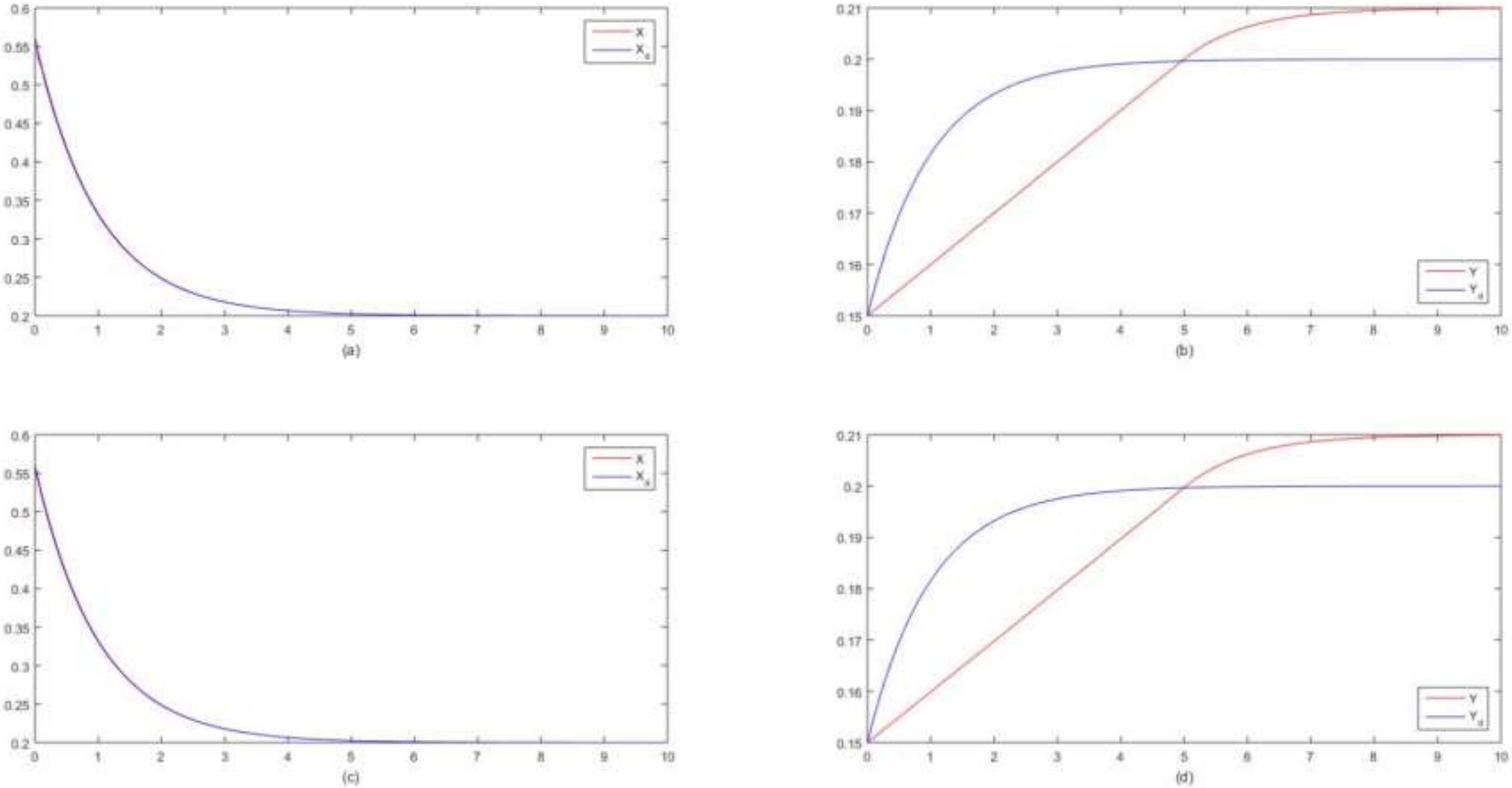

Figure 6.8: Time responses of the position/force control system: (a) Trajectories on coordinate axis X, (b) Trajectories on coordinate axis Y utilising Khatib & Burdick’s algorithm; (c) Trajectories on coordinate axis X, (d) Trajectories on coordinate axis Y utilising Azenha & Machado’s algorithm.

When

$$\mathbf{\Omega} = \begin{bmatrix} 0 & 0 \\ 0 & 1 \end{bmatrix},$$

the system is a force/position control system. Coordinate x is force controlled, coordinate y is position controlled.

The soft wall is placed at 0.2 on coordinate x. Desired position is $y_d = 0.2$, and the desired force is $F_d = 10$. The results show both algorithms work well

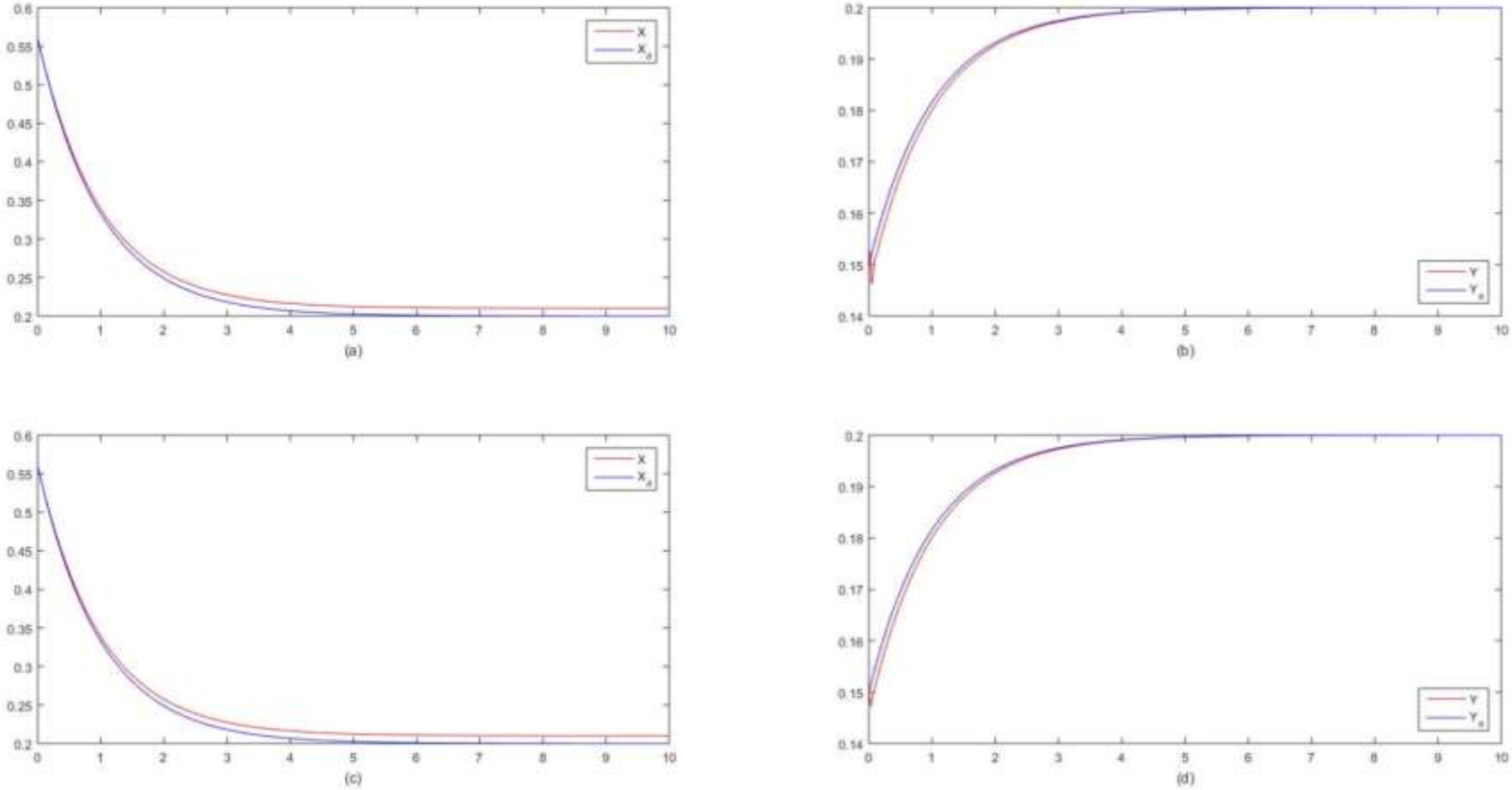

Figure 6.9: Time responses of the force/position control system: (a) Trajectories on coordinate axis X, (b) Trajectories on coordinate axis Y utilising Khatib & Burdick’s algorithm; (c) Trajectories on coordinate axis X, (d) Trajectories on coordinate axis Y utilising Azenha & Machado’s algorithm.

X, Y are real-time value on coordinate X and Y. While X_d, Y_d are desired values.

When

$$\mathbf{\Omega} = \begin{bmatrix} 0 & 0 \\ 0 & 0 \end{bmatrix},$$

the system is a force/force control system. Coordinate x is force controlled, coordinate y is force controlled as well.

The soft wall is placed at 0.2 on coordinate y and x. $F_{d1} = 10, F_{d2} = 10$.The results show that both algorithm work consistently.

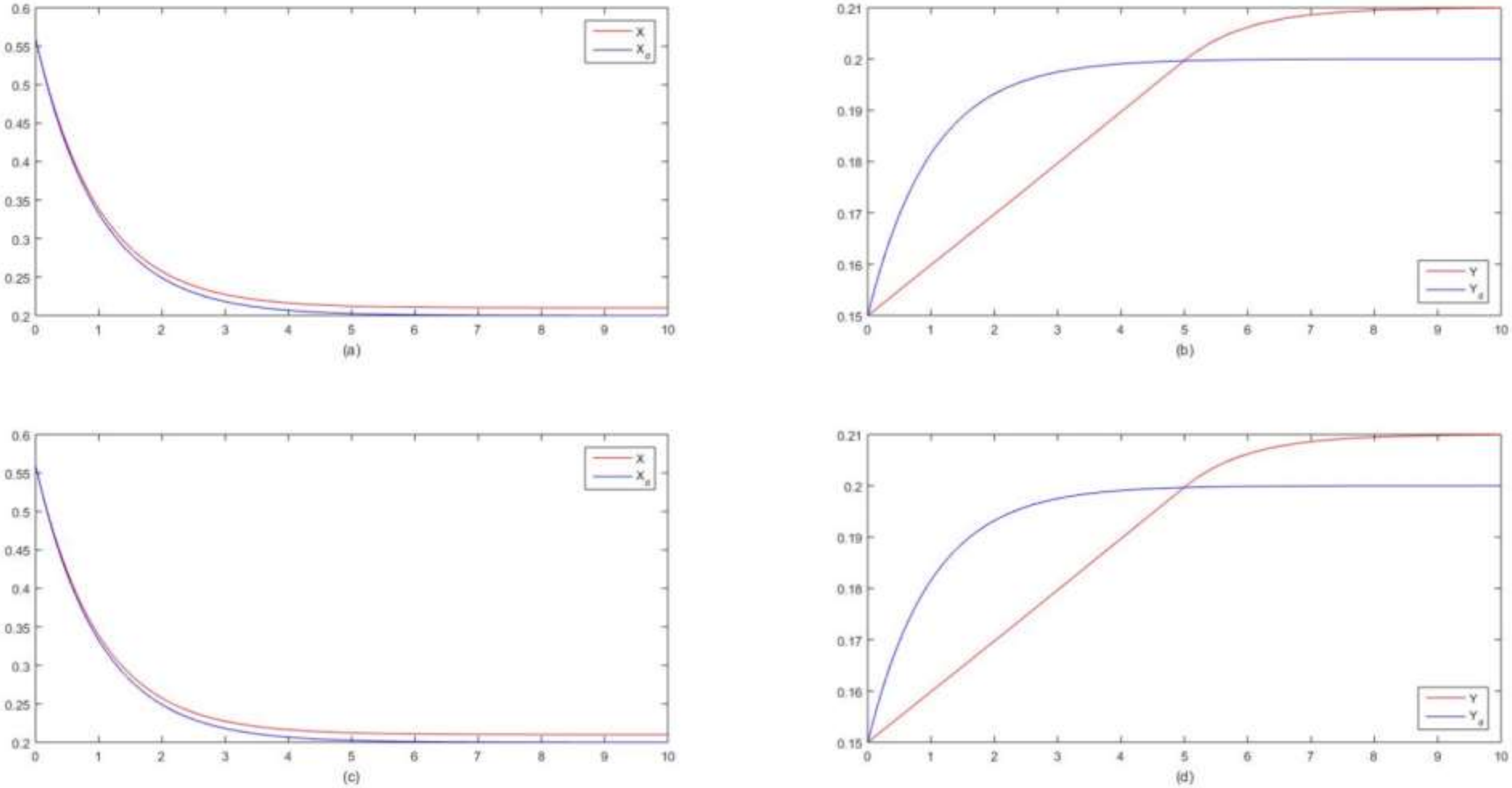

Figure 6.10: Time responses of the force/force control system: (a) Trajectories on coordinate axis X, (b) Trajectories on coordinate axis Y utilising Khatib & Burdick’s algorithm; (c) Trajectories on coordinate axis X, (d) Trajectories on coordinate axis Y utilising Azenha & Machado’s algorithm.

To sum up, when it is position/position control, Khatib & Burdick’s algorithm has obvious oscillation so that it is not as good as Azenha & Machado’s algorithm. The other results like position/force control, force/position control and force/force control showed that Azenha & Machado’s algorithm work consistently with Khatib & Burdick’s algorithm. Moreover, as Khatib & Burdick’s need more parameters than Azenha & Machado’s so that we consider Azenha & Machado’s algorithm is better than Khatib & Burdick’s algorithm.

6.3 Hybrid position/force control of the robotic retractor

In the next model, the retractor will touch a soft tilted wall and move to the desired position on the wall of Cartesian coordinate C. The model of the retractor manipulator has been done depend on Azenha & Machado’s algorithm. The retractor manipulator has one rotational joint and a prismatic joint. The desired position is on y_c, and the desired force is placed on the director of x_c.

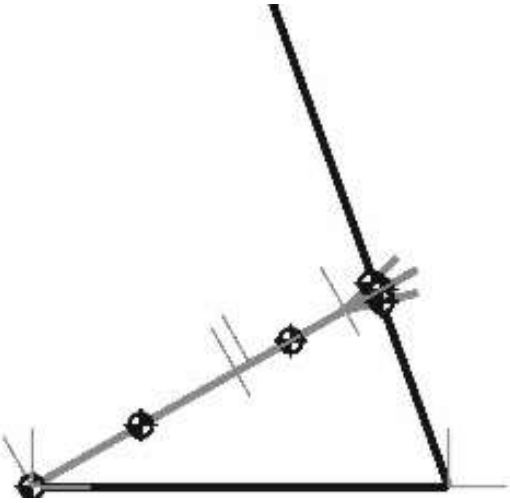

Figure 6.11: Retractor with manipulator

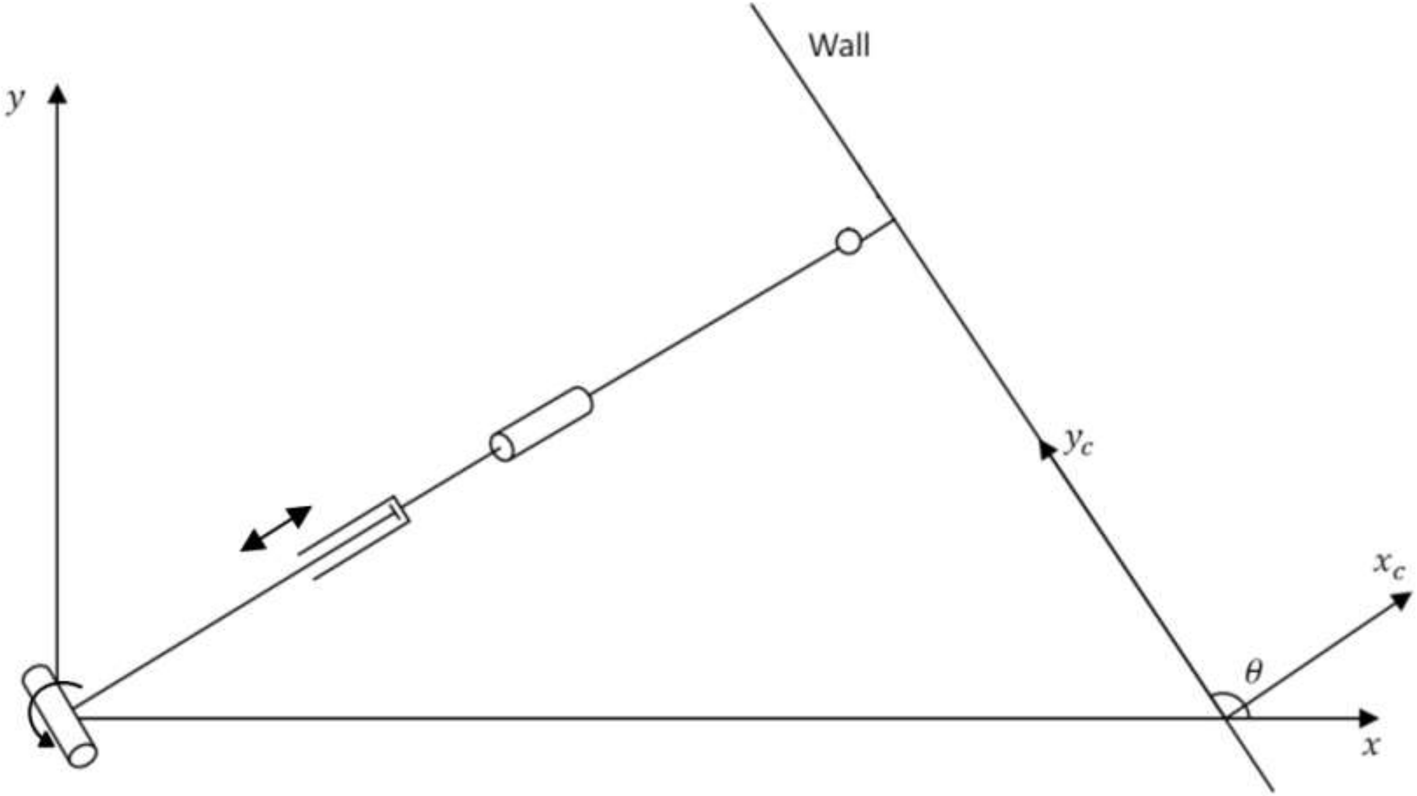

Figure 6.12: Diagram of the retractor with manipulator

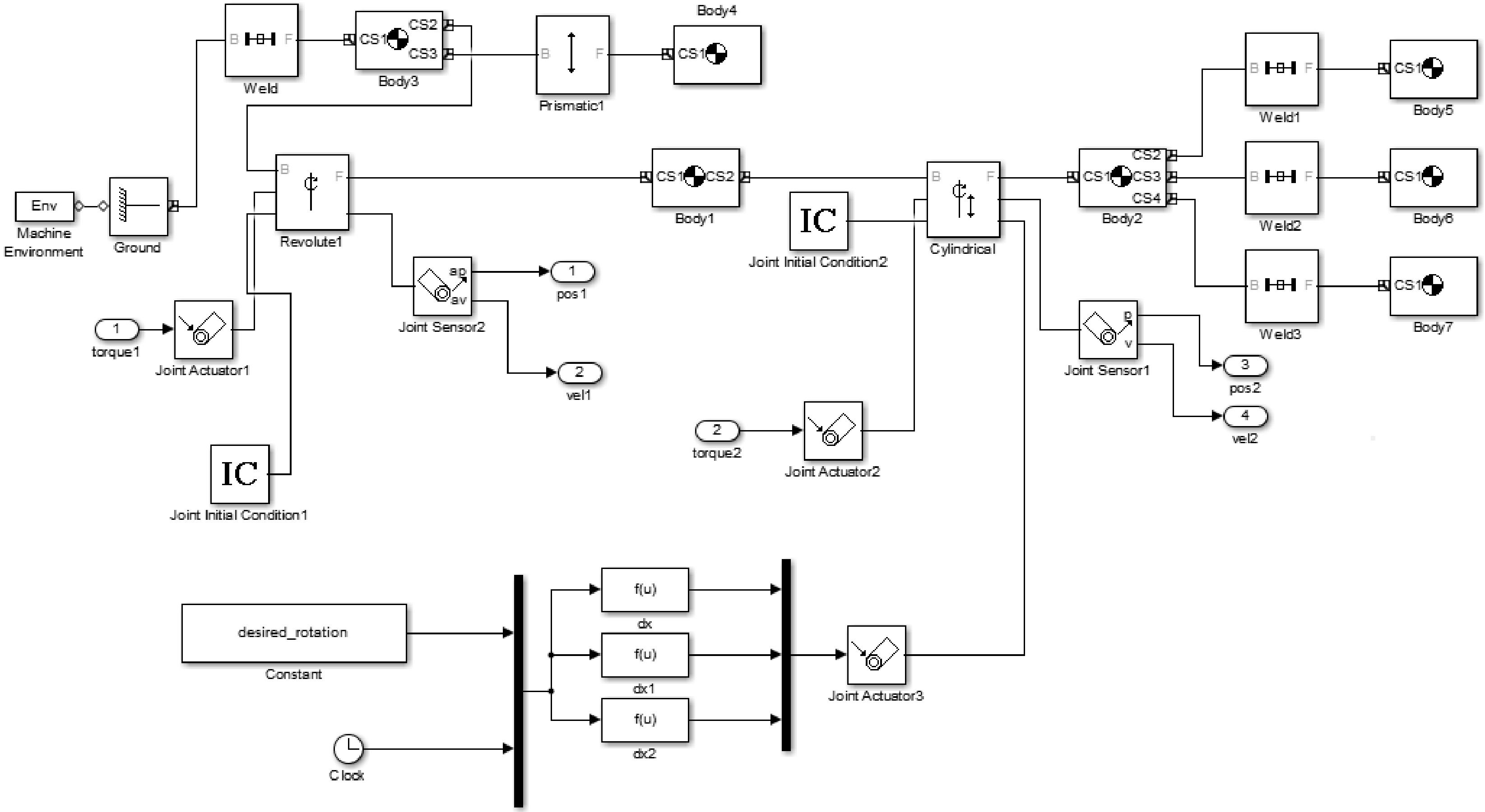

Figure 6. 13 2-joint manipulator and retractor Simulink diagram

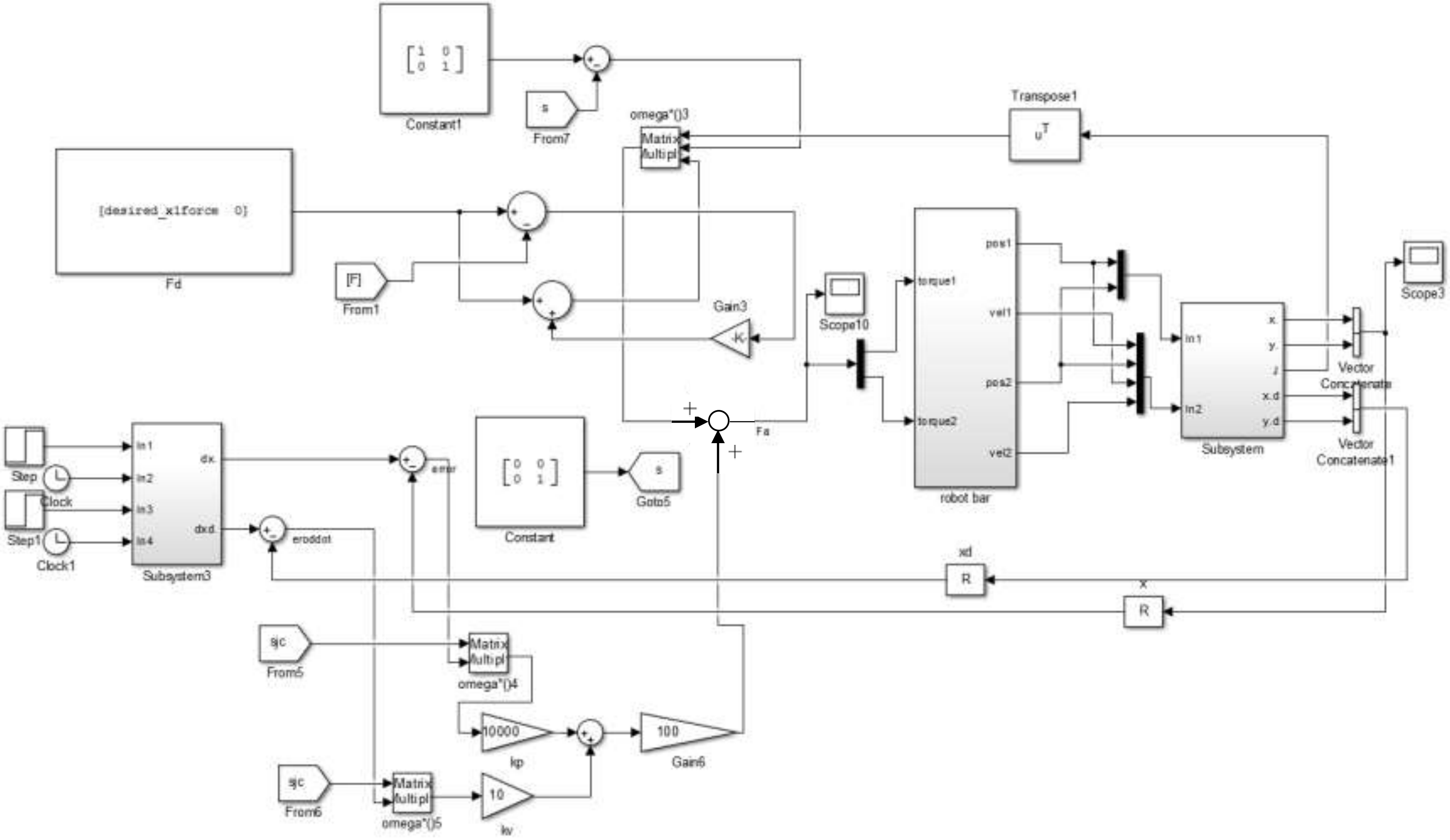

Figure 6. 14 Azenha & Machado’s hybrid position/force control diagram

In the coordinate C, y_c is the tilted wall. Consider the wall is a soft tissue. The target position and force are $y_d = 0.5,\ F_d = 10$.

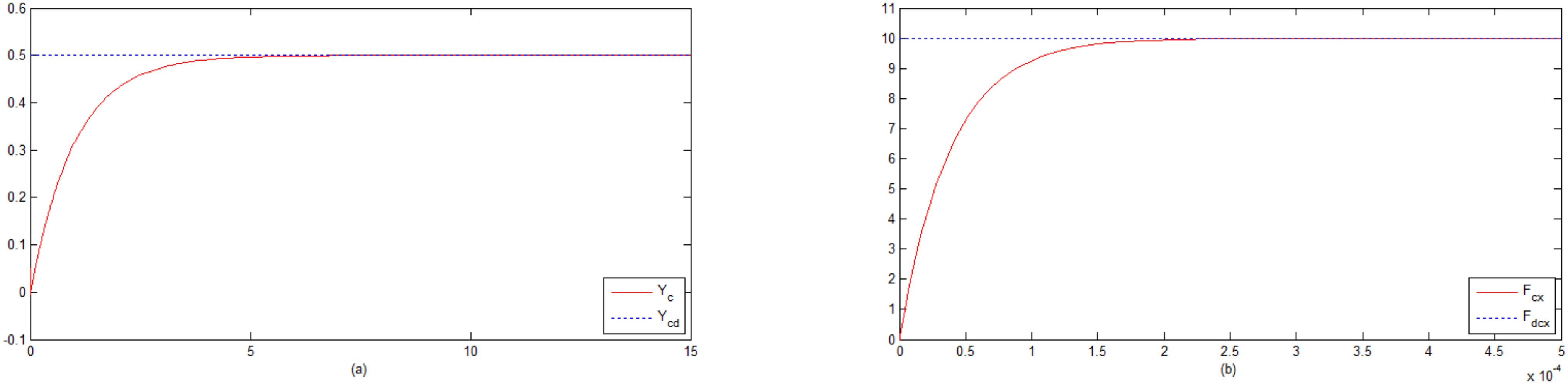

Figure 6.15: Time responses of the position/force hybrid control system:(a) Position; (b) Force.

Figure 6.15 shows the time responses of the position force hybrid control. It took approximate 8 seconds for manipulator to reach the target position, and it took 2.5×10^{-4} seconds to obtain the target force.

6.3 Summary

To sum up, this chapter first describes active compliance control including impedance control and hybrid position/force control, and then compared two methods of hybrid position/force control. One method is from Khatib, and another is method is from Azenha. The comparison result showed that Azenha & Machado's method is better than Khatib & Burdick's method. Later, the model of the robotic retractor touching soft wall utilising Azenha &Machado's method was carried out.

Chapter 7

Time-optimal control of the retractor

7.1 On-off control

An on-off controller is a feedback controller that switches abruptly between two states. The on-off controller is also known as bang-bang controller. To solve a wide range of control problems, on-off controller is carried out as an optimal strategy to minimize the total time taken to perform a task or some function of it. On-off control related to applications like robotics, rocket flight, cranes and physics (Kim et al. 2001), game theory(Olsder 2002), chemistry (Dadebo, 1998), biological (Ledzewicz and Schättler 2002a, 2002b), and socio-economic system (Kaya, 2004). Due to the discontinuous control signals, systems that include on-off controllers are variable structure systems (VSS). The key question is whether the systems responds in a time-optimal way or in minimum time in response to the switched on or off controls. Pedro, Mthethwa and Nyadoro (2003) presented algorithms to compute time-optimal solutions for a two-link robotic manipulator operating in the horizontal plane subject to control constraints. In this chapter, we shall briefly review these aspects as they could, in principle, be applied to the control of the retractor, although we have not been able to implement them in the prototype of the retractor.

Kaya (2004) gave a formulation of the problem solving by an on-off control. The on-off constrained optimal control problem is shown as below,

$$\begin{cases} \qquad\qquad minimize \quad \emptyset\left(x\left(t_f\right), t_f\right) \\ subject\ to \quad \dot{x}(t) = f\left(x(t), u(t)\right), \qquad u(t) \in \{-1, 1\} \\ \qquad\qquad x(t_0) = x_0, x\left(t_f\right) = x_T, \end{cases} \tag{7.1}$$

where $t \in [t_0, t_f]$, the terminal time t_f is free, the state $x: [t_0, t_f]$ is continuous, and f is smooth in x except possible at the time points where the control $u: \left[t_0, t_f\right]$ switches between -1 and 1.

7.2 Pontryagin’s minimum principle

The control parameter u(t) lies in some admissible region while constrained input control problems provide the admissible region. To solve these problems, we must replace the stationarity condition Hamiltonian, $H_u = 0$, with a more general condition called Pontryagin’s minimum principle (Boltyanskii, 1956). The Pontryagin’s minimum principle is used in optimal control theory for finding the best possible control for taking a dynamical system from one state to another. The control Hamiltonian takes an extreme value over control. When the extreme value is a maximum, Hamiltonian leads to a maximum hence. On the contrary, Hamiltonian leads to a minimum hence when the extreme value is a minimum.

Consider u is the set of values of permissible controls. Then the principle states u^* must satisfy,

$$H(x^*, u^*, \lambda^*, t) \leq H(x^*, u^* + \delta u, \lambda^*, t)$$

for all admissible δu.

A linear generalization on-off theorem with constrained input magnitude is shown below. Consider the linear control system model as,

$$\dot{\mathbf{x}} = \mathbf{Ax} + \mathbf{Bu} \tag{7.2}$$

A and **B** are constant $n \times n$ and $n \times m$ matrices respectively.

The performance index is,

$$J(t_0) = \int_{t_0}^{T} dt \tag{7.3}$$

Constraints is,

$$|u(t)| \leq constant \tag{7.4}$$

Optimal Control is,

$$u^*(t) = -sgn(B^T \lambda(t)) \tag{7.5}$$

The proof of this follows from applying Pontryagin's minimum principle to get

$$(\lambda^*)^T Bu^* \leq (\lambda^*)^T Bu$$

The left side is minimized by choosing u to be as small as possible, which depends on the sign of $(\lambda^*)^T B$.

7.3 Application of time-optimal control

Figure 7.1 shows the 2-joint manipulator with the dual-hand fan retractor. One of the 2-joint manipulator joints is a rotational joint while another joint is a prismatic joint.

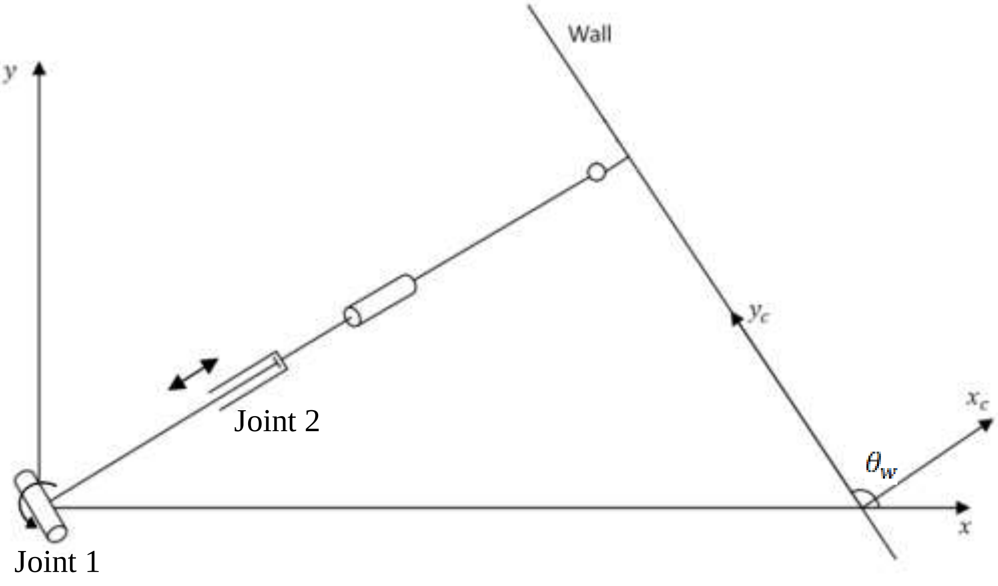

Figure 7.1: Diagram of the 2-joint manipulator with the dual-hand fan retractor

Application of Lagrangian formalism to the 2-link robotic manipulator gives the dynamic equation show as follow.

$$\mathbf{H}(\theta)\ddot{\theta} + \mathbf{C}(\theta, \dot{\theta}) + \mathbf{G}(\theta) = \mathbf{\Gamma} \tag{7.6}$$

$$\mathbf{H}(\theta) = \begin{bmatrix} m_1 l_1^2 + I_1 + I_2 + m_2 l_2^2 & 0 \\ 0 & m_2 \end{bmatrix} \tag{7.7}$$

$$\mathbf{C}(\theta, \dot{\theta}) = \begin{bmatrix} 2m_2 l_2 \dot{\theta}_1 \dot{l}_2 \\ -m_2 l_2 \dot{\theta}_1^2 \end{bmatrix} \tag{7.8}$$

$$\mathbf{G}(\theta) = \begin{bmatrix} g c_1 (m_1 l_1 + m_2 l_2) \\ m_2 g s_1 \end{bmatrix} \tag{7.9}$$

Where $\mathbf{H}(\theta)$ is the links' inertia matrix, $\mathbf{C}(\theta, \dot{\theta})$ is the vector of the Coriolis and centripetal torques, and $\mathbf{G}(\theta)$ is the vector of the gravitational torques. Here, $c_1 = \cos\theta_1$ and $s_1 = \sin\theta_1$.

Control constraints are shown as follow,

$$U_{1min} \leq u_1(t) \leq U_{1max} \tag{7.10}$$

$$U_{2min} \leq u_2(t) \leq U_{2max} \tag{7.11}$$

To develop the time-optimal controller, we linearize the equations of motion. The reason for linearising the nonlinear system is because the system is only weakly coupled. By linearising the system, we may decouple the system into two independent second order sub-systems. Thus, it is also required that there are two independent control effectors to implement the controls. Linearising (7.5), (7.6), (7.7), get

$$\mathbf{H}(\theta) = \begin{bmatrix} m_1 l_1^2 + I_1 + I_2 + m_2 l_2^2 & 0 \\ 0 & m_2 \end{bmatrix} \tag{7.12}$$

$$\mathbf{C}(\theta, \dot{\theta}) = \begin{bmatrix} 0 \\ 0 \end{bmatrix} \tag{7.13}$$

$$\mathbf{G}(\theta) = \begin{bmatrix} g (m_1 l_1 + m_2 l_2) \\ m_2 g \theta_1 \end{bmatrix} \tag{7.14}$$

It is general to linearise the term $\cos\theta_1$, it is replaced by 1 and the term $\sin\theta_1$ by the variable term θ_1.

$$c_1 = 1, s_1 = \theta_1 \tag{7.15}$$

From the first dynamic equation,

$$I_{11}\ddot{\theta} = I_{11} \cdot u - I_{11} \cdot c_{n1} = I_{11} \cdot u - I_{11} \cdot \frac{g(m_1 l_1 + m_2 l_2)}{m_1 l_1^2 + I_1 + I_2 + m_2 l_2^2} \tag{7.16}$$

Here, I_{11} is the first term of matrix **H**. $I_{11} \cdot u$ is the rotational joint control torque.

From the second dynamic equation,

$$m_2\ddot{l} = m_2 \cdot u - m_2 \cdot c_{n2} = m_2 \cdot u - m_2 \cdot \frac{m_2 g \theta_1}{m_2} \tag{7.17}$$

Here $m_2 \cdot u$ is the prismatic joint control force.

Consider $c_{n1} = 0$ and $c_{n2} = 0.4$, the initial $\theta_0 = 0.9, l_0 = 0.5, \dot{\theta}_0 = 0.1, \dot{l}_0 = 0.1, u = \pm 1$. Get results of states response and phase plane shown as follows.

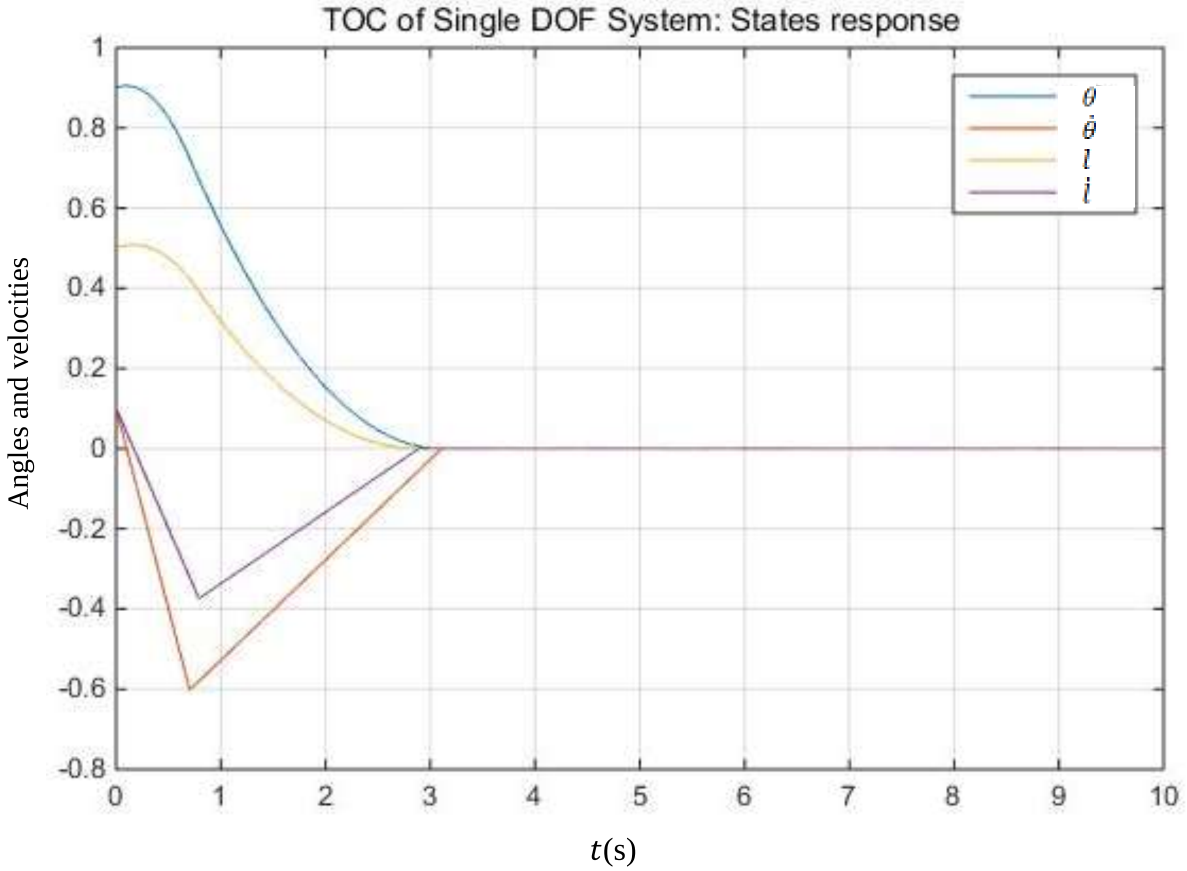

Figure 7.2: Time-optimal control of single DOF system: States response.

Figure 7.2 shows the time-optimal control states response. The yellow curve and green curve are the position trajectories of joint 1 and joint 2, separately. The orange curve and purple curve are velocity profiles. The initial value of the rotational joint error θ was 0.9, and the initial value of the prismatic joint error was 0.5. The velocities dropped to zero first and increased in the opposite direction. The velocities increased to certain values and decreased to zero when the error of joint 1 and joint 2 are zero as well.

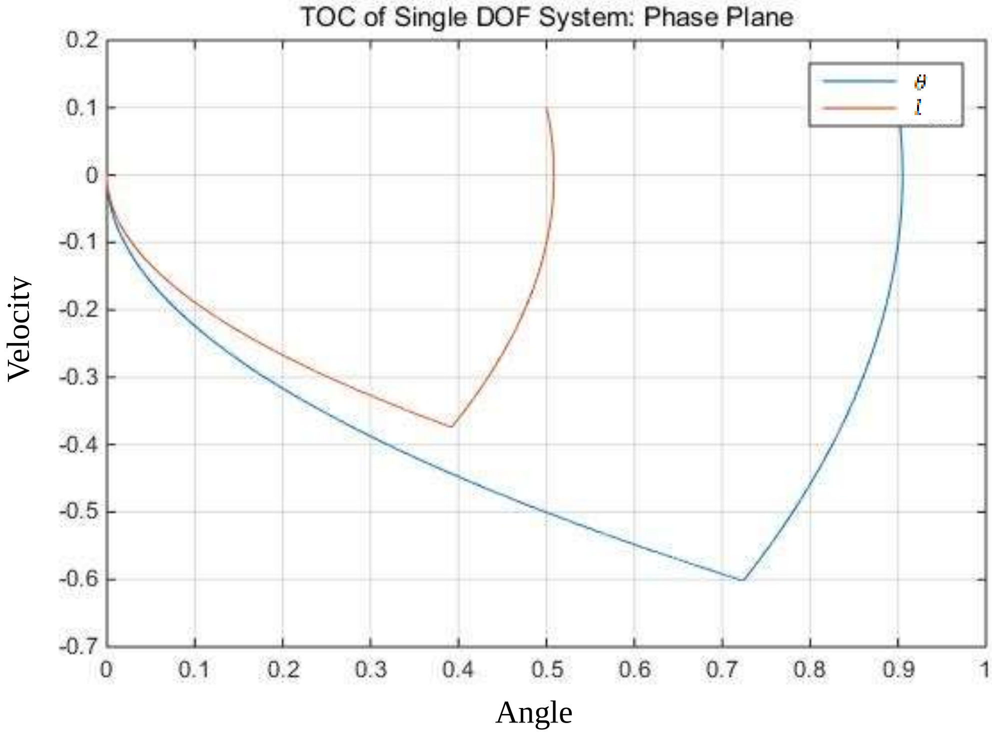

Figure 7.3: Time-optimal control of single DOF system: Phase Plane.

In Figure 7.3, two curves are showing the phase plane. The blue curve shows the phase plane for joint-1, and the orange curve shows the phase plane for joint-2. Initially, blue curve starts at (0.9, 0.1) and orange curve starts at (0.5, 0.1). The switching equation is $\frac{X_2^2}{2(u-c_{ni})}$. The trajectory follows the parabola

$$X_1(t) = \frac{X_2^2}{2(u-c_{ni})} + C \tag{7.25}$$

when the $u = -1, C$ is a constant. After the blue curve and orange curve reach $\frac{X_2^2}{2(u+c_{ni})}$, the two curves follow their trajectory move to zero follow the switching trajectory $\frac{X_2^2}{2(u-c_{ni})}$, when $u = 1, C = 0$. The phase plane plot above is a typical example of the phase-plane plot which obtains for the time-optimal control of the retractor, as in each degree of freedom, the value of the constant c would be different. For this reason, we have shown the phase-plane plots for two different values of the constant c_{ni}. Ode45, a solver in MATLAB, is implemented in solving the time-optimal problem. Thus we conclude that the linear theory of time-optimal control of a second order system may be applied to the dynamics of each degree of freedom.

7.4 Summary

In this chapter, the On-off control and Pontryagin’s minimum principle are introduced. On-off control, also called bang-bang control, switches abruptly between two states. On-off control minimizes the total time for performing a task. Later, the Pontryagin’s minimum principle is introduced. The Pontryagin’s minimum principle is used for taking a dynamical system from one state to another. Then, a 2-joint manipulator (with one prismatic joint and a rotational joint) is controlled by utilising On-off control and there is a fan retractor attached on the end of the 2-joint manipulator.

Chapter 8

Conclusions and future work

8.1 Conclusions

In this thesis, a dual-head fan retractor for laparoscopic applications was designed in SolidWorks. The dual-head fan retractor consists of five sections: two fan devices, the tubular element, the wrist and the handle. There are two fan-shaped end-effectors assembled on the distal end of the two fan devices. The feature of the dual-head is that it has two end-effectors which can provide a hand-holding shape during laparoscopic colorectal surgery. The dual-head fan retractor has four degrees of freedom. The first is associated with the opening and collapsing of the fan blades; the second is the rotation of the palm; the third is rotation of the front body; the fourth is rotation of the entire fan device as single unit. In short, the dual-head fan retractor has more flexibility than the traditional retractors illustrated in Chapter 2. Later, fabrication of the dual-head fan retractor was accomplished. It is a scaled version, which is 2.5 times larger than the real size dual-head fan retractor designed originally. Only the 2.5 ratio prototype was fabricated. One of the components was built by AISI 301 stainless steel while other components were built by the 3D printer. The 2.5 ratio prototype showed the four degrees of freedom and movements. Although the real sized dual-head fan retractor was not fabricated because 3D printed component with little dimension is fragile, we found another way to do the stress analysis on the real sized dual-head fan retractor by using SolidWorks Simulation. To do the stress analysis, first step was defining all the components material in the dual-head fan retractor. Materials for clinical applications like titanium and stainless steel were presented and compared. The titanium has an outstanding elastic modulus, but we did not consider titanium because it is too expensive. The laminated bar was built of AISI 301 stainless steel while other components are defined as material AISI 304 and AISI 420 stainless steel. That is because the components produced by AISI 304 and AISI 420 have better tensile strength and elastic modulus. The next step of stress analysis was mash drawing. The gridding has a high density on little sections, for example, the gear tooth of the clutch tooth. Later, in the next step the performance of the device was tested and the static component was defined. Next, the contact relationship between components was established. Then, the next step was to set a 1.635 N load which was calculated according to the intestine weight. The system then generated results like the displacement figure, the factor of safety figure and stress distribution figure. The results designated that the weakest part of the fan retractor is the tooth flank of the tooth clutch. However, the retractor can obtain better tensile strength if titanium is applied on the retractor.

Manipulator dynamics introduced the connection between the body movement and the force. The dynamic of the multi-body system was described in three approaches: first, the Newton-Euler approach; second, the recursive Newton-Euler formulation; third, Lagrangian method. As for the dual-head fan retractor, the fan-shaped end-effector has three blades. Each of the blades can be considered as a spherical pendulum. Then, we modelled the dynamic system of the blade. The mathematical model of the fan blades was carried out later in chapter 4.

A 3-joint manipulator with three rotational joints was modelled and controlled. It was the preparatory work for study the multiple-joint robotic manipulator. The computed torque control including PD feedback control was carried out for controlling the manipulator. The results showed that the computed torque control is precise and efficient. Later, the dual-head fan retractor attached on a 2-joint manipulator was modelled using the Lagrangian formulation. The 2-joint manipulator has one joint as a rotational joint and another as a prismatic joint. At the end of chapter 5, a 3-joint manipulator, with two rotational joints and one prismatic joint, was mathematically modelled. The 3-joint manipulator was considered as a better manipulator when comparing with the other two manipulators explained early in this chapter. That is because the 3-joint manipulator has bigger working space and multiple working gestures. The prismatic joint makes the pushing and pulling movements more convenient.

Impedance control and its appropriateness were illustrated in Chapter 6. The variable structure impedance control was introduced by using Heping Chen’s algorithm. Later, the hybrid position/force control law was utilised for controlling a 2-joint manipulator. The 2-joint manipulator has two rotational joints. In this thesis, two hybrid position/force control methods was chosen to compare. One is the method from Khatib & Burdick, and another is the method from Azenha & Machado. Results showed that Azenha’s method needs fewer input parameters and its result has no oscillation when comparing with Khatib’s method. Thus, Azenha’s method was chosen to control the robotic manipulator. The robotic manipulator is a 2-joint manipulator which has one rotational joint and one prismatic joint. The results showed that the hybrid position/force control of Azenha & Machado’s worked precisely.

A time-optimal control was set up on to control the robotic manipulator. The robotic manipulator is a 2-joint manipulator which has one rotational joint and one prismatic joint. The 2-joint manipulator has two degrees of freedom. The dynamic equation for each degree of freedom was considered as a second order system. The linear theory was applied in the time-optimal control.

8.2 Future work

There are various works need to be investigated to make the design and control of the robotic retractor more precise.

Artificial intelligence (AI) modelling, as a branch of computer science, includes numerical methods, programming systems and hardware systems. The techniques from AI can help optimising mathematical modelling. A variety of algorithms for geometric reasoning will provide effective mechanisms. In Chapter 4, the mathematical model of the fan blades was illustrated. In the future, AI modelling will be utilised to provide more efficient mechanisms for the robotic retractor.

The robotic retractor system should be miniaturised before to be usable in the surgical application. Optimal miniaturisation on the end-effector should be carried out for the purpose of minimising the trauma. The suggestion to make this happen is to use titanium components. The reason why we want to choose titanium is because of its excellent elastic modulus and tensile strength. It is well known that the elastic modulus and tensile strength of titanium are much bigger than that of stainless steel. Thus, components with small size and robust property can be built by using titanium. The shortcoming is that titanium is much more expensive than stainless steel. The future work will be design and fabrication of the real sized dual-head fan retractor. The clinical trial will be established later.

Chapter 6 discussed two hybrid position/force control methods from Khatib & Burdick and Azenha & Machado. Two methods have been simulated on a two-joint manipulator modelled by MATLAB SimMechanics. The future work will be the implementation of both of the methods from Khatib & Burdick and Azenha & Machado. A two-joint manipulator will be built and fabricated. Later, the two-joint manipulator will be controlled through MATLAB.

In the further study, a 3-joint manipulator with two rotational joint and a prismatic joint will be modelled and controlled. The reason of utilising the 3-joint manipulator is because the 3-joint manipulator has more gestures than the 2-joint manipulator. With the help of the prismatic joint, the surgeon can easily pull and push the intestine.

The time-optimal control based on Pontryagin Minimum Principle (PMP) has been chosen to solve a nonlinear two-point boundary value problem established by the robotic retractor model. The future work will be the implementation of the time-optimal control by using MATLAB. First, a robotic retractor system should be established; second, build the controller by using MATLAB Simulink library; third, run the system.

Appendix A

Stress analysis

A.1 Calculation of force

In Figure A.1, the diagram of the retractor holding shape end-effector is shown. For getting the force that would be placed on the end-effector, we need to first aware the touching area. The statistics in Figure A.2 is measured.

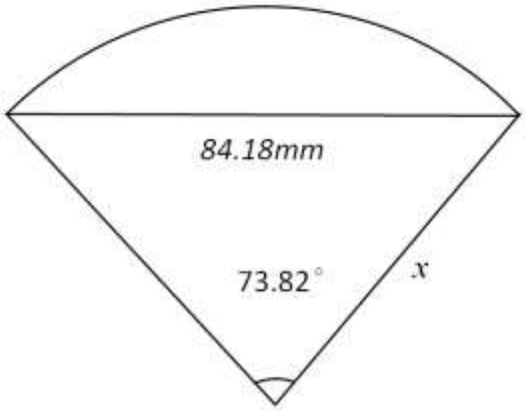

Figure A.1: Parameters of the end-effector.

There is an unknown parameter x in the figure A.2. Get the value for using cosine law,

$$cos\,A = (b^2 + c^2 - a^2)/2bc \tag{3.1}$$

Here, A=73.82° , b=c=x, a=84.19 mm. Get,

$$cos(73.82°) = (2x^2 - 84.18^2)/2x^2 \tag{3.2}$$

Then calculate and have

$$x=70mm.$$

To get the touching area, use the fan area formula

$$S = \pi x^2 \frac{A}{360} \quad (3.3)$$

As x=70 mm, A=73.82°. Have,

$$S \approx 3156.6\, mm^2$$

The weight of the intestine on the retractor will follow the formula below,

$$m = \rho V = \rho S h \quad (3.4)$$

here, m is the mass of the intestine on the retractor, ρ means the density of intestine, S is the value of the touching area, h is the height of the intestine.

As the diameters of the large intestine and small intestine are 65mm and 40mm separately.

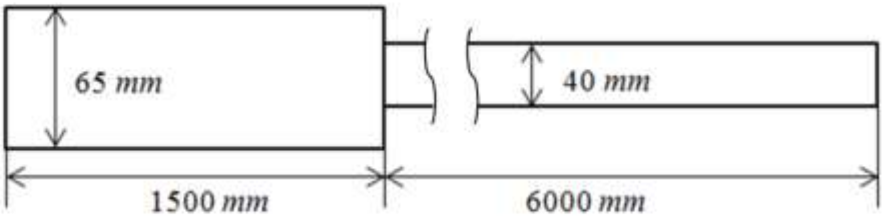

Figure A.2: Diagram of large intestine and small intestine.

Table A.1: The approximate dimension and weight of large intestine and small intestine.

	Large intestine	Small intestine
Weight	2kg	1.75kg
Length	1500mm	6000mm
Diameter	65mm	40mm

The volumes of large intestine and small intestine are,

$$V_1 = \pi(\frac{D_1}{2})^2 h_1 = \pi(\frac{65}{2})^2 1500 = 4977460\, mm^2$$

$$V_2 = \pi(\frac{D_2}{2})^2 h_2 = \pi(\frac{40}{2})^2 6000 = 7539822\, mm^2$$

For getting the ρ,

$$\rho = \frac{m_1 + m_2}{V_1 + V_2} = \frac{2000 + 1750}{4977460 + 7539822} = 0.0003\ g/mm^3$$

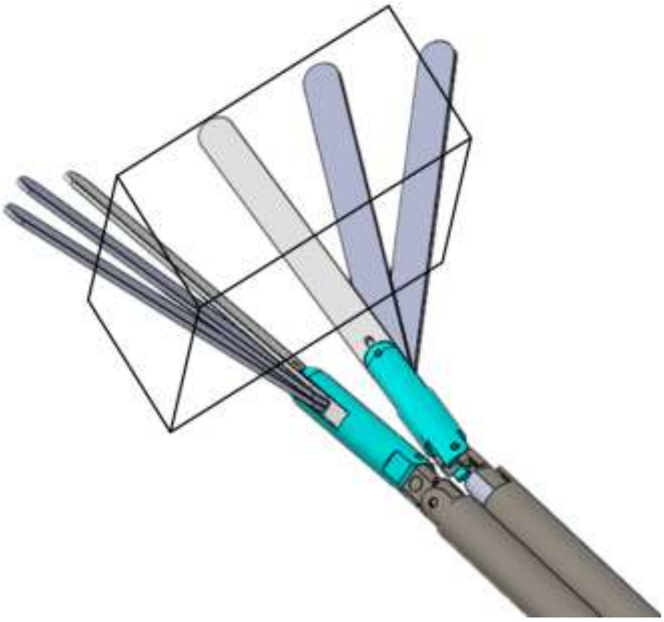

Figure A.3: Dual-head fan retractor with loads.

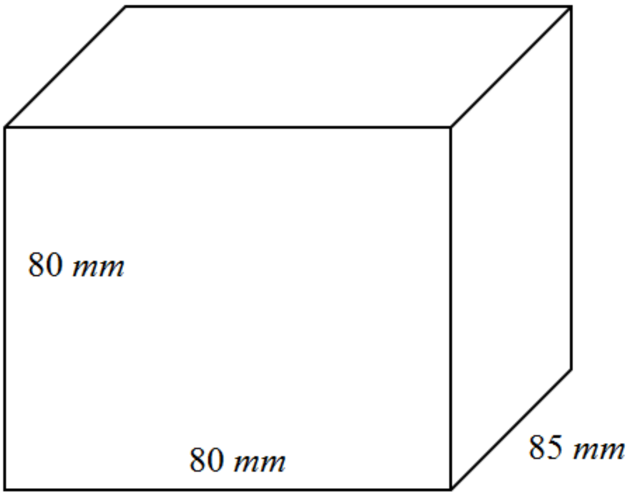

Figure A.4: Loaded intestine concept.

The loaded intestine weighs,

$$m = \rho V$$

Intestine slips easily because the intestine mucus decreases the friction between tissues.

The biggest height h of the intestine will not be higher than 80 mm.

$$m = 0.0003 \times 80 \times 80 \times 85 = 163.5\ g$$

$$F = mg = 0.1635 \cdot 10 = 1.635N$$

The total force loaded on the blades of dual-head fan retractor is 1.635 *N* or less.

A.2 Metal materials selection

In manufacturing, materials selection is imperative and prior. There are multiple materials can be applied for fabrication of surgical instrument, like stainless steels and Titanium alloys. The material has excellent corrosion resistance and moderate strength is ideal for the manufacturing of laparoscopic surgical instrument.

Stainless steel 301, 303, 304, 316, 410, 420 and 430 are used for the hygienic application. The table below shows the contrast for the above stainless steels.

Table A.2: Contrast for stainless steel 301, 303, 304, 316, 410, 420 and 430.

Stainless Types	Typical Chemical Composition %			Characteristics	Typical applications
	Cr	Ni	C		
301	17	7	0.10	High strength, abrasion resistance, good formability	Wheel covers, spring, processing equipment
303	17	9	0.15	Good corrosion performance, High tensile strength	Dental scalers, dental explorers, dental and surgical forceps, kidney dishes, theatre tables, etc
304	18	8	0.06	Multipurpose	Tubing, architectural trim, hollow handles, screws, nuts, rivets, dental syringes and amalgam carriers, laboratory spatulas and mixing knives,

					dental clamps and support bands for dental fillings, retractors, orthodontic wire and tape, guide pins, dental tweezers, dental impression trays, internal panels and trays for sterilizing units
316	16.5	10.5	0.05	Pitting corrosion resistance	Heat exchangers, chemical equipment, dental scalers, dental explorers, dental and surgical forceps, kidney dishes, theatre tables, screws, nuts, rivets
316L	16.5	10.8	0.02	Low carbon minimizes carbide precipitation during welding	Heat exchangers, chemical equipment, dental scalers, dental explorers, dental and surgical forceps, kidney dishes, theatre tables, screws, nuts, rivets
410	11.5	-	0.14	General purpose, harden-able	Machine parts, dental tweezers, dressing forceps, tissue forceps, guide pins, retractors, laboratory spatulas and mixing knives, solid handles, screws, nuts, rivets

420	12.5	-	0.38	Increased harden-ability	Bone curettes, bone-cutting forceps, bone rongeurs, chisels and gouges, conchotomes, dental chisels, dental curettes, dental scalers, dental extraction forceps, dental filling, instruments, dental root elevators, dental explorers, dental tweezers, forceps, forceps with bow, handles, branch forceps, guide pins, laboratory, orthodontic pliers, probes, retractor, scissors with carbide inserts, scissors, laboratory spatulas and mixing knives, screws, nuts, rivets, spring, solid handle
430	16.5	-	0.05	General-purpose corrosion resistance	Processing and storage tanks/vessels, pumps, pipelines and tubes, taps and valves, fasteners, screwdrivers for bone screws, solid handles

The corrosion resistance of AISI 303 is lower than that of AISI 304. AISI 303 stainless steel is well known in medical devices manufacturing as its free-machining properties.

The weakness of 303 and 304 is that they are not implanted steel as they may expose to human tissue for more than one month. Austenitic AISI 316 is commonly known as surgical steel, and it is usually the choice for biomedical implants. AISI 410 and 420 have good corrosion resistance and high hardness. The heat treatment can harden AISI 410 and 420, and that’s why they are able for developing advanced mechanical properties. AISI 430 is a ferritic grade, and it also has a good corrosion resistance.

In stainless steel, large numbers of clinical application shown that nickel and its compounds could endanger human health. That is because ion nickel can permeate through the pore and sebaceous glands reaching the beneath of the human skin. The ion nickel affects the tissues beneath the human skin that may cause relevant clinical manifestations (Fullerton et al., 1986). As the disadvantages of ion nickel, many countries unveil policies to limit the nickel content in clinical and daily use stainless steels. Therefore, certain indicators strictly limit the nickel content in implant, dental and jewellery manufacturing. For example, AISI 316L and AISI 317L austenite surgical stainless steel contain nickel from 10%~14%, while stainless steel 304L has 8%~10% nickel molecule. The corrosion resistance of stainless steel mainly depends on the content of chromium ion. When the content of chromium reaches 12%, the chromium on the surface of the stainless steel will produce a thin film of passivation coat to stop further corrosion and oxidation. However, the corrosion and oxidation can happen again when damages affected by acid, alkali and salt. The content of carbon affects the corrosion of stainless steel. The higher content of carbon, the poorer corrosion the stainless steel may have.

To sum up, stainless steel with an austenite structure which has suitable content of nickel, chromium and lower carbon content is desired. Nickel and chromium help build the capability of corrosion and oxidation and increase the feature of cold processability and stretch feature. However, the more nickel, the higher price. To get a better corrosion, select a stainless steel type with the lower content of carbon is desired.

Titanium alloys like Ti-6Al-7Nb, Ti–6Al–4V, Ti–13Cu–4.5Ni, Ti–25Pd–5Cr, and Ti–20Cr–0.2Si are anti-magnetic, corrosion resistant and with light weight. Titanium alloys are considered to be ideal for biological and medical application but with expensive costs. Ti–6Al–7Nb, Ti–6Al–4V are popular titanium materials in medical and surgical applications. Table 3.3 notes a review of different fundamental features of Titanium (Geetha, et al., 2009).

Table A.3: Physical property for Ti-6Al-7Nb and Ti-6Al-4V.

Name	Density kg/m^3	Young’s modulus Gpa	Tensile Strength Mpa
Ti–6Al–7Nb	4520	120	1000
Ti–6Al–4V	4500	115	900

Titanium is anti-magnetic, corrosion-resistant, lightweight and robust. The characters make titanium alloy efficient for biological and medical applications. Titanium has good tensile strength and good corrosion-resistant from nitric acid, chloride, saltwater. Moreover, titanium has better flexibility and is much lighter than stainless steel. Less dimensional change is carried out in titanium than in stainless steel when they are heated or cooled. Additionally, titanium is suitable for magnetic resonance imaging applications, and it is chosen as the material of implant components for its biocompatibility. These advantages make titanium surgical instruments durable and practical. However, titanium is too expensive and may not be chosen for retractor fabrication.

In this report, material which has the advantage of biocompatibility, lower price, simple finishing and processing would be chosen to make the component of the fan retractor. After investigation, the AISI 304 and AISI 420 were suitable for manufacturing of our instrument and they come with cheap price. The characteristic of AISI 420 and AISI 304 is their increased hardenability after treated so that they were chosen for creating components that need to be robust and sturdy. AISI 301 has good elasticity and toughness after appropriate heat treatment and it was selected as the material for processing elongated laminated bars.

A.3 Stress analysis from SolidWorks Simulation

SolidWorks Simulation was utilised to get the stress analysis of the retractor. To get the results of stress analysis, we followed the procedures below. First, we created components and assembly the models in SolidWorks. Second, we identified the materials for each component. Third, we set input force. Fourth, we created mash for each component. Fifth, we ran the system and got results like displacements, factor of safety and stress distribution. The mechanical parameters of 301, 304 and 420 are shown below. These are the materials that applied to build the dual-head fan retractor.

Table A.4: Mechanical parameters of AISI 301, AISI 304 and AISI 420.

	AISI 301	AISI 304	AISI 420
Elastic Modulus	300 MPa	250 MPa	200 MPa
Density	8000 $^{kg}/_{m^3}$	8000 $^{kg}/_{m^3}$	7800 $^{kg}/_{m^3}$
Tensile strength	550 MPa	600 MPa	800 MPa

Hardened AISI 304 is selected to build the tooth clutch as the biggest stress distributed on the tooth clutch. The elongated laminated bar needs to have great elasticity so that heat treated AISI 301 is utilised for fabrication of the elongated laminated bar. The stress analysis is carried out when the dual-head fan retractor is opening, and the retractor showed a hand holding shape. Here, the hand holding shape obtains the load 1.635 *N*.

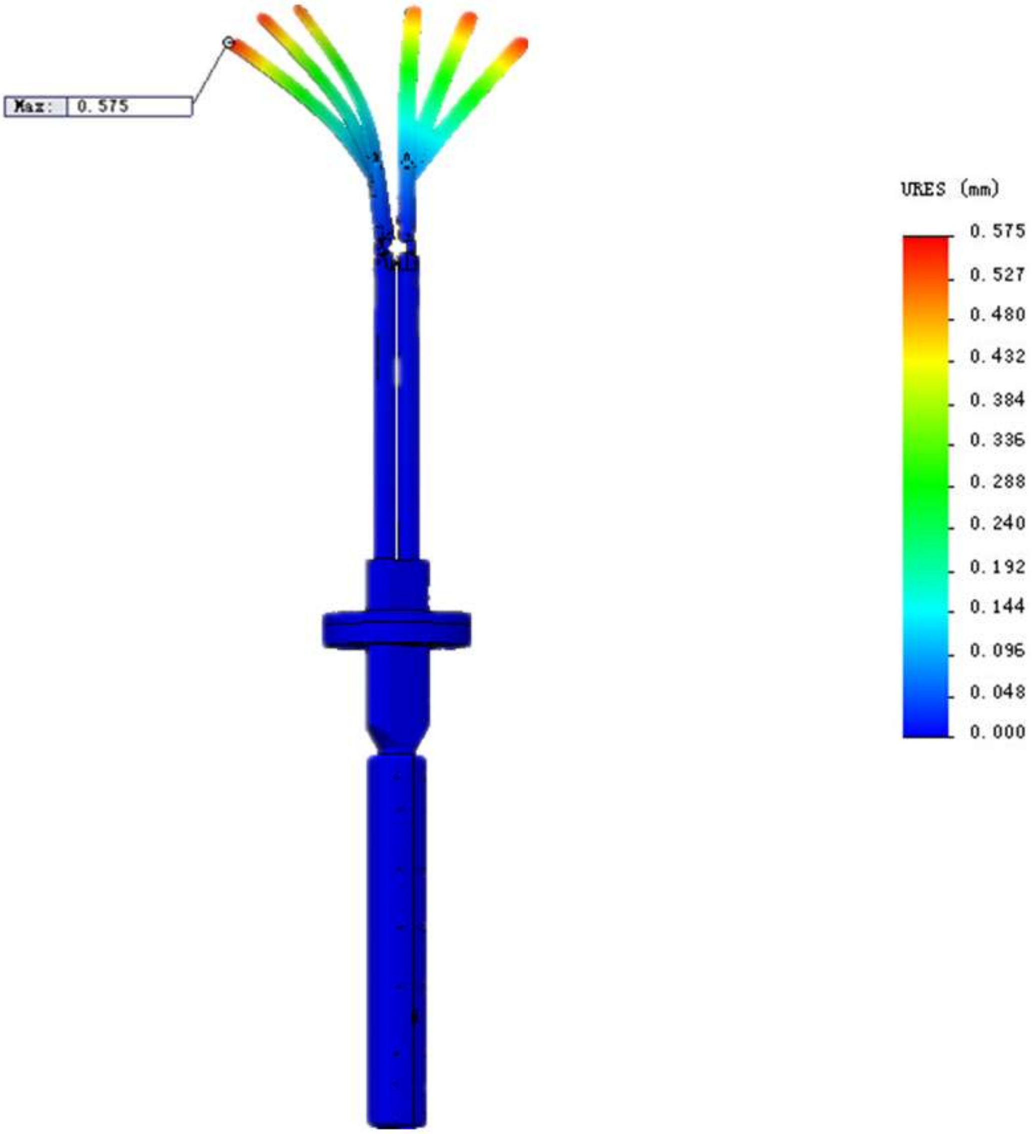

Figure A.5: The dual-head fan retractor showing the displacement.

Displacement is the distance between the initial point and final point. The Figure A.5 shows the displacement of the dual-head fan retractor when load 1.635*N* is placed on the fan blade with the handle fixed. The fan blades are made of AISI 304. The displacement increases with the colour changing from blue to red. The result showed that the maximum displacement is 0.575 mm on the tip of the fan blade.

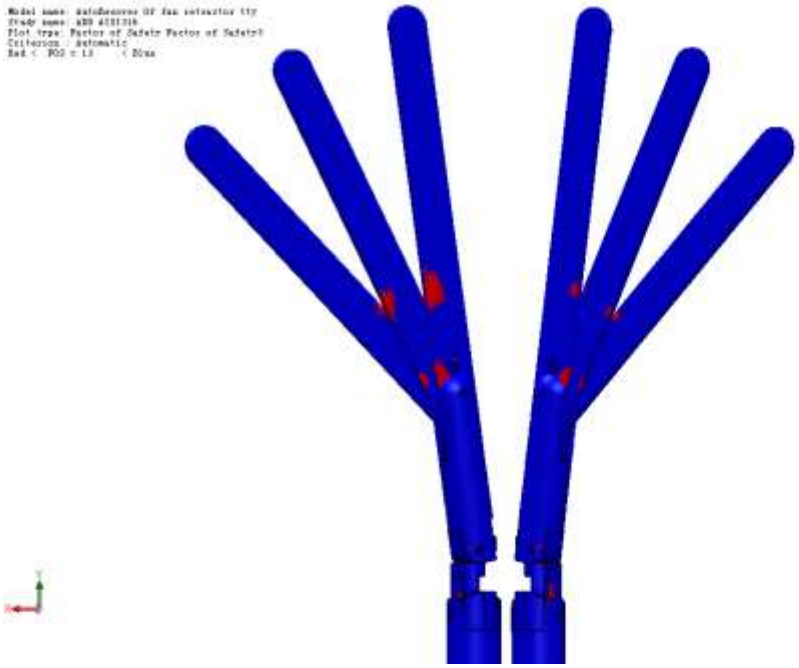

Figure A.6: Factor of safety diagram for the end-effector on the front view.

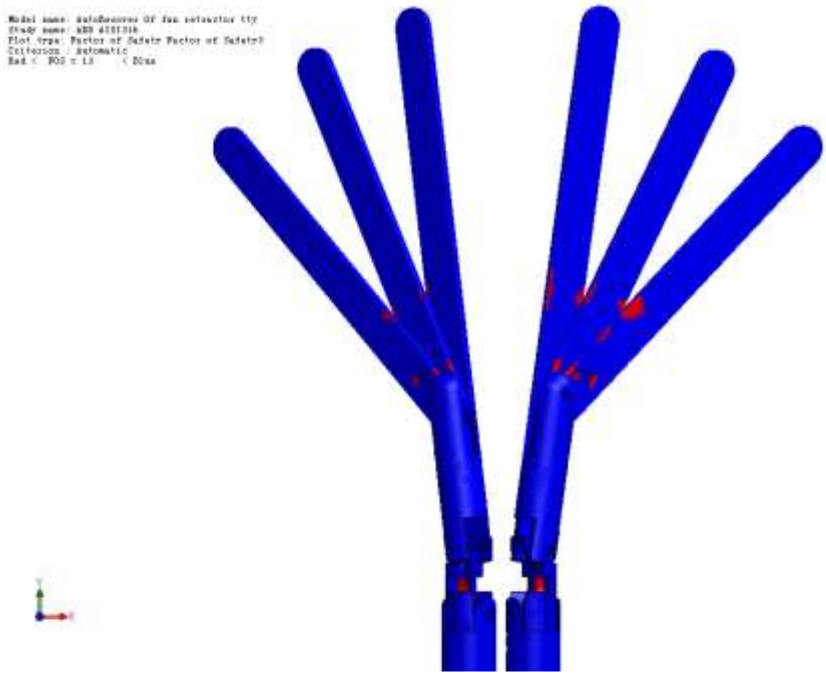

Figure A.7: Factor of safety diagram for the end-effector on the back view.

The factor of safety describes the load carrying capacity of a system beyond an actual load. In Figures A.6 and A.7, the red area is the unsafe regions while the blue area is relatively safe area. The red area of tooth clutch has more danger coefficient than other blue area.

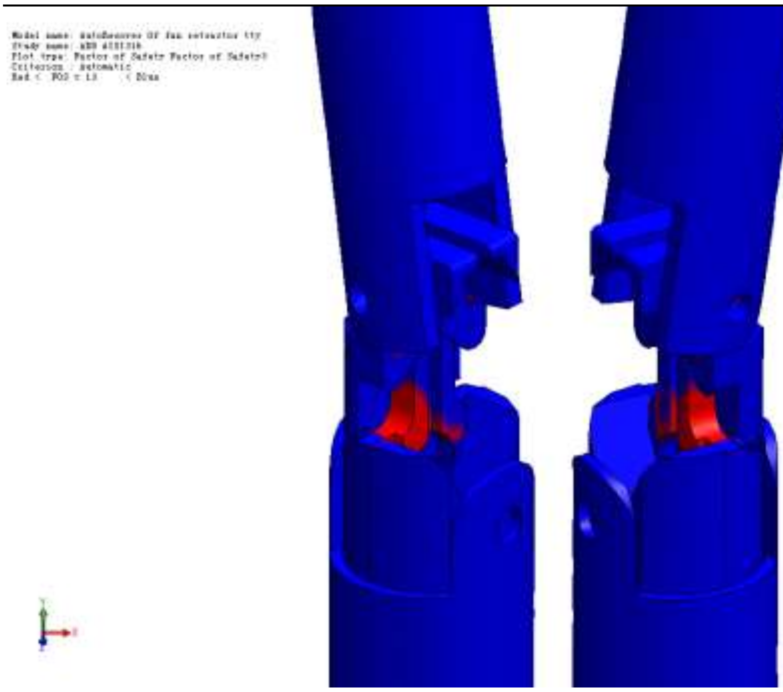

Figure A.8: Factor of safety for the tooth clutch set on the back view.

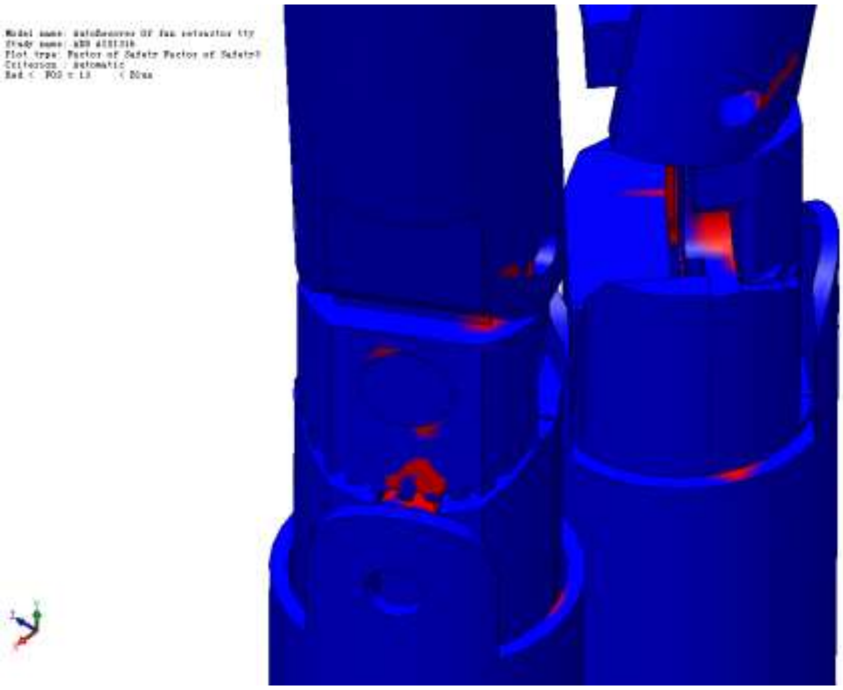

Figure A.9: Factor of safety for the tooth clutch set on the left view.

In Figure A.9, the unsafety area is on the tooth clutch and the front part of the front cover as they were covered by colour red.

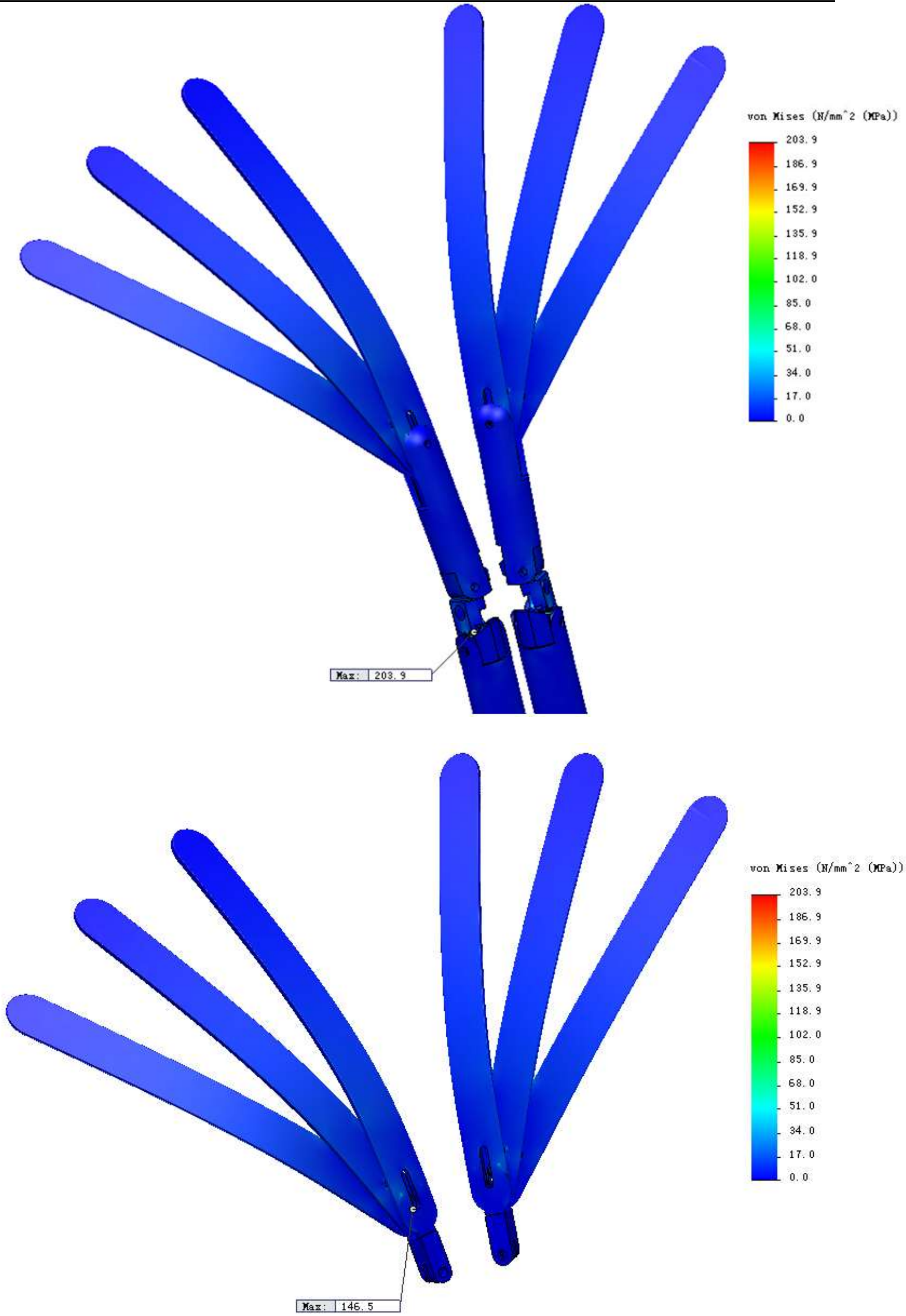

Figure A.10: The stress distribution of the fan blades.

The stress distribution of the fan end-effectors is shown in Figure A.10. The maximum pressure of the whole retractor was on the tooth clutch, which is 203.9 MPa. The maximum stress of the fan blades is 146.5 MPa on the slave blade.

Figure A.11 shows the distribution of the gear set and the palm. It is clear that rest of the gear set and palm are in colour blue. That means these areas are safe. The tooth of the tooth clutch was marked as the maximum pressure point and the pressure is 203.9 MPa.

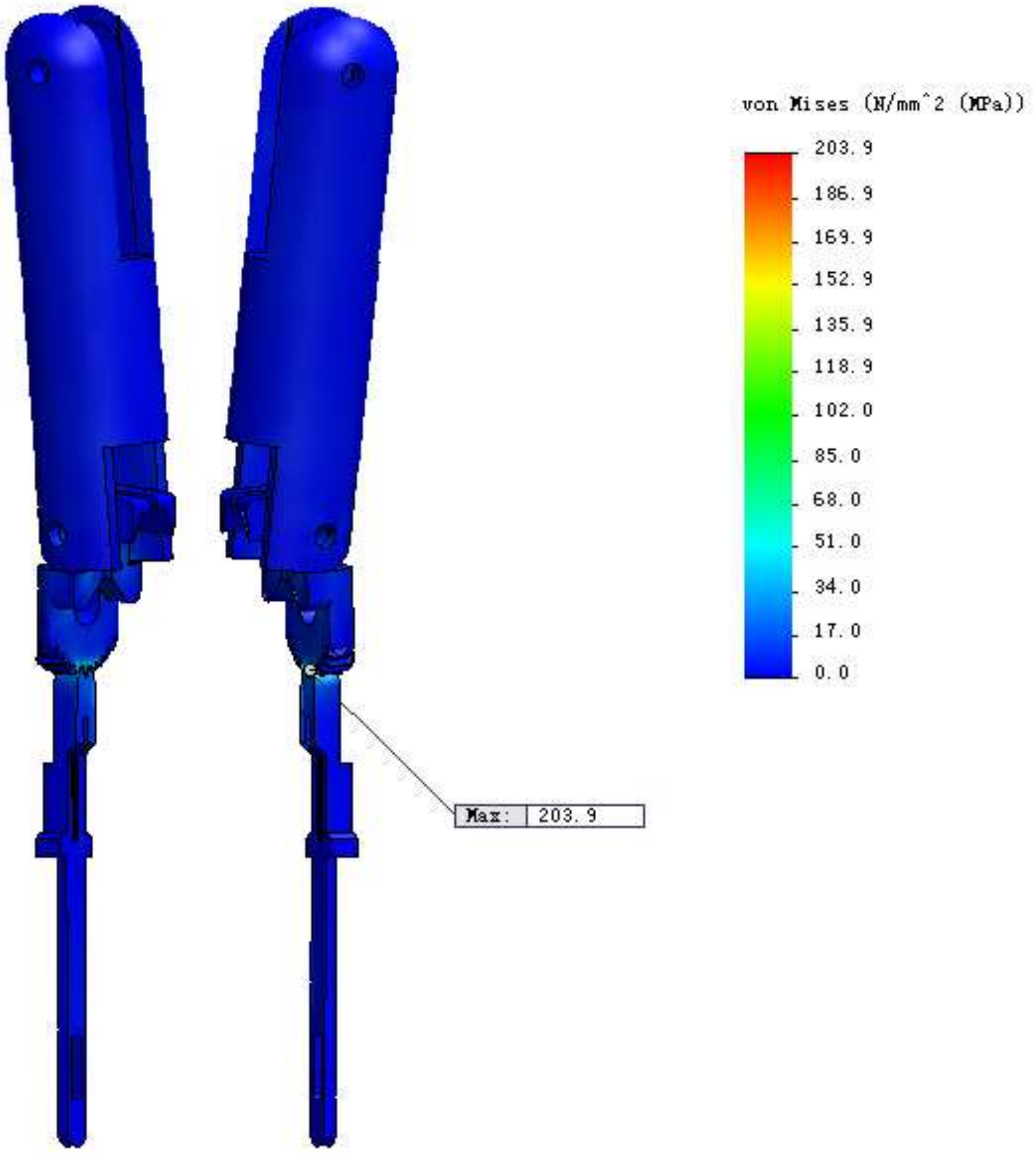

Figure A.11: The stress distribution of the palm, tooth clutch and clutch pedal on the front view.

In Figure A.12, it displays the stress distribution of the gear set and the palm on the left view. The biggest stress on tooth clutch is 203.9 MPa which is smaller than the elastic modulus of the hardened AISI 304, which is 250Mpa. That means tooth clutch is safe when load is 1.635N.

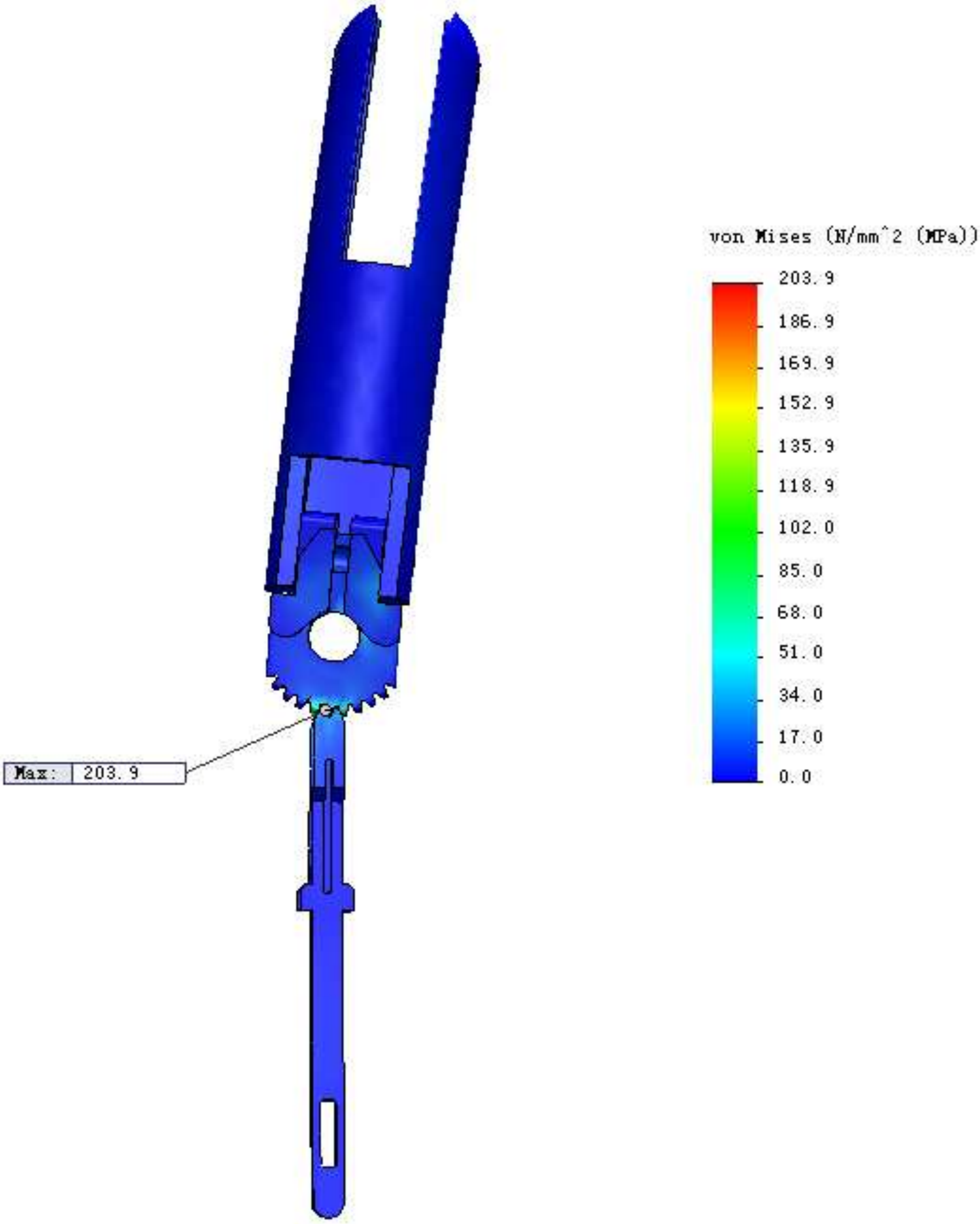

Figure A.12: The stress distribution of the palm, tooth clutch and clutch pedal on left view.

Figure A.13 shows the stress distribution of the tooth clutch and the clutch pedal. The clutch tooth sustains the biggest stress when load 1.635*N* is applied and the maximum stress is 203.9 MPa.

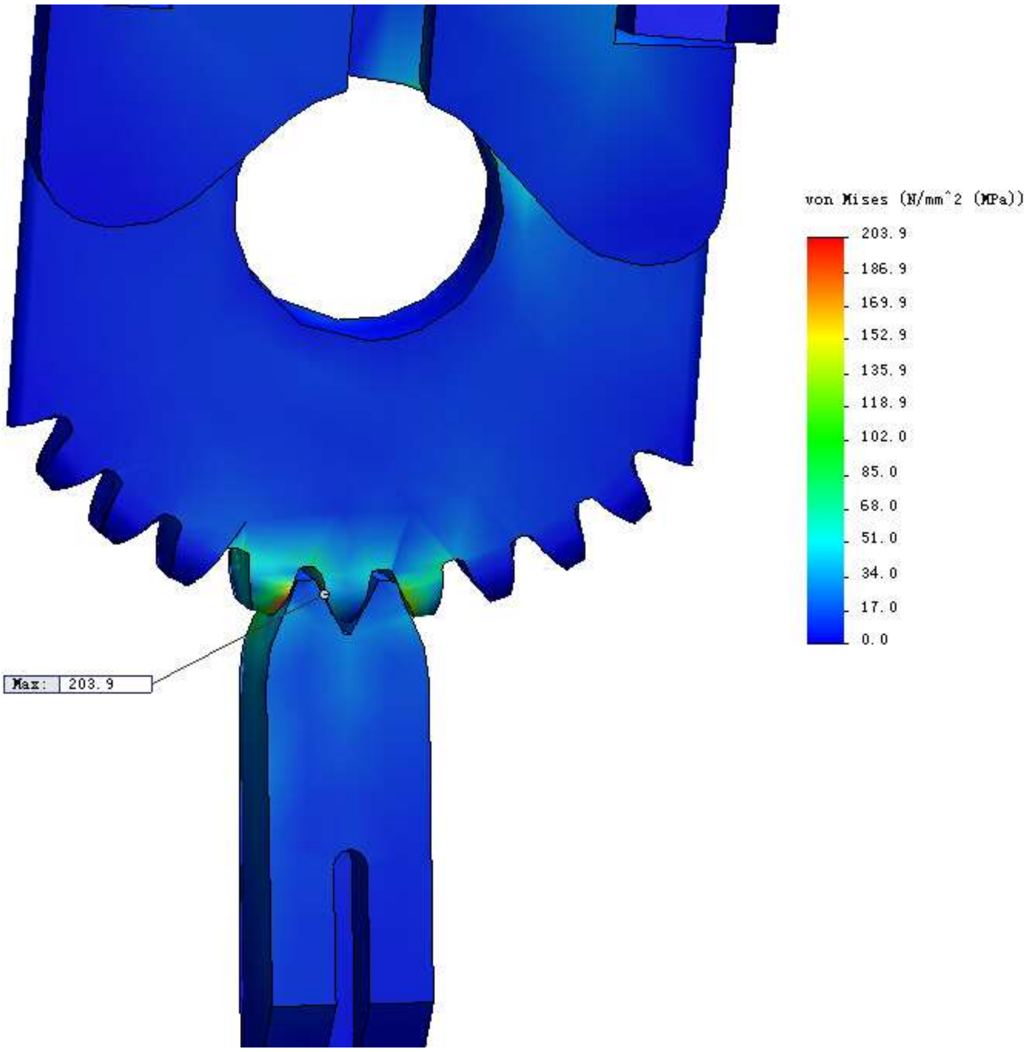

Figure A.13: The stress distribution of the tooth clutch and clutch pedal.

Figure A.14 and Figure A.15 show the stress distribution of the tooth clutch and the front cover. As explained, the biggest stress is on the tooth clutch.

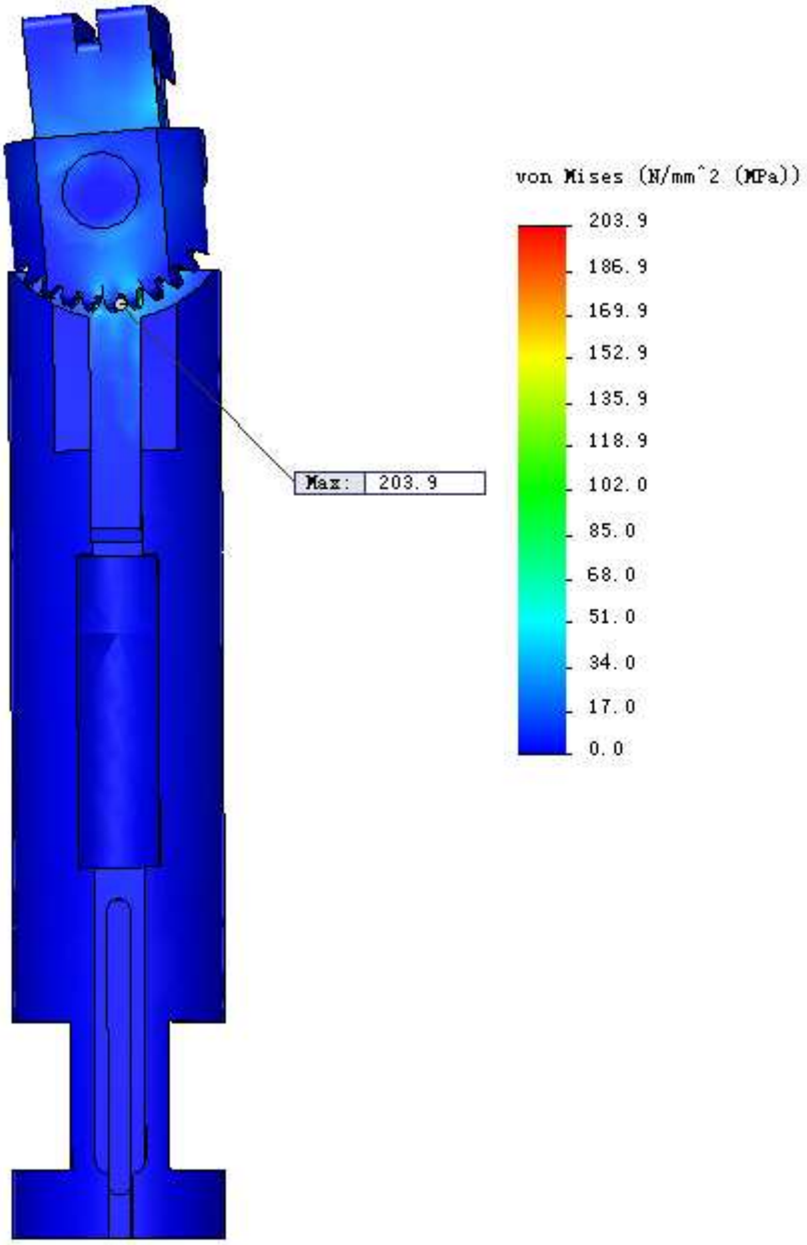

Figure A.14: The stress distribution of the tooth clutch and front cover on the front view.

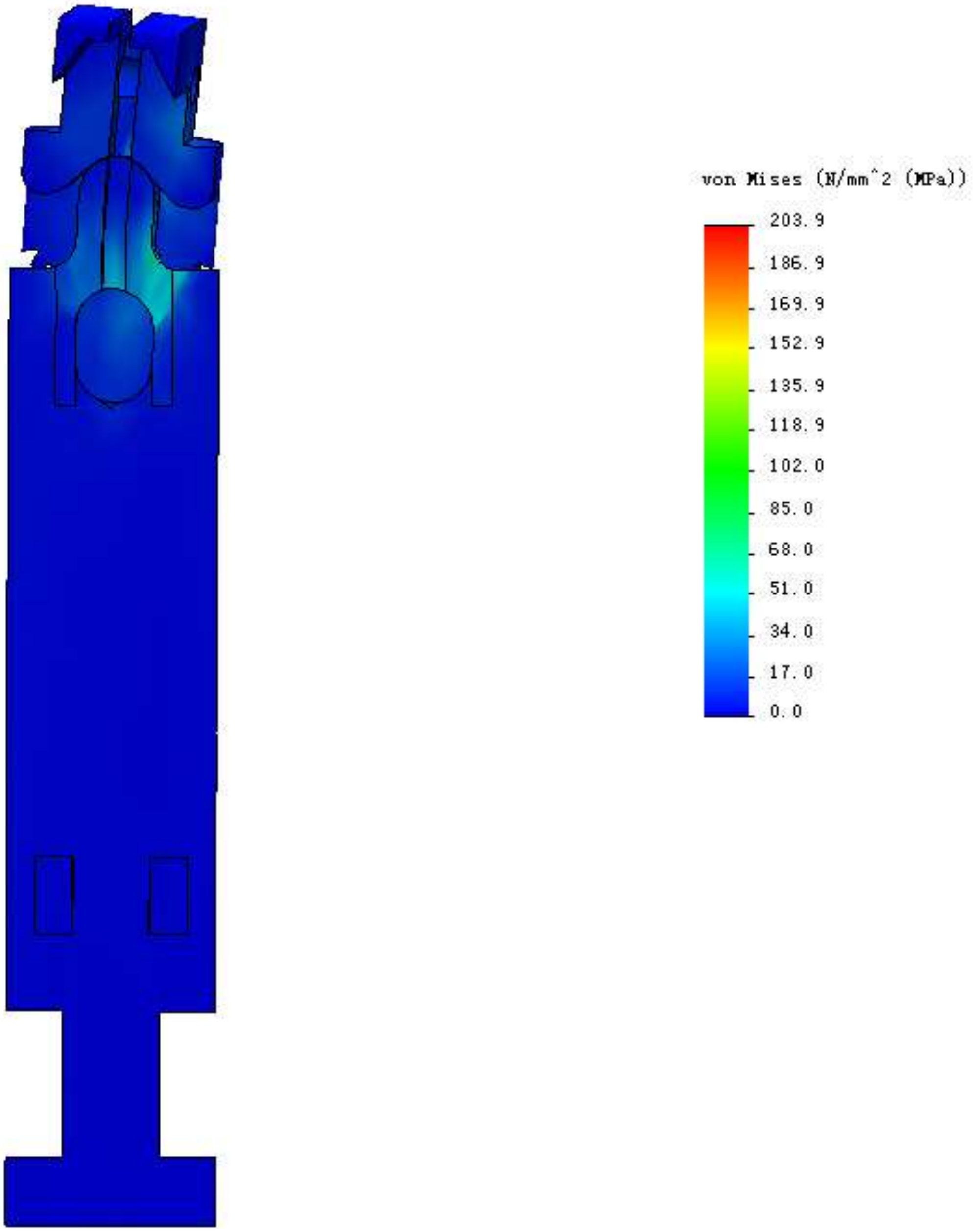

Figure A.15: The stress distribution of the tooth clutch and front cover on the back view.

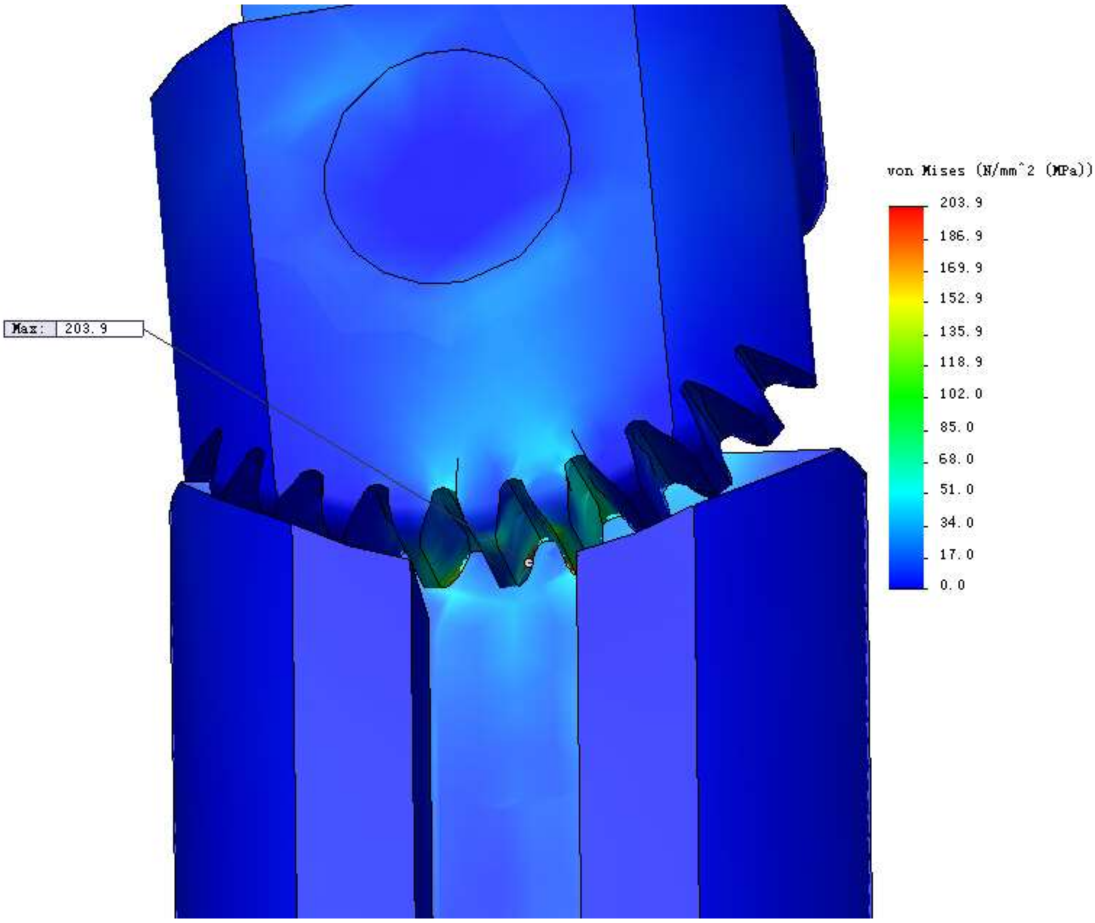

Figure A.16: The amplified diagram of the stress distribution of the tooth clutch and front cover.

The Figure A.16 shows the amplified diagram of the stress distribution. It clearly presents the location of the biggest stress point.

A.4 Components fabrication

In this section, we will discuss the details of fabrication of the 2.5 ratio prototype. The laminated bars were made by heat treated AISI 301 while the other components are created by 3D printer.

A.4.1 Wire electrical discharge machining

For cutting the slots on the laminated bars, a wire electrical discharge machining machine was selected. Wire electrical discharge machining applies molybdenum wire as a tool. When the high-frequency pulse voltage is utilised on the molybdenum wire, the molybdenum wire decomposes and turn to be electro-spark which drill a hole on the metal cut along the metal surface. Vast heat can be produced instantly. The heat is very much high so that partly metal may be gasified.

Figure A.17: HF numerically-controlled processing machine.

The technique procedure can be divided into two steps. First, use molybdenum wire to drill a hole on the metal bar. Second, use the wire electrical discharge machine to cut a slot depending on the drawing.

A.4.2 Normalization for stainless steel laminated bar

The open and collapse joint and front palm rotation all rely on few pieces of 301 stainless steel laminated bar. The 301 stainless steel laminated bar is robust in moving forward and backwards, and also have good elasticity to do the palm rotation. For making the laminated bar, we need seven steps.

1. Stock

Find three pieces 301 stainless steel and ready for processing.

2. Drilling

Drilling three pieces and ready for wire electrical discharge machining.

3. Wire electrical discharge machining

Wire electrical discharge machining depend on the drawing.

4. Grinding

Grind the surface to reach drawing request.

5. Shaping

Shape the laminated bar. Heat the components up to Ac3. Ac3 means to heat the freedom ferrite then transfer all the freedom ferrite to austenite formation. Normally the temperature is from 727℃ to 912℃. Normalise the stainless steel by heating it to a particular temperature. Then, let the material cool down to room temperature. It is a treatment process for making stainless steel softer but keeps the other properties still.

6. Ultrasonic cleaning

Ultrasonic cleaning could help clean the dead angle.

7. Stoving

Stoving can contribute to wiping off water stain.

A.4.3 3D printing

3D printing, also known as additive manufacturing (AM), helps synthesise a three-dimensional product by using various processes. 3D printing machine builds successive layers to form the product which can be any geometry or shape. For fabricating the dual-head fan retractor, some components are made by the 3D printing technique. The 3D printer from Stratasys Ltd. is utilised to build the components.

Figure A.18: Stratasys 3D printer.

A.5 System Integration of the overall Retractor

The integration of the retractor can be divided into three steps. First, integrating the fan devices; second, assembling of the middle body; third, packaging of the handle.

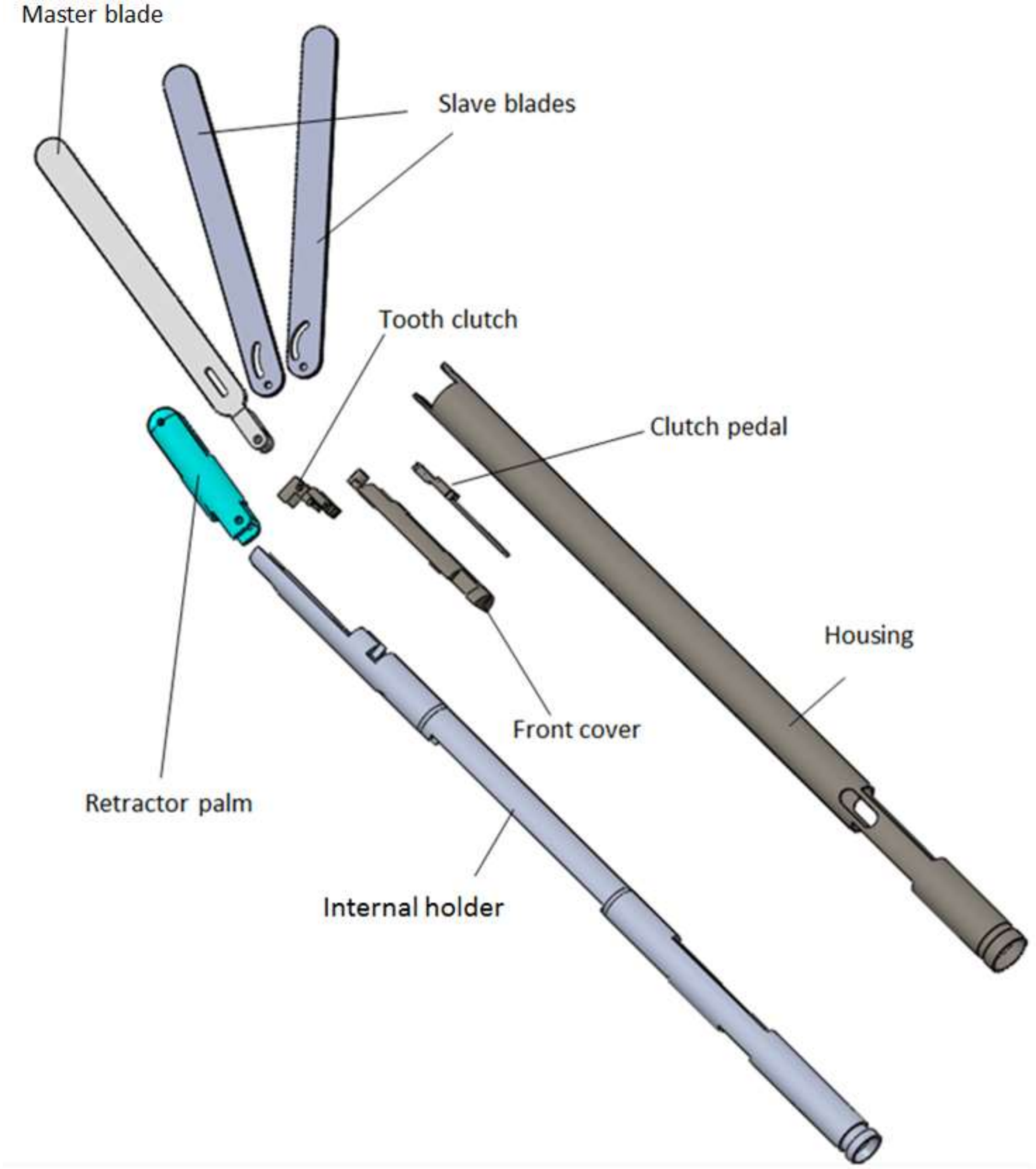

Figur e A.19: Integrating of the fan device.

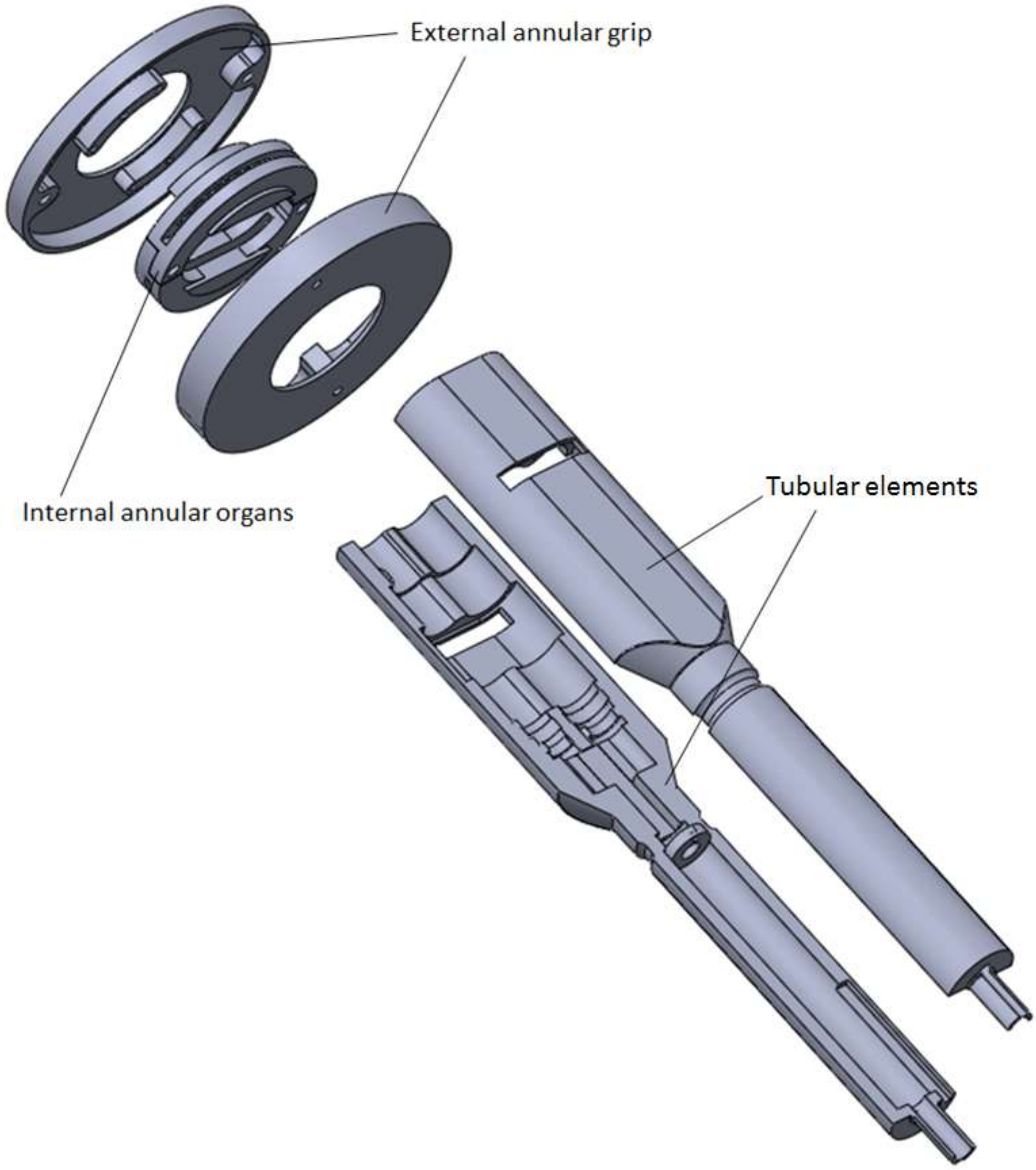

Figure A.20: Assembly of the mid body.

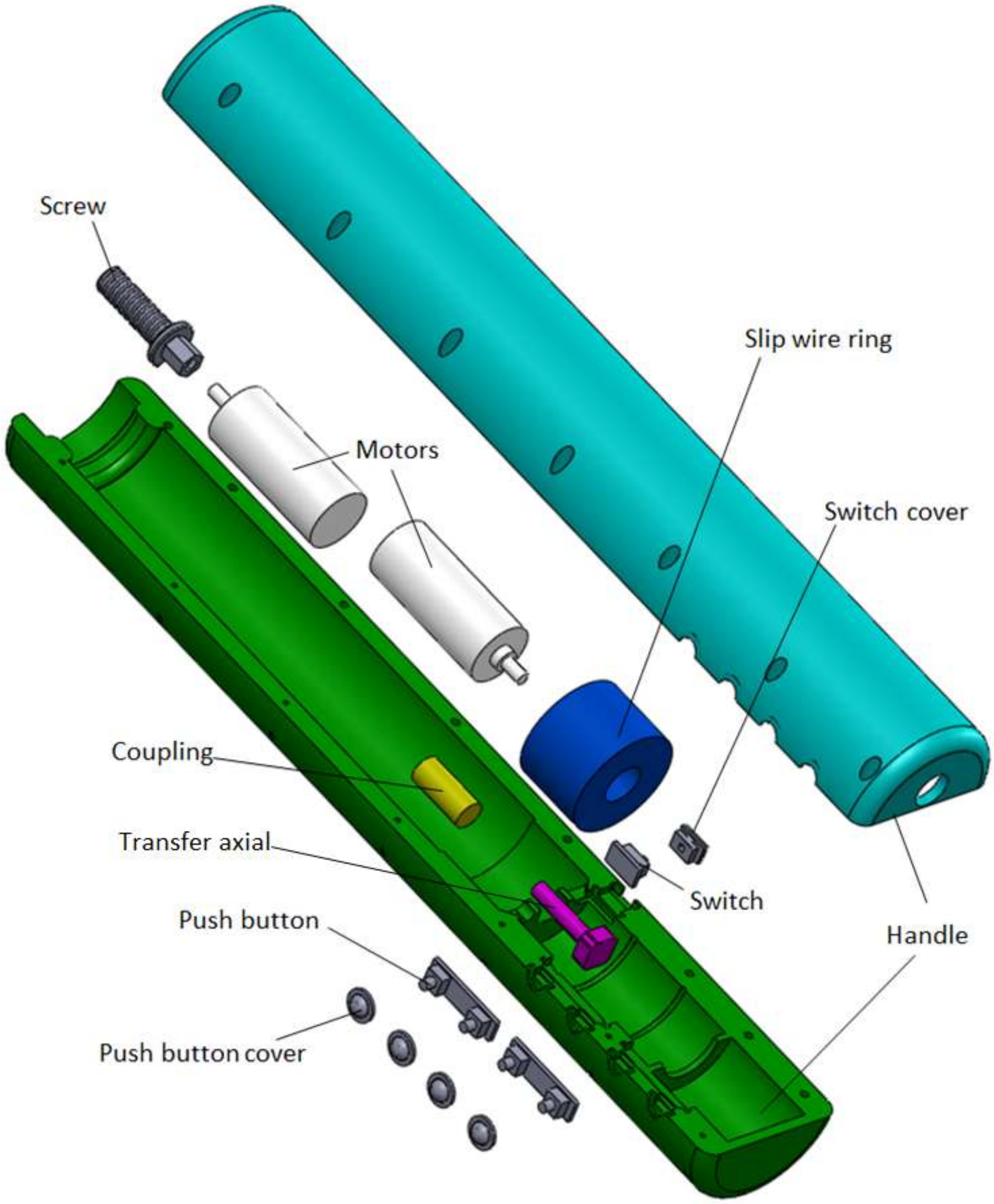

Figure A.21: Packaging of the handle.

Mechanisms are carried out for transferring torque from the motor to the end-effectors. With the help of SolidWorks, results of stress analysis have been generated. For building the control system, the first step is to choose the motors; the second step is to find a capable driver by considering the control logic; the third step is to build the printed control board (PCB) to control a motor driver.

Appendix B

Screw threads

The terms associated with the screw threads are shown in Figure B.1, where the major diameter is the maximum diameter of the screw thread, and minor diameter is the minimum diameter of the screw thread. Here, the pitch diameter is the average of maximum diameter and minimum diameter, while the flank is the straight section of the thread surface which is on either side of the thread. The pitch, measured parallel to the axis plane, is the distance between corresponding points of adjacent screw threads. The crest is the peak edge of the screw thread that reaches the adjacent top flanks while root is the bottom edge of the screw thread that connects the adjacent bottom flanks. The angle formed by the flanks which measured in an axial plane is the thread angle.

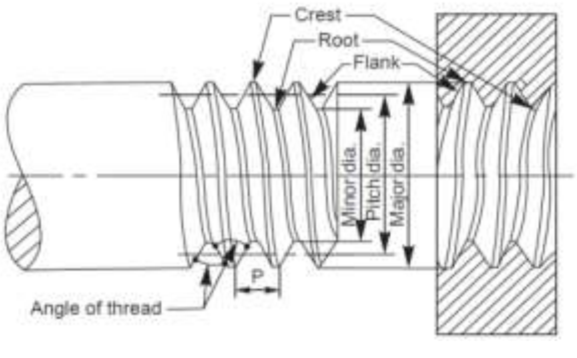

Figure B.1: The terms associated with the screw threads (Larapedia, 2016).

B.1 Square threads

Square threads are commonly used in high duty applications, and the cross-section of the threads appears continuous squares, hence the square threads named after the square geometry. Square threads are the most intrinsically efficient, and they have the lowest friction on account of no radial pressure on the nut, which also extends the nut life, therefore, they are strong enough to carry huge weight. Nevertheless, the fabrication of square thread is difficult, slow and expensive. Although square threads have outstanding efficiency and lowest friction, the thread we are expecting does not have to carry huge weight. The fabrication of square thread is more complicated than the others so that it takes high conversion cost and prolonged time for manufacturing. It’s not the thread that is adopted in the retractor.

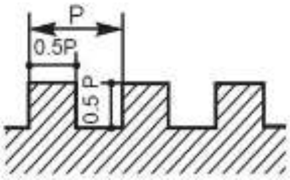

Figure B.2: Cross-section of a square thread (Larapedia, 2016).

B.2 Buttress threads

Buttress threads, also known as breech-lock threads, compose two different types of thread profiles. The thread triangle is scalene, half of the buttress thread flank exhibits lead-screw and the other half flank is a type of hydraulic sealing thread forms. The load-bearing thread flank is perpendicular to the screw axis or slightly slants, but usually the slant angle goes no greater than 7˚, while the other flank slants to 45˚. The load-bearing threads, also called resulting threads, have the same diminutive friction feature as square threads and possess around twice the shearing strength because of the long thread base. Buttress threads typically applied in artillery, especially in the screw type breechblock, while they are utilised in the construction of vice as large power transmission takes place in only one orientation. Regarding the function of the buttress threads, it is not the thread design for the retractor.

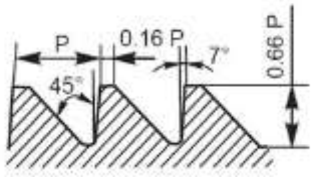

Figure B.3: Cross-section of a buttress thread (Larapedia, 2016).

B.3 V-thread

V-thread gets its name from the letter V isosceles triangle profile. A V-thread without truncation is known as a sharp V-thread. Theoretically, V-threads designed to keep the fastener from loosening. Hence, it works efficiently for linear positioning. This thread induces more frictional resistance when moving the large contact surface so that V-threads are inappropriate for the use of lead-screws. Concerning the above reason, the V-thread is not the design we are searching.

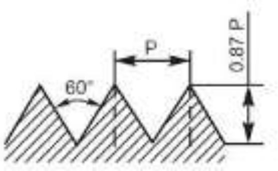

Figure B.4: Cross-section of a V-thread (Larapedia, 2016).

B.4 B.S.W thread

British standard whit worth (B.S.W) thread can trace its root back to the Victorian age. It was called Whitworth thread as well. The B.S.W thread has round ends which make the thread stronger than the sharp V-thread. The pitch value of the thread increases with the core diameter by steps. However, because B.S.W thread is hard for manufacturing, it is not suitable for the retractor.

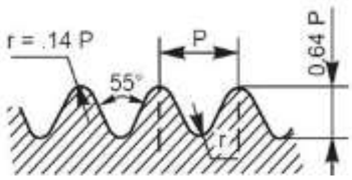

Figure B.5: Cross-section of a B.S.W thread (Larapedia, 2016).

B.5 Trapezoidal threads

Trapezoidal threads, have screw thread profiles with trapezoidal outlines, are known for powerful lead-screw as their high strength and easy machining. The premier trapezoidal thread form is the **Acme thread** form which has a 29˚ thread angle with a thread height half of the pitch. The Acme tooth is more robust than a comparably sized square thread due to the wider base. Acme threads are more prevalent than the other trapezoidal screw threads as the tooling for Acme threads is more dominant. Because of the advantages above, the screw thread and the dual-headed slider are designed regarding Acme thread regulation.

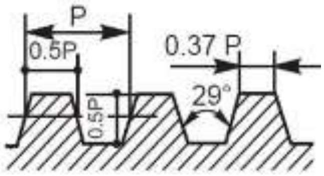

Figure B.6: Cross-section of an Acme thread (Larapedia, 2016).

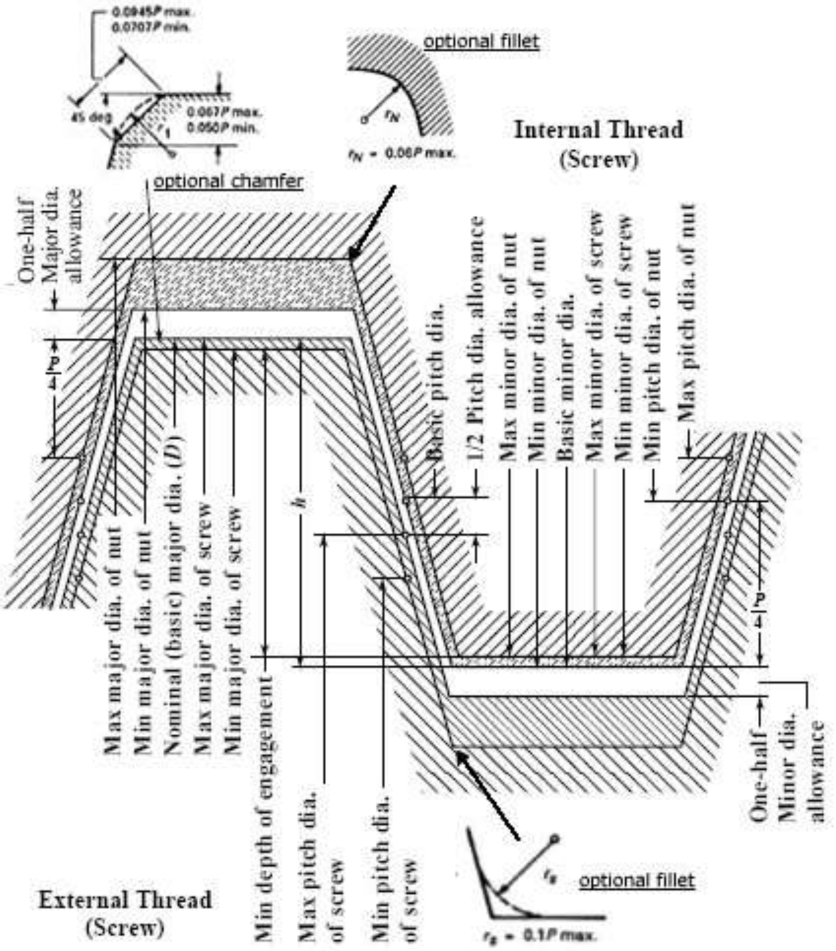

Figure B.7: The Acme thread regulation(Oberg 2012).

Table B.1: List of the equations of the Acme regulation(Engineers 1997).

Parameter/Condition	Symbol	Equation
Pitch	P	$P = \frac{1}{n}$
Basic Pitch Diameter	D_2	$D_2 = D - 0.5P$
Basic Minor Diameter	D_1	$D_1 = D - P$
Thickness at Pitch Line	t	$t = \frac{P}{2}$
Basic Height of Thread	h	$h = \frac{P}{2}$

Basic Flat at Crest (internal thread)	F_{cn}	$F_{cn} = 0.3707P$
Basic Flat at Crest (external thread)	F_{cs}	$F_{cs} = 0.3707P - 0.259\times(PDAET)$
Basic Flat at Root (internal thread)	F_{rn}	$F_{rn} = 0.3707P - 0.259\times(MDAIT)$
Basic Flat at Root (external thread)	F_{rs}	$F_{rs} = 0.3707P$ $-0.259\times(MDAET - PDAET)$
Minimum Stress Area	A_t	$A_t = 3.1416(\frac{d_{1\,min} + d_{2\,min}}{4})^2$
Minimum Shear Area Per Unit Length	A_s	$A_s = 3.1416 \cdot D_{1\,max}(0.5 + n \cdot \tan(14.5^{\circ})\ (d_{2min}$ $- D_{1\,max}))$

Appendix C

Motor selection and control

C.1 Motor selection

The dual-head fan retractor is a fine surgical instrument. For fitting the small size and a relatively bigger torque, two gear DC motor sets have been chosen for torque transferring.

C.2 Gear motors

JGA20-130 from Aslong Ltd. is selected. The chart below shows the parameters of different types of JGA20-130.

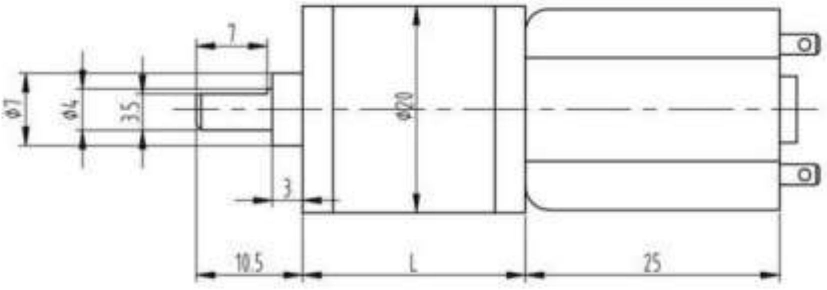

Figure C.1: Drawing of the gear motor.

Table C.1: Parameters of the gear motor.

Voltage		No Load		Load Torque				Stall		L	Reducer	Weight
Workable Range	Rated Voltage	Speed	current	speed	current	Torque	Output	Torque	Current	Size	Ratio	Weight
V	V	rpm	mA	Rpm	mA	N • m	W	N • m	A	mm	1:00	g
3-9V	6	288	60	221	200	0.25	1.1	1.25	930	16	25	80
3-9V	6	144	60	110	200	0.5	1.1	2.5	930	17.5	50	80

3-9V	6	72	60	55	200	1	1.1	5	930	19	100	80
3-9V	6	36	60	28	190	1.95	1.1	9.7	930	19	195	80
3-9V	6	28	60	22	190	2.5	1.1	Forbidden	930	19	250	80
3-9V	6	15	60	11	190	4.8	1.1	Forbidden	930	20.5	488	80
9-18V	12	240	56	185	100	0.2	0.8	1	400	16	25	80
9-18V	12	120	56	92	100	0.4	0.8	2	400	17.5	50	80
9-18V	12	60	56	46	100	0.8	0.8	4	400	19	100	80
9-18V	12	30	56	23	100	1.56	0.8	7.8	400	19	195	80
9-18V	12	24	56	18	100	2	0.8	10	400	19	250	80
9-18V	12	12	56	9.5	100	4	0.8	Forbidden	400	20.5	488	80

The ‘Forbidden’ in Table C.1 means that stalling in the motor is prohibited.

It is well known that the human safe voltage is 6V to 36V. A 6V gear motor is chosen in this project. The rolling speed is desired to be slow because fast speed may cause irretrievable mistakes like damage the internal organs. JGA20-130 contains a 4.8 Nm load torque gear motor, which is suitable for the dual-head fan retractor. In these cases, JGA20-130-6V-15RPM is selected for fabricating the dual-head fan retractor.

C.3 DC motor basic theory

The gear motor is assembled by a DC motor and a gear box. Motor rotational speed formula is shown below,

$$n = (U - IR)/C_e\emptyset \tag{C.1}$$

Here, *n* is the rotational speed, *U* is the working voltage of the gear motor, *I* is the motor current, *R* is the resistance of the gear motor and *CeØ* is the electromotive force (EMF).

The torque formula is below,

$$M = C_m I \tag{C.2}$$

Here, *M* notes the value of motor toque, C_m is torque factor and *I* is electronic current.

The induction armature voltage is below,

$$E = C_e \emptyset n \tag{C.3}$$

E is induction armature voltage, C_e is electromechanical coupling factor, $\emptyset$ is magnetic flux, n is motor rotational speed.

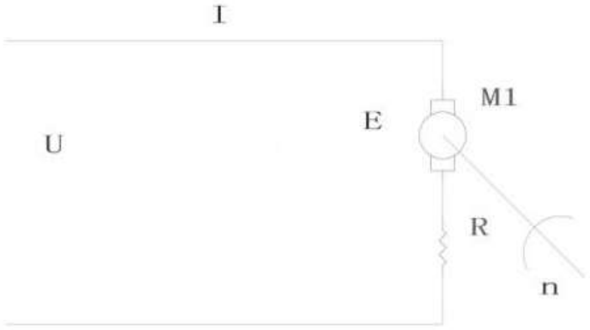

Figure C.2: Diagram of gear motor.

In the figure above, it shows the control theory of a DC motor. Here, U is the working voltage, I is the working current, E is the induction armature voltage, R is the internal resistance of DC motor and n is rotational speed.

C.4 Motor rotational methods

To make the motor spin forwards and backwards, an H-bridge circuit is utilised. In Figure C.3 shown below, four metallic oxide semiconductor field effect transistor (MOSFET) are included in a driver for controlling the spin movements.

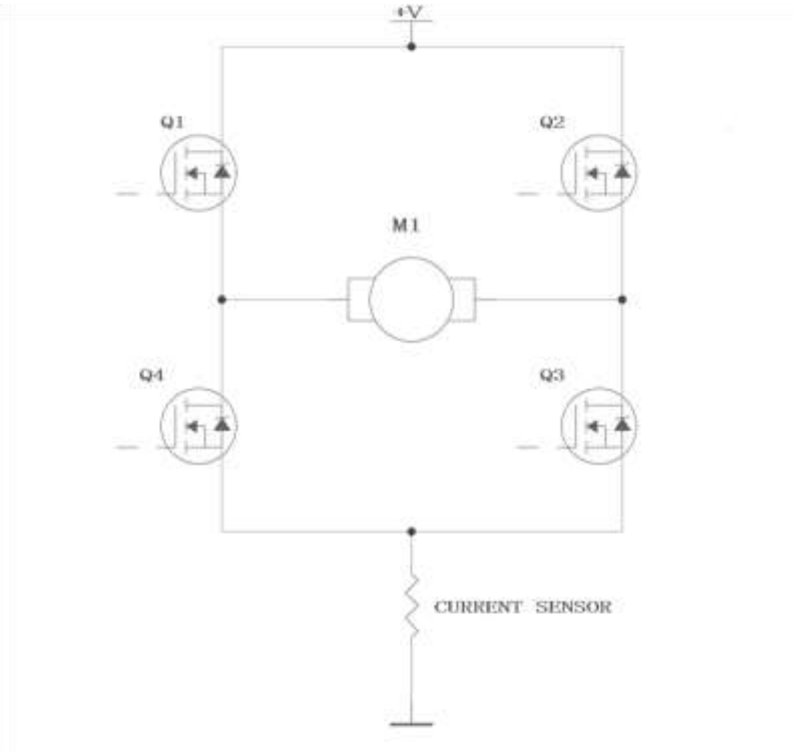

Figure C.3: Diagram of H-bridge

In the figure above, Q1, Q2, Q3 and Q4 are MOSFETs. The motor does the forwards spin when odd numbers are switched on. The motor does the reverse spin when even numbers are switched on. There is a current sensor before the major loop reaching the ground. The current sensor measures the current of the motor. To make the forwards and reversal rotations, choosing a capable motor driver is essential.

C.5 Circuit schematic

In terms of the functional diagram of the DRV8801, the circuit schematic is built as below.

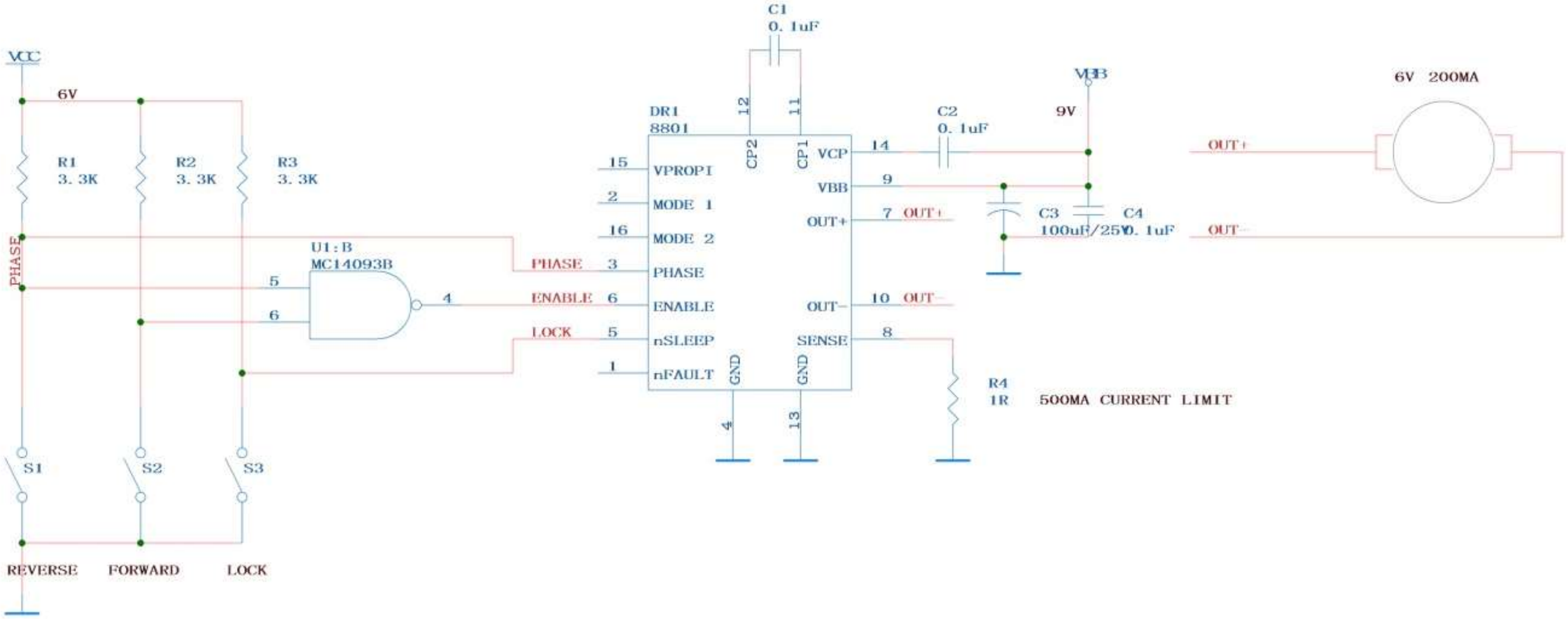

LOCK	ENABLE	PHASE	MOTOE DIRECTION
1	1	1	FORWARD
1	1	0	REVERSE
1	0	X	STOP
0	X	X	SLEEP

Figure C.4: The circuit schematic.

The S1, S2 are push buttons. The S3 is slide switch. U1 is a NAND gate. DR1 is DRV8801 integrated circuits (IC). Switch on S3, nSLEEP is low potential. No matter what potential are S1 and S2, the motor doesn't rotate. Switch off S3, pin LOCK is a high potential, so that it's ready for forward and reverse rotation. Then, switch on S2, switch off S1, PHASE pin is low potential while ENABLE pin is a high potential. The motor does a clockwise rotation. When switching on S1 and switching off S2, PHASE pin is high potential while ENABLE pin is a high potential. The motor does an anti-clockwise rotation.

C.6 Design of printed circuit boards

For building the printed circuit boards (PCB), the first step is to draw the circuit schematic; second, numbering the components; third, draw the PCB on EDA2000. The figure below shows a push button utilised in this project as buttons S1, S2 and S3.

Figure C.5: Push button S1,S2 and its PCB.

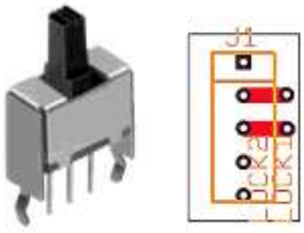

Figure C.6: Switch button S3 and its PCB.

The other element components are settled on the PCB below.

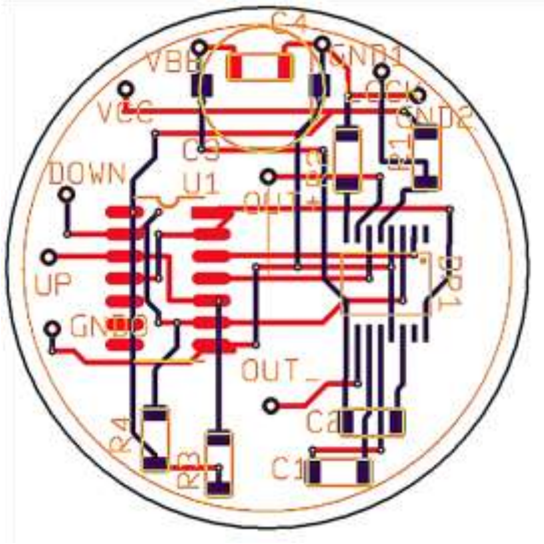

Figure C.7: Main PCB.

The three PCBs connected in terms of the functional circuit diagram, and helps logically control the circuit. All the PCBs are made depend on the dimension of components.

C.7 Motor driver DRV8801

In this report, the motor driver DRV8801(Texas Instrument Ltd., 2015) designed by Texas Instrument Ltd is selected to drive the gear motor JGA20-130. DRV8801 motor driver has multiple features, for example,

1. Low ON-Resistance output
2. Over current protection
3. Motor lead short-to-supply protection
4. Short-to-ground protection
5. Low-power mode
6. Synchronous rectification
7. Diagnostic output
8. Internal under voltage lockout(UVLO)
9. Crossover-current protection
10. 16-pin QFN with powerPAD^{TM} package

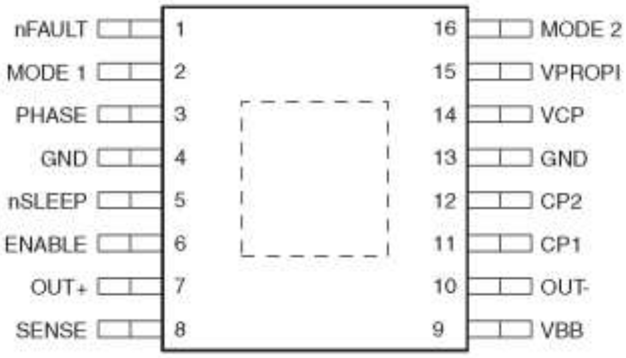

Figure C.8: Diagram of DRV8801.

The DRV8801 PWP package top view above notes the functional name of 16-pin outputs. Below are the details for the terminal functions.

Table C.2: Table of pin function.

Terminal		Description
No.	DRV8801	
1	nFAULT	Fault open-drain output
2	MODE1	Mode logic input
3	PHASE	Logic input for direction control
4	GND	Ground
5	nSLEEP	Sleep logic input
6	ENABLE	Enable logic input
7	OUT+	DMOS full-bridge output positive
8	SENSE	Sense power return
9	VBB	Load supply voltage
10	OUT-	DMOS full-bridge output negative
11	CP1	Charge-pump capacitor 1
12	CP2	Charge-pump capacitor 2
13	GND	Ground

14	VCP	Reservoir capacitor
15	VPROPI	Winding current proportional voltage output
16	MODE2	Mode 2 logic input
	PowerPAD	Exposed pad for thermal dissipation connect to GND pins

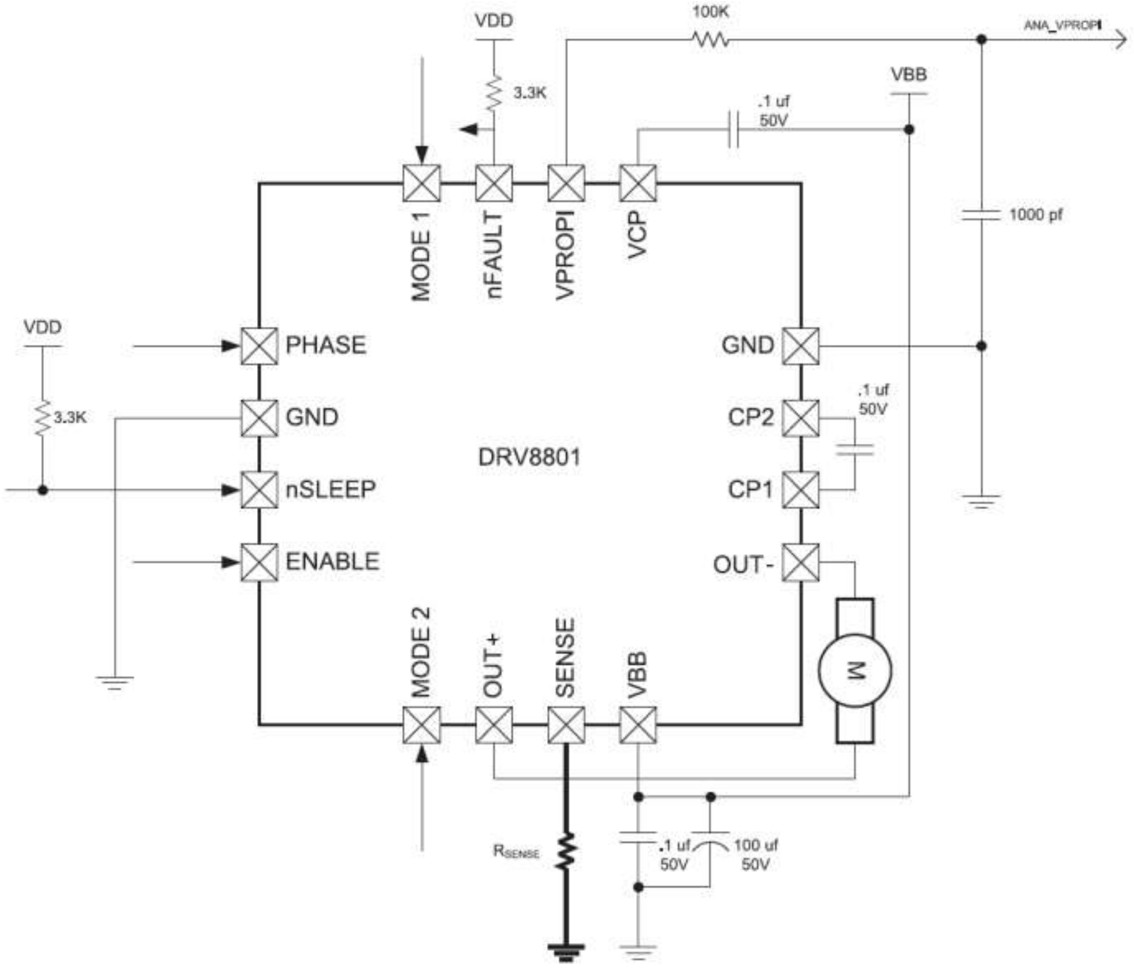

Figure C.9: Application diagram of DRV8801.

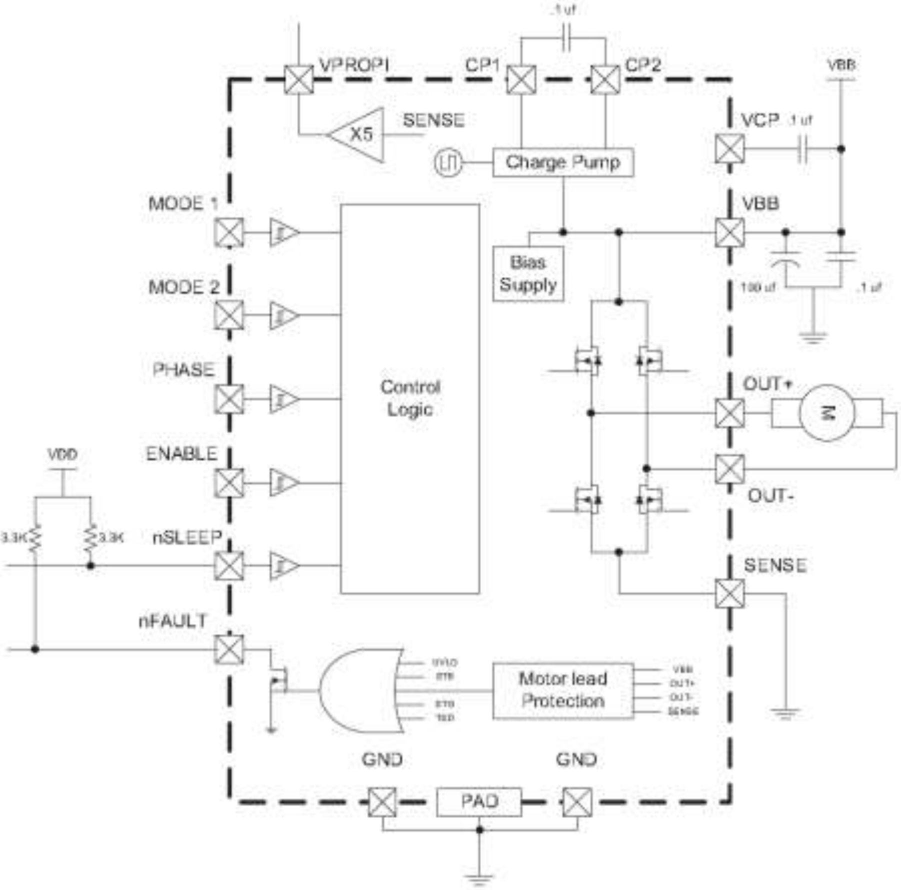

Figure C.10: Function block of DRV8801.

Table C.3: Control logic table.

PINS							OPERATION
PHASE	ENABLE	MODE1	MODE2	nSLEEP	OUT+	OUT-	
1	1	X	X	1	H	L	Forward
0	1	X	X	1	L	H	Reverse
X	0	1	0	1	L	L	Brake(Slow decay)
1	0	0	1	1	L	H	Fast-decay synchronous
0	0	0	X	1	H	L	Fast-decay synchronous
X	X	X	X	0	Z	Z	Sleep mode

Here, X=don’t care, Z= high impedance

To prevent reversal of current during fast-decay synchronous rectification, outputs go to the high-impedance state as the current approaches 0 A.

Reference

Abramowitz, M., & Stegun, C. A. (1972). § 23.1: Bernoulli and Euler Polynomials and the Euler-Maclaurin Formula. *Handbook of Mathematical Functions with Formulas, Graphs, and Mathematical Tables*, 804–806.

Alpers, D. H., Kalloo, A. N., Kaplowitz, N., Owyang, C., Powell, D. W., & Yamada, T. (2011). *Principles of clinical gastroenterology*. John Wiley & Sons.

Anaheim Automation.(2016) Linear Actuator Guide.[Online] Available from: http://www.anaheimautomation.com/manuals/forms/linear-actuator-guide.php#sthash.dLxoWbWk.n1jIgSUR.dpbs

Anthea, M., Hopkins, J., McLaughlin, C. W., Johnson, S., Warner, M. Q., LaHart, D., & Wright, J. D. (1993). Human biology and health. *Englewood Cliffs, New Jersey, USA*, 71–76.

Astin, M., Griffin, T., Neal, R. D., Rose, P., & Hamilton, W. (2011). The diagnostic value of symptoms for colorectal cancer in primary care: a systematic review. *Br J Gen Pract*, *61*(586), e231–e243.

Azenha, A., & Machado, J. A. T. (1997). Dynamic analysis in variable structure position/force hybrid control of manipulators. In *Systems, Man, and Cybernetics, 1997. Computational Cybernetics and Simulation., 1997 IEEE International Conference on* (Vol. 5, pp. 4309–4314). IEEE.

Bassi, E., Benzi, F., Capisani, L. M., Cuppone, D., & Ferrara, A. (2009). Hybrid position/force sliding mode control of a class of robotic manipulators. In *Decision and Control, 2009 held jointly with the 2009 28th Chinese Control Conference. CDC/CCC 2009. Proceedings of the 48th IEEE Conference on* (pp. 2966–2971). IEEE.

Bechlioulis, C., Doulgeri, Z., & Rovithakis, G. (2009). Robot force/position tracking with guaranteed prescribed performance. In *Robotics and Automation, 2009. ICRA'09. IEEE International Conference on* (pp. 3688–3693). IEEE.

Boltyanskii, V. G., Gamkrelidze, R. V, & Pontryagin, L. S. (1956). Towards a theory of optimal processes, Reports Acad. *Sci. USSR*, *110*(1), 710.

Boltyanskiy, V. G., Gamkrelidze, R. V, MISHCHENKO, Y. E. F., & Pontryagin, L. S. (1962). Mathematical theory of optimal processes.

Botden, S. M. B. I., Torab, F., Buzink, S. N., & Jakimowicz, J. J. (2008). The importance of haptic feedback in laparoscopic suturing training and the additive value of virtual reality simulation. *Surgical Endoscopy*, *22*(5), 1214–1222.

Bryson, A. E. (1975). *Applied optimal control: optimization, estimation and control*. CRC Press.

Buunen, M., Veldkamp, R., Hop, W. C., Kuhry, E., Jeekel, J., Haglind, E., … Morino, M. (2009). Colon Cancer Laparoscopic or Open Resection Study Group: Survival after laparoscopic surgery versus open surgery for colon cancer: long-term outcome of a randomised clinical trial. *Lancet Oncol*, *10*(1), 44–52.

Caccavale, F., Chiacchio, P., Marino, A., & Villani, L. (2008). Six-DOF impedance control of dual-arm cooperative manipulators. *Mechatronics, IEEE/ASME Transactions on*, *13*(5), 576–586.

Cannon, R. M., Scoggins, C. R., Callender, G. G., McMasters, K. M., & Martin, R. C. G. (2012). Laparoscopic versus open resection of hepatic colorectal metastases. *Surgery*, *152*(4), 567–574.

Chan, S. P., Yao, B., Gao, W. B., & Cheng, M. (1991). Robust impedance control of robot manipulators. *International Journal of Robotics & Automation*, *6*(4), 220–227.

Chang, P. H., & Jin, M. (2006). Nonlinear Target Impedance Design and Its Use in Robot Compliant Motion Control with Time Delay Estimation. In *IEEE Industrial Electronics, IECON 2006-32nd Annual Conference on* (pp. 161–166). IEEE.

Chen, H., Wang, J., Zhang, G., Fuhlbrigge, T., & Kock, S. (2009). High-precision assembly automation based on robot compliance. *The International Journal of Advanced Manufacturing Technology*, *45*(9-10), 999–1006.

Chen, H., & Xiao, J. (2011). Robust compliant assembly automation using an industrial robot. In *2011 6th IEEE Conference on Industrial Electronics and Applications* (pp. 1161–1166). IEEE.

Christian, S. C. (1998, March 3). Laparoscopic retractor having a plurality of blades extending laterally from a handle. *Google Patents.* Retrieved from http://www.google.tl/patents/US5722935

Craig, J. J. (2005). *Introduction to robotics: mechanics and control* (Vol. 3). Pearson Prentice Hall Upper Saddle River.

Craig, J. J., & Raibert, M. H. (1979). A systematic method of hybrid position/force control of a manipulator. In *Computer Software and Applications Conference,* *1979. Proceedings. COMPSAC 79. The IEEE Computer Society's Third International* (pp. 446–451). IEEE.

Cui, Y., & Sarkar, N. (2001). A unified force control approach to autonomous underwater manipulation. *Robotica*, *19*(03), 255–266.

Cummings, L. C., Delaney, C. P., & Cooper, G. S. (2012). Laparoscopic versus open colectomy for colon cancer in an older population: a cohort study. *World Journal of Surgical Oncology*, *10*(1), 1.

Cuschieri et al.(2004, March 16). Retractor for use in endoscopic surgery and medical instrument for introducing a retractor and method for the use of a retractor in endoscopic surgery. Google patents. Retrieved from https://www.google.ch/patents/US6705989

Dadebo, S. A., McAuley, K. B., & McLellan, P. J. (1998). On the computation of optimal singular and bang–bang controls. *Optimal Control Applications and Methods*, *19*(4), 287–297.

Delaney, C. P., Chang, E., Senagore, A. J., & Broder, M. (2008). Clinical outcomes and resource utilization associated with laparoscopic and open colectomy using a large national database. *Annals of Surgery*, *247*(5), 819–824.

Denavit, J. (1955). A kinematic notation for lower-pair mechanisms based on matrices. *Trans. of the ASME. Journal of Applied Mechanics*, *22*, 215–221.

Dutta, A., & Obinata, G. (2002). Impedance control of a robotic gripper for cooperation with humans. *Control Engineering Practice*, *10*(4), 379–389.

Edwards, B. K., Ward, E., Kohler, B. A., Eheman, C., Zauber, A. G., Anderson, R. N., … Seeff, L. C. (2010). Annual report to the nation on the status of cancer, 1975-2006, featuring colorectal cancer trends and impact of interventions (risk factors, screening, and treatment) to reduce future rates. *Cancer*, *116*(3), 544–573.

Engelmann, R. H., & Middendorf, W. H. (1995). *Handbook of electric motors* (Vol. 92). Marcel Dekker.

Engineers, A. S. of M. (1997). *Standard ASME B1. 5-1997 (2004): Acme Screw Threads*. American Society of Mechanical Engineers.

Fesharakizadeh, M., Taheri, D., Dolatkhah, S., & Wexner, S. D. (2013). Postoperative ileus in colorectal surgery: is there any difference between laparoscopic and open surgery? *Gastroenterology Report*, *1*(2), 138–143.

Fisher, W. D., & Mujtaba, M. S. (1992). Sufficient stability condition for hybrid position/force control. In *Robotics and Automation, 1992. Proceedings., 1992 IEEE International Conference on* (pp. 1336–1341). IEEE.

Fleshman, J., Sargent, D. J., Green, E., Anvari, M., Stryker, S. J., Beart Jr, R. W., … Nelson, H. (2007). Laparoscopic colectomy for cancer is not inferior to open surgery based on 5-year data from the COST Study Group trial. *Annals of Surgery*, *246*(4), 655–664.

Fullerton, A., Andersen, J. R., Hoelgaard, A., & Menné, T. (1986). Permeation of nickel salts through human skin in vitro. *Contact Dermatitis*, *15*(3), 173–177.

Geetha, M., Singh, A. K., Asokamani, R., & Gogia, A. K. (2009). Ti based biomaterials, the ultimate choice for orthopaedic implants–a review. *Progress in Materials Science*, *54*(3), 397–425.

Golub, R., Siddiqui, F., & Pohl, D. (1998). Laparoscopic versus open appendectomy: a metaanalysis. *Journal of the American College of Surgeons*, *186*(5), 545–553.

Group, C. O. of S. T. S. (2004). A comparison of laparoscopically assisted and open colectomy for colon cancer. *The New England Journal of Medicine*, *350*(20), 2050.

Group, C. C. L. or O. R. S. (2005). Laparoscopic surgery versus open surgery for colon cancer: short-term outcomes of a randomised trial. *The Lancet Oncology*, *6*(7), 477–484.

Group, T. L. A. vs O. C. T. S. (2007). Laparoscopically assisted vs open colectomy for colon cancer: a meta-analysis. *Archives of Surgery*, *142*(3), 298.

Guerrieri, M., Campagnacci, R., De Sanctis, A., Lezoche, G., Massucco, P., Summa, M., … Lezoche, E. (2012). Laparoscopic versus open colectomy for TNM stage III colon cancer: results of a prospective multicenter study in Italy. *Surgery Today*, *42*(11), 1071–1077.

Ha, Q., Santos, M., Nguyen, Q., Rye, D., & Durrant-Whyte, H. (2002). Robotic excavation in construction automation. *Robotics & Automation Magazine, IEEE*, *9*(1), 20–28.

Hamdi-Cherif, A. (2011). *Knowledge-Based Control for Robot Arm*. INTECH Open Access Publisher.

Hassan, S., Anwer, N., Khattak, Z., & Yoon, J. (2010). Open architecture dynamic manipulator design philosophy (DMD). *Robotics and Computer-Integrated Manufacturing*, *26*(2), 156–161.

Hiltebrandt, S., & Wolf, J. (1992, May 19). Organ manipulator. *Google Patents*. Retrieved from http://www.google.co.uk/patents/US5113846

Hiroi, M., Hojo, M., Hashimoto, Y., Abe, Y., & Dote, Y. (1986). Microprocessor-Based Decoupled Control of Manipulator Using Modified Model-Following Method with Sliding Mode. *IEEE Transactions on Industrial Electronics, 2*(IE-33), 110–113.

Hogan, N. (1984). Impedance control: An approach to manipulation. In *American Control Conference, 1984* (pp. 304–313). IEEE.

Huang, J. B., Xie, Z. W., Liu, H., Sun, K., Liu, Y. C., & Jiang, Z. N. (2008). DSP/FPGA-based controller architecture for flexible joint robot with enhanced impedance performance. *Journal of Intelligent and Robotic Systems*, *53*(3), 247–261.

Hurd, S. A., Carnegie, D. A., Brown, N. R., & Gaynor, P. T. (2005). Development of an intelligent robotic system for the automation of a meat-processing task. *International Journal of Intelligent Systems Technologies and Applications*, *1*(1-2), 32–48.

Jamner, J. (1993, August 17). Endoscopic retractor. *Google Patents*. Retrieved from https://www.google.com.au/patents/US5235966

Jemal, A., Bray, F., Center, M. M., Ferlay, J., Ward, E., & Forman, D. (2011). Global cancer statistics. *CA: A Cancer Journal for Clinicians*, *61*(2), 69–90.

Josefsen, T. (1993, March 23). Surgical retractor. *Google Patents*. Retrieved from https://www.google.ch/patents/US5195505

Jung, S., Hsia, T. C., & Bonitz, R. G. (2001). Force tracking impedance control for robot manipulators with an unknown environment: theory, simulation, and experiment. *The International Journal of Robotics Research*, *20*(9), 765–774.

Jung, S., Hsia, T. C., & Bonitz, R. G. (2004). Force tracking impedance control of robot manipulators under unknown environment. *Control Systems Technology, IEEE Transactions on*, *12*(3), 474–483.

Katić, D., & Vukobratović, M. (2002). *Advanced Control of Robot Compliance Tasks Using Hybrid Intelligent Paradigms*. Springer.

Kaya, C. Y., Lucas, S. K., & Simakov, S. T. (2004). Computations for bang–bang constrained optimal control using a mathematical programming formulation. *Optimal Control Applications and Methods*, *25*(6), 295–308.

Kelly, R., & Salgado, R. (1994). PD control with computed feedforward of robot manipulators: A design procedure. *IEEE Transactions on Robotics and Automation*, *10*(4), 566–571.

Khatib and Burdick, O., & Burdick, J. (1986). Motion and force control of robot manipulators. In *Robotics and Automation. Proceedings. 1986 IEEE International Conference on* (Vol. 3, pp. 1381–1386). IEEE.

Khatib, O. (1987). A unified approach for motion and force control of robot manipulators: The operational space formulation. *Robotics and Automation, IEEE Journal of*, *3*(1), 43–53.

Kierzenka, J., & Shampine, L. F. (2001). A BVP solver based on residual control and the Maltab PSE. *ACM Transactions on Mathematical Software (TOMS)*, *27*(3), 299–316.

Kiran, R. P., Delaney, C. P., Senagore, A. J., Millward, B. L., & Fazio, V. W. (2004). Operative blood loss and use of blood products after laparoscopic and conventional open colorectal operations. *Archives of Surgery*, *139*(1), 39–42.

Klein, C. A., & Maney, J. J. (1979). Real-time control of a multiple-element mechanical linkage with a microcomputer. *Industrial Electronics and Control Instrumentation, IEEE Transactions on*, (4), 227–234.

Komati, B., Clévy, C., & Lutz, P. (2014). Force tracking impedance control with unknown environment at the microscale. In *Robotics and Automation (ICRA), 2014 IEEE International Conference on* (pp. 5203–5208). IEEE.

Koninckx, P. R. (1997, September 2). Instrument set for laparoscopic hysterectomy. *Google Patents.* Retrieved from https://www.google.co.uk/patents/US5662676

Kröger, T., Finkemeyer, B., Heuck, M., & Wahl, F. M. (2004). Adaptive implicit hybrid force/pose control of industrial manipulators: Compliant motion experiments. In *Intelligent Robots and Systems, 2004.(IROS 2004). Proceedings. 2004 IEEE/RSJ International Conference on* (Vol. 1, pp. 816–821). IEEE.

Kuzmak, L. I. (1996, June 4). Finger-like laparoscopic blunt dissector device. Google Patents. Retrieved from http://www.google.co.uk/patents/US5522788

Lacy, A. M., Delgado, S., Castells, A., Prins, H. A., Arroyo, V., Ibarzabal, A., & Pique, J. M. (2008). The long-term results of a randomized clinical trial of laparoscopy-assisted versus open surgery for colon cancer. *Annals of Surgery*, *248*(1), 1–7.

Larapedia. (2016) Screws and nomenclature of thread technical drawing. [Online] Availablefrom:http://www.larapedia.com/engineering_quality_summaries/screws_a nd_nomenclature_of_thread_technical_drawing.html [Accessed 24th June 2016].

Ledzewicz, U., & Schättler, H. (2002). Analysis of a cell-cycle specific model for cancer chemotherapy. *Journal of Biological Systems*, *10*(03), 183–206.

Ledzewicz, U., & Schättler, H. (2002). Optimal bang-bang controls for a two-compartment model in cancer chemotherapy. *Journal of Optimization Theory and Applications*, *114*(3), 609–637.

Lee, K., & Buss, M. (2008). Force tracking impedance control with variable target stiffness. In *Proceedings of the 17th IFAC World Congress* (Vol. 17, pp. 6751–6756).

Lefebvre, T., Xiao, J., Bruyninckx, H., & De Gersem, G. (2005). Active compliant motion: a survey. *Advanced Robotics*, *19*(5), 479–499.

Li, S., Chi, P., Lin, H., Lu, X., & Huang, Y. (2011). Long-term outcomes of laparoscopic surgery versus open resection for middle and lower rectal cancer: an NTCLES study. *Surgical Endoscopy*, *25*(10), 3175–3182.

Mason, M. T. (1981). Compliance and force control for computer controlled manipulators. *Systems, Man and Cybernetics, IEEE Transactions on*, *11*(6), 418–432.

Matinfar, M., & Hashtrudi-Zaad, K. (2005). Optimization-based robot compliance control: Geometric and linear quadratic approaches. *The International Journal of Robotics Research*, *24*(8), 645–656.

Matula, P. A., & Remiszewski, S. H. (1995, January 17). *Surgical retractor*. Google Patents. Retrieved from http://www.google.co.uk/patents/US5381788

Merika, E., Saif, M. W., Katz, A., Syrigos, C., & Morse, M. (2010). Colon cancer vaccines: an update. *In Vivo*, *24*(5),607–628.

Milsom, J. W., Böhm, B., & Nakajima, K. (2006). *Laparoscopic colorectal surgery*. Springer.

Morgan, R. G., & Özgüner, Ü. (1985). A decentralized variable structure control algorithm for robotic manipulators. *Robotics and Automation, IEEE Journal of*, *1*(1), 57–65.

Nagata, F., Watanabe, K., & Izumi, K. (2001). Furniture polishing robot using a trajectory generator based on cutter location data. In *Robotics and Automation, 2001. Proceedings 2001 ICRA. IEEE International Conference on* (Vol. 1, pp. 319–324). IEEE.

National Cancer Institute. (2016) Colon Cancer Treatment (PDQ®)–Patient Version. [Oneline] Available from: https://www.cancer.gov/types/colorectal/patient/colon-treatment-pdq#section/all [Accessed 24th June 2016].

Nef, T., Mihelj, M., & Riener, R. (2007). ARMin: a robot for patient-cooperative arm therapy. *Medical & Biological Engineering & Computing*, *45*(9), 887–900.

Oberg, E. (2012). *Section 11. Machine Elements–Machinery's Handbook 29*. Industrial Press.

Engineers, A. S. of M. (1997). *Standard ASME B1. 5-1997 (2004): Acme Screw Threads*. American Society of Mechanical Engineers.

Olsder, G. J. (2002). On open-and closed-loop bang-bang control in nonzero-sum differential games. *SIAM Journal on Control and Optimization*, *40*(4), 1087–1106.

Onori, S., Serrao, L., & Rizzoni, G. (2016). Pontryagin's Minimum Principle. In *Hybrid Electric Vehicles* (pp. 51–63). Springer.

Owen, W., Croft, E., & Benhabib, B. (2008). Stiffness optimization for two-armed robotic sculpting. *Industrial Robot: An International Journal*, *35*(1), 46–57.

Pedro, J. O., Mthethwa, M., & Nyandoro, O. T. (n.d.). Time-Optimal Control of Robotic Manipulators Modelled with Actuators Dynamics. In *1st African Control Conference (AFCON 2003), South Africa*.

Raibert, M. H., & Craig, J. J. (1981). Hybrid position/force control of manipulators. *Journal of Dynamic Systems, Measurement, and Control*, *103*(2), 126–133.

Richardson, R., Brown, M., Bhakta, B., & Levesley, M. (2005). Impedance control for a pneumatic robot-based around pole-placement, joint space controllers. *Control Engineering Practice*, *13*(3), 291–303.

Seraji, H., & Colbaugh, R. (1997). Force tracking in impedance control. *The International Journal of Robotics Research*, *16*(1), 97–117.

School of Medicine. (2012) Introduction to Clinical Oncology, Cancer Staging. [Online] Available from: http://www.collaborativecurriculum.ca/en/modules/oncologyintro/oncology-fundamentals-cancertreatment-02.jsp [Accessed 24th June 2016].

Schreuder, H. W. R., & Verheijen, R. H. M. (2009). Robotic surgery. *BJOG: An International Journal of Obstetrics & Gynaecology*, *116*(2), 198–213.

Simakov, S. T., Kaya, C. Y., & Lucas, S. K. (2002). Computations for time-optimal bang–bang control using a Lagrangian formulation. In *Preprints of IFAC 15th Triennial World Congress*.

Slotine, J., & Sastry, S. S. (1983). Tracking control of non-linear systems using sliding surfaces, with application to robot manipulators†. *International Journal of Control*, *38*(2), 465–492.

Springplungers. (2015) Balls plungers.[Online] Available from: http://www.springplungers.com/ [Accessed 24th June 2016].

Sticca, R. P., Alberts, S. R., Mahoney, M. R., Sargent, D. J., Finstuen, L. M., Nelson, G. D., … Pockaj, B. A. (2013). Current use and surgical efficacy of laparoscopic colectomy in colon cancer. *Journal of the American College of Surgeons*, *217*(1), 56–62.

Texas instrument Ltd., (2015) DRV8801.[Online] Available from: http://www.ti.com/product/DRV8801[Accessed 24th June 2016

Tjandra, J. J., & Chan, M. K. Y. (2006). Systematic review on the short-term outcome of laparoscopic resection for colon and rectosigmoid cancer. *Colorectal Disease*, *8*(5), 375–388.

The AnastomoSEAL Project. (2013) Colorectal cancer resection. [Online] Available from: https://www.anastomoseal.eu/goals-of-the-anastomoseal-project/ [Accessed 24th June 2016].

Tsuji, T., & Tanaka, Y. (2008). Bio-mimetic impedance control of robotic manipulator for dynamic contact tasks. *Robotics and Autonomous Systems*, *56*(4), 306–316.

University of Maryland medical center. (2012) Large bowel resection-series. [Online] Available from: http://umm.edu/health/medical/reports/presentations/large-bowel-resection-series [Accessed 24th June 2016].

Vakhrameev, S. A. (1997). A bang-bang theorem with a finite number of switchings for nonlinear smooth control systems. *Journal of Mathematical Sciences*, *85*(3), 2002–2016.

Vukobratovic, M. (2009). Dynamics and robust control of robot-environment interaction (Vol. 2). *World Scientific.*Figure 1.1 and Figure 1.3.[Accessed 24th June 2016]

Von Stryk, O., & Schlemmer, M. (1994). *Optimal control of the industrial robot Manutec r3*. Springer.

Wang, L., Hao, Y., Wang, F., & Liu, H. (2007). Experimental study of force control based on intelligent prediction algorithm in open architecture robot system. In

Robotics and Biomimetics, 2007. ROBIO 2007. IEEE International Conference on (pp. 1675–1681). IEEE.

Wang, Z., Peer, A., & Buss, M. (2009). Fast online impedance estimation for robot control. In *Mechatronics, 2009. ICM 2009. IEEE International Conference on* (pp. 1–6). IEEE.

WebMD. (2009) Digestive Disorders Health Center.[Online] Available from: http://www.webmd.com/digestive-disorders/picture-of-the-colon [Accessed 24th June 2016].

World health organization. (2013) Crude rates for different cancers regarding to incidence and mortality.[Online] Available from: http://www.who.int/en/ [Accessed 24th June 2016].

Young, K.-K. D. (1978). Controller design for a manipulator using theory of variable structure systems. *Systems, Man and Cybernetics, IEEE Transactions on*, *8*(2), 101–109.